

INFORMATION AND COMMUNICATION THEORETICAL
MODELING, DESIGN, AND ANALYSIS OF HETEROGENEOUS
NANOSCALE COMMUNICATION CHANNELS

by

Deniz Kılınç

A Thesis Submitted to the
Graduate School of Engineering
in Partial Fulfillment of the Requirements for
the Degree of
Master of Science
in
Electrical and Electronics Engineering

Koç University

July 11, 2013

Koç University
Graduate School of Sciences and Engineering

This is to certify that I have examined this copy of a master's thesis by

Deniz Kılınç

and have found that it is complete and satisfactory in all respects,
and that any and all revisions required by the final
examining committee have been made.

Committee Members:

Özgür B. Akan, Ph. D. (Advisor)

Alper T. Erdoğan, Ph. D.

B. Erdem Alaca, Ph. D.

Date: _____

*Anneme ve Babama,
Zeynep ve Aziz Kılınç.*

ABSTRACT

Nanoscale communication between nanodevices is a novel and interdisciplinary concept including nanotechnology, biotechnology and communication technology. The construction of nanonetworks by interconnecting nanodevices expands the capabilities of single nanodevices by means of cooperation between them. In this thesis, we first investigate the nanoscale molecular communication channel between cardiomyocytes, i.e., Gap Junction (GJ) communication channel, from an information theoretical perspective. In addition, we use the GJ communication model to establish relations between cardiac diseases and GJ communication parameters for diagnosis and treatment of cardiac diseases, which is promising for future nanomedicine and bio-inspired nanoscale communication applications. Next, we present several receiver designs for diffusion-based molecular communication which is very prone to intersymbol interference (ISI) due to residual molecules emitted previously. Furthermore, the stochastic nature of the molecule movements adds a signal dependent noise to the diffusion-based molecular communication. We introduce optimal sequence detection and channel equalization methods to mitigate ISI and signal dependent noise, which arise in the diffusion-based molecular communication. Afterwards, we introduce a novel nanoscale wireless communication technique: Wireless Nanoscale Magneto-Inductive (WNMI) communication in which the magnetic coupling between nanocoils is used to form a wireless communication channel. Then, we investigate the WNMI communication channel to reveal its communication capabilities using information theory. The numerical results reveal that the WNMI communication stands as a promising solution to nanoscale communication between nanodevices. Finally, we present another novel and radically different nanoscale communication method: Nanoscale Heat Communication (NHC) in which the heat transfer via diffusion of the thermal energy is used for communication at the nanoscale. In addition, we present an information theoretical analysis of the NHC channel to find its capacity.

ÖZETÇE

Nano-aygıtlar arasındaki nano-ölçekli iletişim oldukça yenilikçi ve nanoteknoloji, biyoteknoloji ve iletişim teknolojilerini gerektiren disiplinler arası bir araştırma alanıdır. Nano-aygıtların birbirlerine haberleşme kanallarıyla bağlanmasıyla oluşturulan nano-ağlar, nano-aygıtların birlikte çalışmasını sağlayarak yeteneklerini artırır. Bu tezde ilk olarak kalp kası hücreleri arasındaki moleküler haberleşme kanalı, diğer adıyla oluklu bağlantı (GJ) haberleşme kanalı, bilgi kuramsal olarak incelenip modellenmiştir. Bu model, kalp hastalıkları ve GJ haberleşme kanalı parametreleri arasında bir ilişki kurabilmek için kullanılmıştır. Bu sayede kalp hastalıklarının teşhis ve tedavisi için bilgi ve haberleşme teknolojilerinden faydalanmanın yolu açılmıştır. Sonrasında difüzyona dayalı moleküler haberleşmede görülen işarete bağlı gürültü ve semboller arası girişim ile baş edebilmek için çeşitli alıcı tasarımları yapılmıştır. Bu tasarımlar arasında optimum dizi tespiti ve kanal eşitleme yöntemleri bulunmaktadır. Daha sonra, yeni bir nano-ölçekli haberleşme yöntemi olan ve nano-bobinler arasındaki manyetik bağlantıya dayanan kablosuz nano-ölçekli magneto-endüktif (WNMI) haberleşme modeli sunulmuştur. WNMI haberleşme kanalının kapasitesi bilgi kuramsal olarak analiz edilip bulunmuştur. Sayısal analizler WNMI haberleşme yönteminin nano-ölçekli kablosuz haberleşme için umut verici bir teknik olduğunu göstermektedir. Son olarak bir başka yeni bir nano-ölçekli haberleşme yöntemi olan nano-ölçekli ısı ile haberleşme (NHC) modeli tanımlanmıştır. NHC haberleşme tekniğinde bilgi alış verişinin termal difüzyonla yayılması prensibine dayanmaktadır. Ayrıca NHC haberleşme kanalının kapasitesi bilgi kuramı kullanılarak bulunmuştur.

ACKNOWLEDGMENTS

I would like to gratefully acknowledge the enthusiastic supervision of Dr. Özgür B. Akan in all steps of the development of this work. He taught me not just how to conduct research, but how to achieve success in life. I achieved more than I ever dreamed of in two years by his guidance and help, and I am proud of being one of his students.

I would like to thank to Dr. Alper T. Erdoğan and Dr. B. Erdem Alaca for taking part in my thesis committee and for their invaluable suggestions and comments.

I want to thank the Next-generation and Wireless Communications Laboratory members due to their friendship and collaboration during last two years. I would also like to thank my best friends Bahadır, Can, Tufan, Haydar, and Serhat for their stimulating ideas and inspirational discussions. I thank Gülce for being my friend and my love with her constant support and encouragement.

I want to acknowledge the support of TÜBİTAK and Koç University, which made the completion of this thesis possible.

I thank my parents, Zeynep and Aziz, and my brother Alişan for believing in me and trusting me at every step I have taken so far. I am very lucky to be a part of such a wonderful family.

TABLE OF CONTENTS

Abstract	iv
Özetçe	v
Acknowledgments	vi
List of Tables	xi
List of Figures	xii
Abbreviations	xvi
Chapter 1: Introduction	1
1.1 Nanoscale Molecular Communication	2
1.2 Nanoscale Magneto-Inductive Communication	3
1.3 Nanoscale Heat Communication	4
1.4 Research Objectives and Solutions	5
1.4.1 Nanoscale Molecular Gap Junction Communication Channel	5
1.4.2 Receiver Design for Molecular Communication	6
1.4.3 Nanoscale Magneto-Inductive Communication Channel	6
1.4.4 Nanoscale Heat Communication Channel	7
1.5 Thesis Outline	8
Chapter 2: Nanoscale Molecular Gap Junction Communication Channel	9
2.1 Introduction	9
2.2 Physical Model of GJ Communication	12

2.2.1	Action Potential Propagation	13
2.2.2	Physical Model of Gap Junction Channels	16
2.2.3	Action Potential Propagation Failure	18
2.2.4	Spontaneous Action Potential Initiation	21
2.3	Information Theoretical Analysis of Gap Junction Communication Channel .	23
2.4	Numerical Analysis	25
2.4.1	Channel Capacity	28
2.4.1.1	Effect of Number of Gap Junction Channels	28
2.4.1.2	Effect of Cardiomyocyte Length	28
2.4.1.3	Effect of Cardiomyocyte Radius	30
2.4.1.4	Effect of Membrane Resistivity of Cardiomyocyte	30
2.4.1.5	Effect of Free Calcium Concentration	31
2.4.2	Channel Propagation Delay	31
2.4.3	Information Transmission Rate	32
2.5	Gap Junction Communication Channel Parameters and Cardiac Diseases . .	34
2.5.1	Channel Capacity and Cardiac Diseases	34
2.5.1.1	Number of Gap Junction Channels	34
2.5.1.2	Length of Cardiomyocyte	35
2.5.1.3	Radius of Cardiomyocyte	35
2.5.1.4	Membrane Resistivity	35
2.5.1.5	Free Calcium Concentration	36
2.5.2	Channel Propagation Delay and Cardiac Diseases	36
2.5.3	Information Transmission Rate and Cardiac Diseases	36
2.5.4	Application on Nanomedicine	37
Chapter 3: Receiver Design for Molecular Communication		39
3.1	Introduction	39
3.2	Molecular Communication Model	42

3.3	Sequence Detection	47
3.3.1	MAP Sequence Detection	48
3.3.2	ML Sequence Detection	50
3.4	Minimum Mean-Square Error Equalizer	51
3.5	Minimum Mean-Square Error Decision-Feedback Equalizer	54
3.6	Adaptive Receiver	58
3.7	Performance Analysis	59
3.7.1	Time Invariant Channel	61
3.7.2	Time Varying Channel	62
Chapter 4:	Nanoscale Magneto-Inductive Communication Channel	64
4.1	Introduction	64
4.2	Physical Model of Point-to-Point WNMI Communication	67
4.3	Waveguide Model for WNMI Communication	72
4.4	Information Theoretical Analysis of WNMI Communication	75
4.5	Performance Evaluation	77
4.5.1	Path Loss in Point-to-Point WNMI Communication	78
4.5.2	Path Loss in WNMI Communication Waveguide	79
4.5.3	Channel Capacity of Point-to-Point WNMI Communication	81
4.5.4	Channel Capacity of WNMI Communication Waveguide	83
Chapter 5:	Nanoscale Heat Communication Channel	86
5.1	Introduction	86
5.2	Theory of Magnetocaloric Effect	89
5.3	Physical Model of Nanoscale Heat Communication	92
5.3.1	Transmitter	92
5.3.2	Signal Propagation	97
5.3.3	Noise	98
5.3.4	Receiver	99

5.4	An Information Theoretical Analysis of Nanoscale Heat Communication . . .	100
5.5	Performance Evaluation	103
5.5.1	Effect of Communication Distance	104
5.5.2	Effect of Adiabatic Temperature Change	105
5.5.3	Effect of Thermal Diffusivity Constant	107
Chapter 6:	Conclusions and Future Research Directions	109
6.1	Research Contributions	109
6.1.1	Nanoscale Molecular Gap Junction Communication Channel	109
6.1.2	Receiver Design for Molecular Communication	110
6.1.3	Nanoscale Magneto-Inductive Communication Channel	111
6.1.4	Nanoscale Heat Communication Channel	112
6.2	Future Research Directions	113
	References	115
	Curriculum Vitae	127

LIST OF TABLES

2.1	Simulation Parameters	27
5.1	Comparison Table of Molecular Communication and Nanoscale Heat Communication	89

LIST OF FIGURES

2.1	A simplified model of the GJ communication and the physical structure of GJs. (a) The GJ communication model. (b) The enlarged section of a GJ including several GJ channels. (c) The top view of a connexon.	11
2.2	The kinetic behavior of a GJ channel modeled by a state machine with three states, i.e., HH, HL, and LH. The rate constants β and α refer to the forward reactions high to low and the backward reactions low to high, respectively. . .	18
2.3	P_f plot with respect to the junctional voltage V_j and the total number of the GJ channels in a GJ, N . For the other parameters, the typical physiological values are used which are $L = 100\mu m$, $r = 11\mu m$, $R_i = 250\Omega cm$, $R_e = 100\Omega cm$, $R_m = 20k\Omega cm^2$, and $V_e = V_i/5$ adopted from [26, 40].	19
2.4	P_w plot with respect to ρ and P_{max} . The other parameters are $K = 15\mu M$, $M = 30000$, $n = 1.6$, and $T_s = 500msec$ [37].	22
2.5	The GJ communication channel transmission diagram with the transmission probabilities. The communication channel expresses binary asymmetric channel (BAC) characteristics.	24
2.6	An illustration for a successful and a failed AP transmissions between TC and RC. Time instants of two stimuli that are applied to TC and the membrane potential changes of TC and RC are shown. The simulation parameters are $N = 110$, $L = 100\mu m$, $r = 11\mu m$, $R_i = 250\Omega cm$, $R_e = 100\Omega cm$, $R_m = 20k\Omega cm^2$, $\rho = 100nM$, $P_{max} = 0.3$, $M = 30000$, $n = 1.6$, $T_s = T_{AP}$, $V_e = V_i/5$ [26, 37, 40].	26

2.7	$I(X;Y)$ in <i>bit</i> for several (a) number of the GJ channels, N , (b) length of the cardiomyocyte, L , (c) radius of the cardiomyocyte, r , (d) the membrane resistivity of the cardiomyocyte, R_m , and (e) the free Ca^{2+} concentration in the cytoplasm, ρ , with varying P_{AP}	29
2.8	The channel propagation delay, τ , between TC and RC with respect to the number of the GJ channels in the GJ, N	32
2.9	The information transmission rate, R , and the AP duration, T_{AP} , with respect to the maximum conductance of the calcium channels, G_{Ca}	33
3.1	The diffusion-based MC model between TN and RN. (a) Graphical representation. (b) Block diagram representation.	43
3.2	The noiseless molecule concentration variation at RN, $y(t)$, for $D = 2.2 \times 10^{-9} \text{m}^2/\text{s}$, $r = 250\text{nm}$, $m = 10^5$, $A = 4 \times 10^9$, $T_e = 4.7\mu\text{s}$	46
3.3	Discrete-time equivalent model of the molecular diffusion channel with intersymbol interference.	48
3.4	A trellis diagram for $I = 2$ with 2^I states.	50
3.5	The block diagram of MMSE equalizer with S tap coefficients.	52
3.6	The block diagram of the MMSE-DFE.	55
3.7	The conceptual model of the channel estimator using in a detector.	59
3.8	Bit error rates of four different detection approaches at different communication distances (a) $r = 50\text{nm}$, $R = 3.12\text{Mbps}$, (b) $r = 250\text{nm}$, $R = 127.9\text{kbps}$, and (c) $r = 1\mu\text{m}$, $R = 8.1\text{kbps}$ with same time invariant diffusion-based molecular channel known at RN.	62
3.9	Bit error rates of four different detection methods for time varying diffusion-based molecular communication channels with (a) $D(t) = 2.2 \times 10^{-9} + 0.8 \times 10^{-9} \cos(2\pi t) \text{m}^2/\text{s}$ and (b) $D(t) = 2.2 \times 10^{-9} + 0.8 \times 10^{-9} \cos(10\pi t) \text{m}^2/\text{s}$	62

4.1	(a) The schematic representation of a CNT bundle-based nanocoil with square planar geometry. (b) The enlarged view of a CNT bundle constituting the CNT bundle-based nanocoil. (c) The side view of a CNT bundle-based nanocoil.	68
4.2	The WNMI communication model and circuit models of the WNMI communication. (a) The model of the WNMI communication. (b) The transformer model of the WNMI communication. (c) The equivalent circuit of the transformer model.	70
4.3	The waveguide model for the WNMI communication and circuit models of the waveguide. (a) The model of the WNMI communication waveguide. (b) The transformer model. (c) The equivalent circuit of the transformer model. .	73
4.4	The path loss in the point-to-point WNMI communication P_L^{PTP} with respect to (a) the communication distance d for different relative permeability values μ_r and (b) the outer side length of the nanocoils a^o for different thicknesses of the CNT bundle t	79
4.5	The path loss in the WNMI communication waveguide P_L^{WG} with respect to (a) the communication distance d for different relative permeability values μ_r , (b) the outer side length of the nanocoils a^o for different thicknesses of the CNT bundle t , and (c) the inter-relay distance r	80
4.6	The channel capacity of the point-to-point WNMI communication C^{PTP} with respect to (a) the communication distance d for different relative permeability values μ_r and (b) the outer side length of the nanocoils a^o for different thicknesses of the CNT bundle t	82
4.7	The channel capacity of the WNMI communication waveguide C^{WG} with respect to (a) the communication distance d for different relative permeability values μ_r , (b) the outer side length of the nanocoils a^o for different thicknesses of the CNT bundle t , and (c) the inter-relay distance r	84

5.1	The schematic demonstration of the entropy of the ferromagnetic material with respect to the temperature for zero magnetic field H_0 and a nonzero magnetic field H_1	91
5.2	The NHC model and the temperature encoding mechanism with binary bipolar coding.	94
5.3	The block diagram representation of (a) transmitter and channel, and (b) receiver for the NHC model.	97
5.4	The binary asymmetric channel (BAC) representation for the NHC.	101
5.5	The numerical analysis results performed over the SNR in dB with respect to the (a) communication distance d , (b) adiabatic temperature change ΔT_{ad} , and (c) thermal diffusivity constant α	106
5.6	The numerical analysis results performed over the channel capacity C in bit/use with respect to (a) the communication distance d , (b) the adiabatic temperature change ΔT_{ad} , (c) the thermal diffusivity constant α	106
5.7	The numerical analysis results performed over the channel capacity C_{op} in bps with respect to (a) the communication distance d , (b) the adiabatic temperature change ΔT_{ad} , (c) the thermal diffusivity constant α	106

ABBREVIATIONS

AP	Action Potential
AWGN	Additive White Gaussian Noise
BAC	Binary Asymmetric Channel
CNT	Carbon Nanotube
CRU	Calcium Release Unit
DAD	Delayed Afterdepolarization
EAD	Early Afterdepolarization
EM	Electro-Magnetic
FSM	Finite State Machine
GJ	Gap Junction
ICM	Ischemic Cardiomyopathy
ISI	Intersymbol Interference
LC	Loading Cardiomyocyte
LPF	Low Pass Filter
MAP	Maximum a Posteriori
MC	Molecular Communication
MCE	Magnetocaloric Effect
MI	Magneto-Inductive
ML	Maximum Likelihood
MMSE	Minimum Mean Square Error
MMSE-DFE	MMSE Decision Feedback Equalizer
NHC	Nanoscale Heat Communication
OOK	On-Off Keying
RC	Receiver Cardiomyocyte

RN	Receiver Nanodevice
SNR	Signal-to-Noise Ratio
SWCNT	Singe-Walled Carbon Nanotube
TC	Transmitter Cardiomyocyte
TN	Transmitter Nanodevice
WNMI	Wireless Nanoscale Magneto-Inductive

Chapter 1

INTRODUCTION

Recent advances in the nanotechnology field have enabled the realization of intelligent nanoscale devices, i.e., nanodevices (e.g., artificial devices or engineered organisms), inspired from the characteristics of molecular structures and biological cells. Nanodevices are fullfeatured devices which are able to independently perform complex tasks ranging from computing and data storing to sensing and actuation. However, their limited memory and processing capabilities point out the requirement for establishment of nanonetworks, i.e., a number of nanomachines connected using nanoscale communication to jointly execute application-specific tasks. The nanoscale communication between nanodevices is a novel and interdisciplinary concept including nanotechnology, biotechnology and communication technology [1]. The construction of nanonetworks by interconnecting nanodevices expands the capabilities of single nanodevices by means of cooperation between them [2, 3]. In the literature, there are several proposed techniques for the realization of the nanoscale communication namely electromagnetic, acoustic or molecular communication [4, 5].

In this thesis, we first investigate the nanoscale molecular communication channel between cardiomyocytes, i.e., Gap Junction (GJ) communication channel, from an information theoretical perspective. Next, we present several receiver designs for diffusion-based molecular communication to mitigate intersymbol interference and signal dependent noise. Afterwards, we introduce a novel nanoscale wireless communication technique: Wireless Nanoscale Magneto-Inductive (WNMI) communication in which the magnetic coupling between nanocoils is used to form a wireless communication channel. Then we investigate the WNMI communication channel to reveal its communication capabilities using information theory. Finally, we present another novel and radically different nanoscale communication

method: Nanoscale Heat Communication (NHC) in which the heat transfer via diffusion of the thermal energy is used for communication at the nanoscale. In addition, we present an information theoretical analysis for the NHC channel to find its capacity.

1.1 Nanoscale Molecular Communication

Molecular communication (MC) is a promising paradigm for communication at nanoscale [1, 4] and it is inspired by the communication of the biological systems at cellular level [6]. In the MC, molecules are utilized to encode, transmit, and receive information. It is believed that the integration process of the molecular transceivers in nanodevices is more feasible due to their size and natural domain unlike the classical communication techniques [8]. Several nature-inspired and theoretically modeled MC techniques exist in the literature. For example, in [6], based on the diffusion of pheromones, spores, and pollen, a long range interconnection of nanodevices deployed over distances from a few centimeters to several meters is discussed. On the other hand, short range MC technique between cardiomyocytes is constructed by Gap Junction (GJ) channels and it is called GJ communication[17]. The GJ communication is a promising solution to the communication of nanodevices. For example, both MC system inspired by cell to cell communications through GJs [19] and MC based on intercellular calcium signaling [20] require utilization of the GJ communication channels for the communication in the nanoscale. However, these studies do not propose a solution for the problem of modeling and analyzing the GJ communication channel from the information theoretical perspective.

The research on the information theoretical investigation of the MC has been heavily conducted in the literature [11], [52], [16], [53]. However, to the date, there is little effort addressing the design of a receiver nanodevice which detects the transmitted information from the received molecular concentration signal. For the MC, the information is encoded in the concentration of the emitted molecules with on-off keying (OOK) modulation in [7], [15], [14]. An emitted concentration pulse changes the molecule concentration at the receiver location. Because of the diffusion of the emitted molecules from regions of high concentration to those of low concentration, the molecule concentration at the receiver

location decreases if the molecule emission ceases. However, the emitted molecules do not vanish completely in the reception space. Therefore, a low signaling interval, i.e., a high transmission rate, causes intersymbol interference (ISI) in the MC. If the transmitter waits long enough to send a new concentration pulse, the effect of the ISI can be eliminated; then, the information transmission rate becomes very low. Nevertheless, having high transmission rates is desirable to improve communication capabilities of nanodevices.

1.2 Nanoscale Magneto-Inductive Communication

Several techniques in the literature are presented for the realization of the nanoscale communication namely electromagnetic, acoustic, or molecular communication [4], [5]. However, for the first time in the literature, we introduce a novel nanoscale wireless communication technique: Wireless Nanoscale Magneto-Inductive (WNMI) communication in which the magnetic coupling between nanocoils is used to form a wireless communication channel. Using Electro-Magnetic (EM) waves for wireless communication at nanoscale has several disadvantages which are high absorption losses due to molecular absorption and frequency selective characteristics of the channel [61]. The molecular absorption loss is caused by the process by which part of the transmitted EM wave is converted into internal kinetic energy of some of the molecules in the communication medium [62]. In addition, since different molecule types have different resonant frequencies and the absorption at each resonance spreads over a range of frequencies, the nanoscale wireless EM communication channel is very frequency-selective [61].

The WNMI communication stands as a promising alternative method for nanoscale wireless communication because it solves the problems associated with the nanoscale wireless EM communication. First, since EM waves are not used, the WNMI communication mitigates the high absorption losses caused by molecular absorption. Second, in the WNMI communication, the channel conditions depend on the magnetic permeability of the medium [66]; thus, having a communication medium with uniform permeability enables constant channel conditions for the WNMI communication. A uniform channel can be created in a variety of media such as air, water, blood, and tissue liquid due to almost the same permeability. In

spite of its advantages, the point-to-point WNMI communication is a short-range nanoscale communication since the strength of the magnetic field falls off much faster than that of EM waves [63, 65]. That is, whereas the molecular absorption in the WNMI communication is much less than that in the EM waves, the path loss of the WNMI communication may be higher than the EM communication. Nevertheless, the path loss in the WNMI communication can be greatly reduced and the communication range can be significantly increased by forming a waveguide structure with passive relay nanonodes similar to waveguides employed in Magneto-Inductive (MI) communication [64, 66].

1.3 Nanoscale Heat Communication

Although recently, Molecular Communication (MC) is considered as a promising solution for the communication of nanodevices [7, 17], there are several disadvantages of MC. For example, the limitation in the molecule storage of a nanodevice restricts the lifetime of a nanonetwork and makes the MC impractical. On the other hand, refilling the molecule storage of a nanodevice is very challenging. Furthermore, in the MC, the emission of the signal molecules in the communication medium may result in undesired accumulation of these molecules. For the first time in the literature, we introduce a novel and radically different nanoscale communication concept: Nanoscale Heat Communication (NHC) in which the heat transfer is used for communication at the nanoscale. The NHC is based on the diffusion of the thermal energy. That is, the temperature of the transmitter nanodevice is modulated according to the transmitted information. The thermal energy emitted due to an increase in the temperature of the transmitter or absorbed due to a decrease in the temperature of the transmitter changes the temperature at the receiver location due to the laws of thermal diffusion. Then, the temperature variation at the receiver location is sensed by the receiver nanodevice using a thermal nanosensor.

The temperature modulation of the transmitter nanodevice is achieved by using the MagnetoCaloric Effect (MCE) which is a well-known phenomenon defined as the change in temperature of magnetic materials exposed to a varying magnetic field [82]. We use the MCE in the NHC because it can be successfully implemented for temperature modu-

lation at nanoscale. By utilizing a nanosolenoid to create a magnetic field and a magnetic nanoparticle, the transmitter nanodevice can modulate the temperature of the nanoparticle to transmit the desired information. Recently, the production and utilization of carbon nanosolenoids have been successfully realized using carbon nanotubes (CNTs) [83, 84, 85]. In addition, the theoretical analyses of the CNT bundle-based inductors are presented in [86, 87]. CNTs bundle-based inductors have been proposed as a possible replacement for copper inductors due to their high conductivity and current carrying capabilities [88, 89].

1.4 Research Objectives and Solutions

The objectives of our research and the solution approaches are explained in this section.

1.4.1 Nanoscale Molecular Gap Junction Communication Channel

Molecular communication (MC) is a promising paradigm to communicate at nanoscale and it is inspired by nature. One of the MC methods in nature is the Gap Junction (GJ) communication between cardiomyocytes. The GJ communication is achieved by diffusion of ions through GJ channels between the cells. The transmission of the information is realized by means of the propagation of the Action Potential (AP) signal. Both the probability of the AP propagation failure and the probability of the spontaneous AP initiation are obtained. For the first time in the literature, the GJ communication channel is modeled and analyzed from the information theoretical perspective to find the communication channel capacity. A closed-form expression is derived for the capacity of the GJ communication channel. The channel capacity, propagation delay and information transmission rate are analyzed numerically for a three-cell network. The results of the numerical analyses point out a correlation between an increase in the incidence of several cardiac diseases and a decrease in the channel capacity, an increase in the propagation delay, and either an increase or a decrease in the transmission rate. The method that we use and results that are presented may help in the investigation, diagnosis and treatment of cardiac diseases as well as help in the design of nanodevices communicating via GJ channels.

1.4.2 Receiver Design for Molecular Communication

In the Molecular Communication (MC), molecules are utilized to encode, transmit, and receive information. Transmission of the information is achieved by means of diffusion of molecules and the information is recovered based on the molecule concentration variations at the receiver location. The MC is very prone to intersymbol interference (ISI) due to residual molecules emitted previously. Furthermore, the stochastic nature of the molecule movements adds noise to the MC. For the first time, we propose four methods for a receiver in the MC to recover the transmitted information distorted by both ISI and noise. We introduce sequence detection methods based on maximum a posteriori (MAP) and maximum likelihood (ML) criterions, both a linear equalizer and a nonlinear decision-feedback equalizer based on minimum mean-square error (MMSE) criterion. We present a channel estimator to estimate time varying MC channel at the receiver. The performances of the proposed methods based on bit error rates are evaluated. The sequence detection methods reveal the best performance at the expense of computational complexity. However, the MMSE equalizer has the lowest performance with the lowest computational complexity. The results show that using these methods significantly increases the information transmission rate in the MC.

1.4.3 Nanoscale Magneto-Inductive Communication Channel

Nanonetworks constructed by interconnecting nanodevices using wireless communication allow nanodevices to perform more complex functions by means of cooperation between them. For the first time in the literature, we introduce a novel nanoscale wireless communication technique: Wireless Nanoscale Magneto-Inductive (WNMI) communication in which the magnetic coupling between nanocoils is used to establish a communication channel. The nanocoils considered in this thesis are formed by Carbon NanoTube (CNT) bundles. The WNMI communication solves high molecular absorption and frequency selective channel characteristics problems, which are encountered in nanoscale wireless electromagnetic communication, by introducing low absorption losses and flat channel characteristics. We begin

with a presentation of the physical model of the point-to-point WNMI communication. Then, we introduce the waveguide technique for the WNMI communication. We derive path loss expressions for both of these methods. Afterwards, we present an information theoretical analysis for both the point-to-point and waveguide-based WNMI communication techniques to find their channel capacities. The performance analyses show that using waveguide technique in the WNMI communication significantly increases both the channel capacity and feasible communication range by greatly reducing the path loss. Based on the performance evaluations, the WNMI communication stands as a promising solution to nanoscale communication between nanodevices.

1.4.4 Nanoscale Heat Communication Channel

Nanodevices can perform more complex functions in nanonetworks constructed by interconnecting nanodevices using wireless communication by allowing cooperation between nanodevices. For the first time in the literature, we introduce a novel and physically realizable nanoscale communication technique: Nanoscale Heat Communication (NHC) in which the heat transfer is used for communication at the nanoscale. The transmitted information is encoded in temperature signals using the MagnetoCaloric Effect (MCE) which is the change in temperature of a magnetic material exposed to a varying magnetic field. Thermal energy emitted or absorbed by a transmitter nanodevice is subject to the laws of thermal diffusion which changes the temperature of the communication medium. The transmitted information is decoded by a receiver nanodevice that senses the temperature variations. We derive an analytical expression for signal-to-noise ratio (SNR) in the NHC. Using the information theoretical analysis, we obtain the closed-form expression for the channel capacity. According to the performance evaluation of the channel capacity, the NHC provides a significantly higher capacity communication compared with the existing nanoscale communication techniques. Therefore, the NHC stands as a promising solution to nanoscale communication between nanomachines based on its channel capacity performance, advantages, and possible applications for emerging nanonetworks.

1.5 Thesis Outline

This thesis is organized as follows. Chapter 2 presents the physical model of the Gap Junction (GJ) communication. Next, an information theoretical model of the GJ communication channel is introduced. At the end of this chapter, we discuss relations between cardiac diseases and the GJ communication channel parameters. In Chapter 3, we describe the physical model of the diffusion-based Molecular Communication (MC). Then, the sequence detection methods for MC based on maximum a posteriori (MAP) and maximum likelihood (ML) criteria are presented. In addition, a linear and a nonlinear type of equalizers for molecular diffusion channel are presented. The performance of these methods based on bit error rates are evaluated at the end of this chapter. In Chapter 4, we first present the physical models of the point-to-point and waveguide-based Wireless Nanoscale Magneto-Inductive (WNMI) communication methods and underline the governing physical laws and mathematical formulations. Next, we present an information theoretical analysis for both the WNMI communication methods. We conclude this chapter by discussing the performance of the WNMI communication methods based on the numerical analyses of the path loss and channel capacity. In Chapter 5, we explain the basic concepts of magnetocaloric effect (MCE) and underline the governing physical laws. Then, we describe the physical model of the Nanoscale Heat Communication (NHC) and explain how each of the components in the communication model works. Furthermore, we perform an information theoretical analysis of the NHC to determine the closed-form expression for the channel capacity and the signal-to-noise ratio (SNR). We conclude this chapter by presenting numerical analyses of both the channel capacity and the SNR for the NHC channel. In Chapter 6, we conclude the thesis discussing the important research results together with the discussion of future issues.

Chapter 2

NANOSCALE MOLECULAR GAP JUNCTION COMMUNICATION CHANNEL

Molecular communication (MC) is a promising paradigm to communicate at nanoscale and it is inspired by nature. One of the MC methods in nature is the Gap Junction (GJ) communication between cardiomyocytes. The GJ communication is achieved by diffusion of ions through GJ channels between the cells. The transmission of the information is realized by means of the propagation of the Action Potential (AP) signal. Both the probability of the AP propagation failure and the probability of the spontaneous AP initiation are obtained. For the first time in the literature, the GJ communication channel is modeled and analyzed from the information theoretical perspective to find the communication channel capacity. A closed-form expression is derived for the capacity of the GJ communication channel. The channel capacity, propagation delay and information transmission rate are analyzed numerically for a three-cell network. The results of the numerical analyses point out a correlation between an increase in the incidence of several cardiac diseases and a decrease in the channel capacity, an increase in the propagation delay, and either an increase or a decrease in the transmission rate. The method that we use and results that are presented may help in the investigation, diagnosis and treatment of cardiac diseases as well as help in the design of nanodevices communicating via GJ channels.

2.1 Introduction

Nanoscale communication between nanodevices (e.g., engineered organisms or artificial devices) is a novel and interdisciplinary concept including nanotechnology, biotechnology and communication technology [1]. The construction of nanonetworks by interconnecting nanodevices expands the capabilities of single nanodevices by means of cooperation between

them [2, 3]. The realization of the communication between nanodevices can be achieved through electromagnetic, acoustic or molecular communication [4, 5]. The Molecular Communication (MC) concept is defined as the information transmission using molecules and it is inspired by nature [6]-[8]. Several nature-inspired and theoretically modeled MC techniques exist in the literature based on pheromones [6], flagellated bacteria and catalytic nanomotors [2], pollen and spores [6], Förster Resonance Energy Transfer [9], and morphogenesis [10].

An approach for further understanding of the information transmission in a molecular environment is to investigate the MC from the information theoretical perspective. For example, in [11] and [12], the information transfer capacity of the MC, in which propagation of signaling molecules is based on Brownian motion and the number of molecules transmitted or received represents the coded information, is evaluated. In [13], diffusion-based MC is investigated, where information is carried on the frequency of signal molecules. In [14] and [15], a diffusion-based MC is analyzed including several factors affecting the capacity of the channel and an error compensation method for the reliable communication is proposed. In [16], MC based on calcium signaling is investigated by developing an information theoretical model.

In this chapter, for the first time in the literature, the nanoscale MC between ventricular cardiomyocytes is modeled and analyzed based on the information theory to obtain the communication channel capacity. The study presented in this chapter is given in [17]. The communication between the cardiomyocytes is achieved by the transmission of ions through channels in specialized structures of the cell membrane called Gap Junctions (GJs) [18]. This type of communication is called GJ communication. The GJ communication is an approach that have been proposed for the communication of nanodevices. For example, both MC system inspired by cell to cell communications through GJs [19] and MC based on intercellular calcium signaling [20] require utilization of the GJ communication channels for the communication in the nanoscale. However, these studies do not propose a solution for the problem of modeling and analyzing the GJ communication channel from the information theoretical perspective. To model and analyze the GJ communication channel based on the

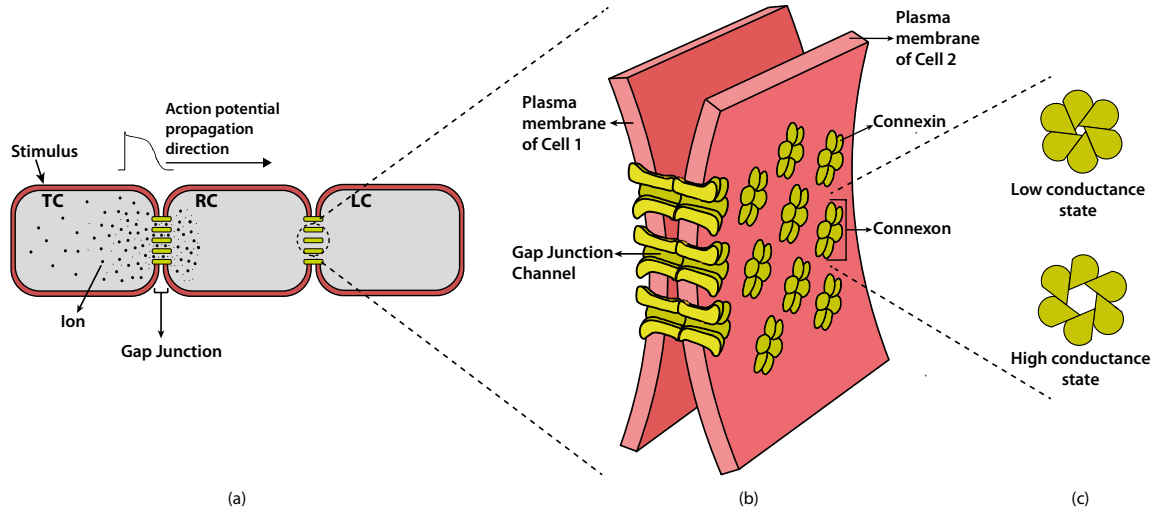


Figure 2.1: A simplified model of the GJ communication and the physical structure of GJs. (a) The GJ communication model. (b) The enlarged section of a GJ including several GJ channels. (c) The top view of a connexon.

information theory, we first introduce the model of the electrical signal propagation and the model of the GJ channels. Then, we combine these models to obtain the failure probability of the electrical signal propagation. In addition, the probability of the spontaneous electrical signal propagation is derived.

The potential models for the GJ communication of nanodevices can be engineered from commonly used techniques such as GJ transfection of cultured HeLa cells with connexin coding DNAs [21] or injection of *Xenopus* oocytes with connexin coding RNAs [22]. Therefore, the construction of the GJ communication channel is an existing technique used widely in physiology experiments. Unlike most of the existing models in the literature, this study presents information theoretical model of an already experimented, physically realizable and hence, realistic nanoscale communication channel. The model presented in this chapter may help in investigation, diagnosis and treatment of cardiac diseases. The information theoretical model can be used in physiology studies of the GJ communication channel to have a broader perspective in the investigations. Furthermore, the model can be utilized in the design and engineering of the GJ communication for nanodevices.

The rest of this chapter is organized as follows. Section 2.2 presents the physical model of the GJ communication. In Section 2.3, an information theoretical model of the GJ communication channel is proposed. Section 2.4 presents a numerical analysis of the channel capacity, the channel propagation delay and the information transmission rate. In Section 2.5, relations between cardiac diseases and the channel capacity, the propagation delay and the information transmission rate are discussed.

2.2 Physical Model of GJ Communication

In the myocardium, i.e., the muscular tissue of the heart, the communication between two cardiomyocytes is achieved by the diffusion of ions at the cell-to-cell contact domain called gap junction (GJ) through pipe-like channels clustered in the GJ known as GJ channels [18]. The nanoscale MC between two cardiomyocytes is called GJ communication. For the rest of the chapter, the GJ channels and the GJ communication channel should not be confused with each other since the former refers to *the physical channels* clustered in a GJ while the latter refers to *the communication channel* formed by the GJ channels clustered in a GJ. To avoid any ambiguity between the physical channels and the communication channel, the communication channel is always denoted by *the GJ communication channel* and the physical channels are denoted by *the GJ channels*. In Fig. 2.1(a), a GJ forming a GJ communication channel between two cardiomyocytes is indicated and in Fig. 2.1(b), several GJ channels clustered in a GJ are shown.

In the GJ communication, the diffusion of ions between cardiomyocytes provides the propagation of the electrical activity called cardiac Action Potential (AP). The AP is initiated by the sinoatrial node, i.e., the impulse-generating tissue of the heart, and is used for the transmission of the information between cardiomyocytes [18]. That is, the information indicating whether cardiomyocytes contract or relax is encoded in the AP pulse train by the sinoatrial node. A cardiomyocyte at rest contracts when an AP pulse is successfully received, which is called excitation-contraction coupling [23]. In contrast, when there is no AP pulse received by a cardiomyocyte, the corresponding cardiomyocyte stays at rest. Fur-

thermore, cardiomyocytes have the so called all-or-none property, i.e., if stimulus is above a threshold voltage, cardiomyocytes give complete response or otherwise they do not respond at all [24]. The contraction and relaxation of the heart as a single unit is the result of synchronous propagation of the APs.

A basic network model of the GJ communication is shown in Fig. 2.1(a). In the model, APs are transmitted by a single transmitter cardiomyocyte (TC), propagated through the GJ by means of the diffusion of the ions, and received by a single receiver cardiomyocyte (RC). The ions diffused from TC to RC continue to diffuse to adjacent unstimulated cardiomyocytes, and this affects the AP initiation at the RC. To have a more realistic GJ communication model, there is also a loading cardiomyocyte (LC) to capture the loading effects of the unstimulated myocytes connected to the RC in the cardiac fiber. TC, RC, and LC are identical. In addition, according to the properties of both cardiomyocytes and the AP propagation stated above, the GJ communication between cardiomyocytes is considered as a binary digital communication with On-Off Keying (OOK) modulation. That is, an AP pulse is considered as binary bit 1 and its absence is considered as binary bit 0.

2.2.1 Action Potential Propagation

The heart beat is generated in the form of electrical activity of the impulse-generating cells of the sinoatrial node. The initiation and the propagation of the electrical activity, i.e., the AP, is the most efficient molecular signal conduction mechanism in the myocardium [23]. The AP initiation in cardiomyocytes is described as follows. If a stimulus causes the membrane potential, i.e., the potential difference across the membrane of the cardiomyocyte, to become less negative than a threshold level, the sodium (Na^+) channels embedded in the membrane open and allow Na^+ ions to enter the cardiomyocyte. This makes the membrane potential to rise at a rate of about $300\text{V}/\text{sec}$ causing depolarization of the membrane. Such a rapid increase in the membrane potential is called upstroke of the AP. As the membrane voltage rises, Na^+ channels close due to a process called inactivation. Next, calcium (Ca^{2+}) and potassium (K^+) channels open, which causes the membrane potential to stay constant; that is, the inward Ca^{2+} current and the outward K^+ current compensate

each other for a while. Then, Ca^{2+} channels close but K^+ channels are still open causing rapid repolarization of the membrane. Finally, the membrane potential is restored to around -85mV . A significant amount of current knowledge about the action potential generation process comes from the studies presented in [25]-[27]. In this chapter, we use the cardiac ventricular action potential generation model given in [26].

The potential difference between the stimulated and the unstimulated adjacent cardiomyocytes causes the ions to drift through the GJ channels leading the synchronous propagation of the AP. That is, the GJ coupling enables the wave of the action potential to propagate from one cardiomyocyte to a neighbor cardiomyocyte by means of diffusion of the ions through the GJ channels. The AP propagation model that we use is presented in [28]. The propagation model assumes that each cardiomyocyte is isopotential, i.e., the membrane potential of each individual cardiomyocyte is the same over its membrane surface. According to the model, the most important factor of the AP propagation is delay for an AP to pass through GJs. For the ion current flowing through the cardiomyocyte membrane, the current balance equation is

$$C_m S \frac{dv_n}{dt} = \frac{1}{R_{gj}}(v_{n+1} - 2v_n + v_{n-1}) + S I_m \quad (2.1)$$

where v_n is the membrane potential for the n th cell in one dimensional cardiac fiber, i.e., the potential difference between inside and outside of the cardiomyocyte, C_m is the membrane capacitance per unit area of the cardiomyocyte membrane, S is the surface area of the membrane, R_{gj} is the total GJ resistance between the cardiomyocytes, and I_m specifies the ionic currents, e.g., Na^+ , Ca^{2+} , and K^+ currents, per unit area of the membrane described in detail in [26], [27]. We use the piecewise linear approximation of I_m given in [28] as

$$I_m(v) = \begin{cases} \frac{\alpha_1(V_1 - v)}{R_m}, & v < V^* \\ \frac{\alpha_2(V_2 - v)}{R_m}, & V^* < v \end{cases} \quad (2.2)$$

where R_m is the membrane resistivity, V_1 is the resting potential of the cardiomyocyte membrane, V_2 is the sodium equilibrium potential, V^* is the activation threshold voltage for Na^+ current, and α_1 and α_2 are constants chosen properly such that for $V_1 < v < V_2$, area

under both the piecewise linear function and the approximated function are the same [28]. The parameter values of (2.2) are taken as $V_1 = -87mV$, $V_2 = 28.8mV$, $V^* = -34.8mV$, $\alpha_1 = 1$, and $\alpha_2 = 108$ from the results of the AP model based on the formalism presented in [29, 30]. The piecewise linear function with the given numerical values captures the numerical features of the dynamics of the AP upstroke [28].

The most important deduction that can be extracted from (2.1) is that the propagation fails if R_{gj} is sufficiently large. That is, an increase in R_{gj} causes a decrease in the number of the diffused ions. The less number of ions may not be enough to increase the membrane potential of RC above the threshold value. The critical GJ resistance between TC and RC is denoted by R_{gj}^* and RC has an infinite voltage threshold if $R_{gj} > R_{gj}^*$. In [28], an expression is given for R_{gj}^* as

$$R_{gj}^* = L\sqrt{\frac{\Gamma R_m}{S}} \left[\frac{E_2^2 - 2\mu_2 E_2 + 1}{(1 - E_2^2)\sqrt{\alpha_2}} + \left(\frac{V_2 - V^*}{V_1 - V^*} \right) \frac{E_1^2 - 2\mu_1 E_1 + 1}{(1 - E_1^2)\sqrt{\alpha_1}} \right] \quad (2.3)$$

where L is the length of the cardiomyocyte, and Γ , E_1 , and E_2 are variables defined as

$$\Gamma = (R_i/V_i) + (R_e/V_e) \quad (2.4)$$

$$E_k = \exp\left(\sqrt{(\alpha_k \Gamma L^2 S)/R_m}\right), \quad k = 1, 2 \quad (2.5)$$

where R_i and R_e are the cytoplasmic and extracellular medium resistivity values, respectively, V_i is the volume of the cytoplasm of the cardiomyocyte, and V_e is the volume of the extracellular medium that surrounds the cardiomyocyte in the myocardium. The values of α_1 , α_2 , V_1 , V_2 , and V^* that we use in our work are as the same as the values given above. μ_1 and μ_2 satisfy the equality $R_{gj}^* = R_{gj}$ where R_{gj} is

$$R_{gj} = 2L\sqrt{\frac{\Gamma R_m}{\alpha_k S}} \frac{\left(\mu_k - \frac{1}{E_k}\right) (\mu_k - E_k)}{\mu_k \left(E_k - \frac{1}{E_k}\right)}, \quad k = 1, 2. \quad (2.6)$$

Numerical result of R_{gj}^* is found by solving two nonlinear equations which are $R_{gj}^* = R_{gj}$ for $k = 1$ and $R_{gj}^* = R_{gj}$ for $k = 2$. The upper limit of the GJ resistance for the successful propagation is R_{gj}^* since the AP propagation strictly fails if $R_{gj} > R_{gj}^*$ as stated above.

2.2.2 Physical Model of Gap Junction Channels

The GJs include the GJ channels that form a connection between neighboring cells in many tissues and organs providing chemical and electrical MC [18]. The length and diameter of a complete GJ channel is approximately $10 - 15nm$ and $2 - 3nm$, respectively [31]. Therefore, the GJ communication takes place at nanoscale. The physical structure of a GJ channel is formed by two hemichannels called connexons and they are embedded in the membrane of the connected cells. Furthermore, each hemichannel includes six transmembrane proteins called connexins that are oligomerized in a hexameric structure to form a pore. Two hemichannels belonging to adjacent cells interact to form a complete GJ channel. The structure of GJ channels in a GJ can be seen in Fig. 2.1(b). The GJ channels have an evident selectivity for particle passage based on the permeability of the GJ channels and size of the particles. Thus, the AP propagation between cardiomyocytes depends on the permeability of the GJ channels since the diffusion of the ions is affected by the permeability of the GJ channels [31].

According to the stochastic behavior of the GJ channels [32], a GJ channel have two voltage-sensitive gates in series and one gate is located in each hemichannel. The channel gates control the GJ permeability and each gate has two states: an open state resulting in a high conductance and a closed state resulting in a low conductance for a hemichannel [32] as shown in Fig. 2.1(c). The voltage-sensitive gates control the channel conductance state in accordance to junctional voltage, i.e., potential difference between the membrane potentials of two adjacent cardiomyocytes denoted by V_j , in a stochastic manner. Hence, the gates associated with each connexon can be used to describe the stochastic GJ channel dynamics. At any instant a GJ channel can be in any one of four states:

- **HH state:** both gates are open
- **HL state:** one gate is open and the other gate is closed
- **LH state:** one gate is open and the other gate is closed
- **LL state:** both gates are closed

The occurrence of the LL state, however, is very rare [33] and such a state has a very small conductance compared with the other states; thus, we choose to include only the first three states by neglecting the LL state. The stochastic dynamics of the GJ channels given in [32] is described by probabilities of a channel being in any of HH, HL and LH states, denoted by p_{HH} , p_{HL} , and p_{LH} , respectively, given as follows

$$p_{HH} + p_{LH} + p_{HL} = 1 \quad (2.7)$$

$$\begin{aligned} \frac{dp_{LH}}{dt} &= \beta_1(V_j) \cdot p_{HH} - \alpha_1(V_j) \cdot p_{LH} \\ \frac{dp_{HL}}{dt} &= \beta_2(V_j) \cdot p_{HH} - \alpha_2(V_j) \cdot p_{HL} \end{aligned} \quad (2.8)$$

where V_j is the junctional voltage, $\alpha_1(V_j)$, $\alpha_2(V_j)$, $\beta_1(V_j)$ and $\beta_2(V_j)$ are the rate constants of the state transitions as demonstrated in Fig. 2.2. The rate constants are given as

$$\begin{aligned} \alpha_1(V_j) &= \lambda \exp(-A_\alpha(V_j - V_0)) \\ \alpha_2(V_j) &= \lambda \exp(A_\alpha(V_j + V_0)) \\ \beta_1(V_j) &= \lambda \exp(A_\beta(V_j - V_0)) \\ \beta_2(V_j) &= \lambda \exp(-A_\beta(V_j + V_0)) \end{aligned} \quad (2.9)$$

where V_0 is the junctional voltage at which the opening and closing rates of the GJ channel gates have the same common value λ , and A_α and A_β are constants that indicate the sensitivity of a GJ channel to the junctional voltage [32]. Since connexin43 GJ protein is the major GJ protein in the ventricular muscle [34], in the numerical analysis, we use data obtained experimentally for the connexin43 GJ protein. Thus, we use the constants as $\lambda = 0.69$, $A_\alpha = 0.04(mV)^{-1}$, $A_\beta = 0.07(mV)^{-1}$, and $V_0 = 62mV$ adopted from experimental studies of connexin43 GJ protein [35].

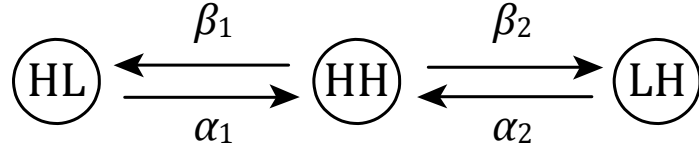


Figure 2.2: The kinetic behavior of a GJ channel modeled by a state machine with three states, i.e., HH, HL, and LH. The rate constants β and α refer to the forward reactions high to low and the backward reactions low to high, respectively.

2.2.3 Action Potential Propagation Failure

The conductance of each GJ channel, denoted by G_{ch} , is a random variable whose probability mass function is

$$f_G(G_{ch}) = \begin{cases} p_{HH}, & \text{if } G_{ch} = G_{HH} \\ p_{HL}, & \text{if } G_{ch} = G_{HL} \\ p_{LH}, & \text{if } G_{ch} = G_{LH} \end{cases} \quad (2.10)$$

where G_{HH} , G_{HL} , and G_{LH} are the conductance values of a single GJ channel in the respective state [32]. In this study, we use the GJ channel conductance values as $G_{HH} = 73pS$, $G_{HL} = 12pS$, and $G_{LH} = 12pS$, which are experimental results for connexin43 type GJ protein [34]. Since the GJ channels in a GJ are connected in parallel, the total conductance of the GJ having n_{HH} , n_{HL} , and n_{LH} GJ channels in HH, HL, and LH states, respectively, is given as

$$G_{gj}(V_j) = n_{HH} \cdot G_{HH} + n_{HL} \cdot G_{HL} + n_{LH} \cdot G_{LH}. \quad (2.11)$$

For a GJ consisting of N GJ channels, probability that there are n_{HH} , n_{HL} , and n_{LH} GJ channels in HH, HL, and LH states, respectively, is found by multinomial distribution

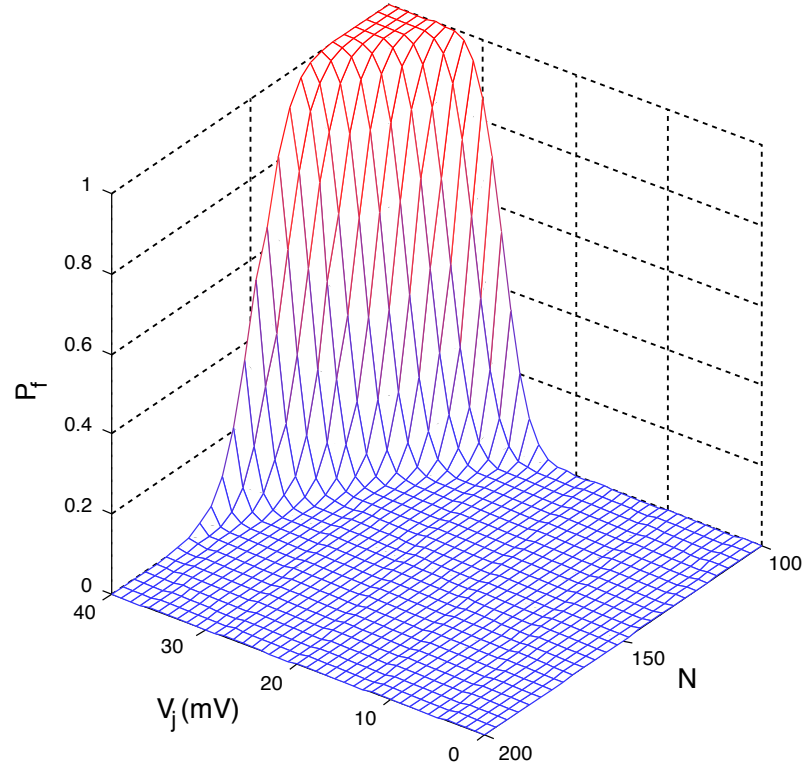


Figure 2.3: P_f plot with respect to the junctional voltage V_j and the total number of the GJ channels in a GJ, N . For the other parameters, the typical physiological values are used which are $L = 100\mu m$, $r = 11\mu m$, $R_i = 250\Omega cm$, $R_e = 100\Omega cm$, $R_m = 20k\Omega cm^2$, and $V_e = V_i/5$ adopted from [26, 40].

function given by

$$Pr\{G_{gj}(V_j) = n_{HH} \cdot G_{HH} + n_{HL} \cdot G_{HL} + n_{LH} \cdot G_{LH}\} = \begin{cases} N! \frac{p_{HH}^{n_{HH}} \cdot p_{LH}^{n_{LH}} \cdot p_{HL}^{n_{HL}}}{n_{HH}! \cdot n_{LH}! \cdot n_{HL}!}, & \text{if } n_{HH} + n_{LH} + n_{HL} = N \\ 0, & \text{otherwise.} \end{cases} \quad (2.12)$$

Assume that a GJ includes N GJ channels and they are distributed such that the number of the GJ channels in HH, HL, and LH states are n_{HH} , n_{HL} , and n_{LH} , respectively. Then,

the total number of different combinations of n_{HH} , n_{HL} , and n_{LH} satisfying $n_{HH} + n_{LH} + n_{HL} = N$ can be found in the following manner. Firstly, the selection of $n_{HH} = N$, $n_{HL} = 0$, and $n_{LH} = 0$ gives one combination. Secondly, for $n_{HH} = N - 1$, there are two possible combinations: $n_{HL} = 0$, $n_{LH} = 1$ and $n_{HL} = 1$, $n_{LH} = 0$. Next, for $n_{HH} = N - 2$, there are three possible combinations: $n_{HL} = 0$, $n_{LH} = 2$, $n_{HL} = 1$, $n_{LH} = 1$, and $n_{HL} = 2$, $n_{LH} = 0$. If we continue in a similar way, for $n_{HH} = 0$, there are $(N + 1)$ combinations. As a result, the total number of different combinations is given by $1 + 2 + 3 + \dots + (N + 1) = \frac{1}{2}(N + 1)(N + 2)$. For each combination, the total conductance value and the probability of the corresponding combination is given in (2.11) and (2.12), respectively. We use MATLAB to obtain the probability mass function of the total conductance of a GJ having total N GJ channels by evaluating all possible channel state combinations and the corresponding probabilities.

Since the propagation of the AP fails when the GJ conductance value, $G_{gj}(V_j)$, is less than the critical conductance value, G_{gj}^* , we can find the probability of the propagation failure, denoted by P_f , using the probability mass function of the GJ conductance as follows

$$P_f = Pr\{G_{gj}(V_j) < G_{gj}^*\} \quad (2.13)$$

where the critical conductance is the reciprocal of the critical resistance, $G_{gj}^* = 1/R_{gj}^*$. The failure probability P_f depends on several parameters such as the critical GJ conductance G_{gj}^* , the junctional voltage V_j , and the number of the GJ channels N , as clearly observed in (2.8), (2.12), and (2.13). In Fig. 2.3, the variation of P_f with N and V_j is shown. For constant N , an increase in V_j does not severely affect P_f at low V_j ; however, for $V_j > 30mV$, an increase in V_j significantly increases P_f . The increase in P_f at high V_j is due to the decrease in the GJ conductance caused by increased closure rates and decreased opening rates of the GJ hemichannels for $V_j > V_0$ as given in (2.9). Therefore, at higher V_j , P_f is higher than P_f at low V_j . In addition, at constant V_j , an increase in N decreases P_f as seen in Fig. 2.3 because conductance of the GJ increases with increasing N as given in (2.11).

The relation between the AP propagation and the stochastic behavior of the GJ channels is described as follows. In Section II-A, it is shown that the success and the failure of the AP propagation depends on the total GJ resistance R_{gj} between two cardiomyocytes. That is, if R_{gj} is larger than the critical GJ resistance R_{gj}^* , the AP propagation between two

cardiomyocytes fails, otherwise the AP propagates successfully. On the other hand, the total GJ conductance is a function of the junctional voltage V_j as stated in Section II-B and II-C. Since the AP propagation creates a junctional voltage on the GJ channels, R_{gj} alters during the AP propagation according to the behavior of the voltage-depended GJ channel gates. Therefore, the AP propagation model and the stochastic model of the GJ channels are interrelated and they are two fundamental models to describe the communication between cardiomyocytes.

2.2.4 Spontaneous Action Potential Initiation

The AP initiation in a cardiomyocyte is caused by the diffusion of the ions from the stimulated cardiomyocyte to the unstimulated neighbor cardiomyocyte through the GJ channels in the GJ. That is, the diffusion of ions stimulates the neighbor cardiomyocyte. However, the AP generation can be triggered in the absence of a stimulus due to some abnormalities of cardiomyocytes such as Early Afterdepolarizations (EADs) and Delayed Afterdepolarizations (DADs) [27]. Although normal and healthy ventricular cardiomyocytes do not exhibit such spontaneous generation of the AP [36], we incorporate the spontaneous AP generation into the GJ communication model considering diseased cardiomyocytes.

The spontaneous AP initiation in a cardiomyocyte can be triggered by the Ca^{2+} release units (CRUs) of the sarcoplasmic reticulum [37]. If a CRU fires, it emits a Ca^{2+} ion spark into the cytoplasm of the cardiomyocyte. The emitted Ca^{2+} ions increase the membrane potential of the cardiomyocyte. Therefore, if the membrane potential becomes greater than a threshold due to the released Ca^{2+} ions by CRUs, an AP is triggered in the cardiomyocyte without an external stimulus. The probability that a CRU fires in the time duration T_s is

$$P_s = 1 - \exp\left(-\frac{P_{max}\rho^n}{K^n + \rho^n}T_s\right) \quad (2.14)$$

where P_{max} is the maximum probability of Ca^{2+} spark occurrence/CRU/unit time, ρ is the free Ca^{2+} molar concentration in the cytoplasm, K is the Ca^{2+} sensitivity parameter and n is the Hill coefficient [37]. Let the number of the CRUs that fire in time T_s be m . Assuming the CRUs are independent of each other, m is distributed by the binomial

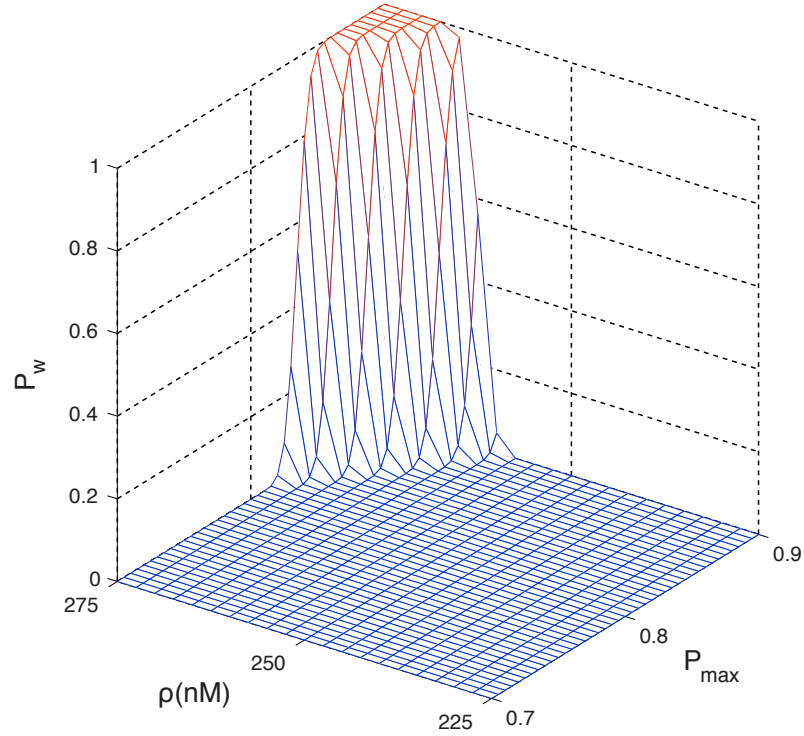


Figure 2.4: P_w plot with respect to ρ and P_{max} . The other parameters are $K = 15\mu M$, $M = 30000$, $n = 1.6$, and $T_s = 500msec$ [37].

probability distribution as $m \sim B(M, P_s)$ where M is the total number of the CRUs in a cardiomyocyte. That is,

$$\Pr\{m \text{ sparks}\} = \binom{M}{m} P_s^m (1 - P_s)^{M-m}. \quad (2.15)$$

Since M is a large number, we can use the Gaussian approximation of the binomial distribution given in (2.15) as

$$m \sim \mathcal{N}(MP_s, MP_s(1 - P_s)). \quad (2.16)$$

The number of Ca^{2+} sparks should be large enough to initiate an AP. In the GJ communication model, we use the half of the number of the CRUs as the required number of sparks to trigger an AP in T_s duration. Thus, the probability of an AP initiation without

any stimulus, denoted by P_w , is

$$P_w = \Pr\left\{\frac{M}{2} < m\right\} = Q\left(\frac{(M/2) - MP_s}{MP_s(1 - P_s)}\right) \quad (2.17)$$

where $Q(\cdot)$ is the Q -function. Since the distribution of m is approximated by Gaussian distribution, we can use Q -function to describe the probability given in (2.17). In Fig. 2.4, P_w with respect to both ρ and P_{max} is plotted. An increase in P_{max} causes an increase in P_s . Thus, an increase in P_{max} causes an increase in the expected number of the emitted Ca^{2+} sparks which increases the probability of the initiation of an AP as seen in Fig. 2.4. Furthermore, since increasing the free Ca^{2+} concentration ρ in the cardiomyocyte cytoplasm increases P_s , an increase in ρ due to the Ca^{2+} concentration fluctuations increases the spontaneous AP initiation probability.

2.3 Information Theoretical Analysis of Gap Junction Communication Channel

The GJ communication channel between TC and RC as illustrated in Fig. 2.1(a) is modeled from the information theoretical perspective. The cardiac APs are used for the information transmission between TC and RC. An AP pulse represents bit 1 and the absence of the AP pulse represents bit 0. For the information theoretical model, we consider two cases to figure out the transmission probabilities of the information from TC to RC. The first case is the failure of the AP transmission; that is, RC detects bit 0 while bit 1 is transmitted by TC. The probability of the first case is P_f given in (2.13). The second case is the initiation of the AP at RC in the absence of a stimulus caused by TC; that is, RC detects bit 1 while bit 0 is transmitted by TC. The probability of the second case is P_w given in (2.17). The AP propagation failure and the spontaneous AP initiation are caused by the noise factors that intrinsically arise in the GJ communication. The intrinsic noise factors are related to the stochastic nature of both the GJ channels and the CRUs. Therefore, the information theoretical channel model of the GJ communication includes the peculiar noises and the noise factors specific to the GJ communication.

The GJ communication channel exhibits Binary Asymmetric Channel (BAC) character-

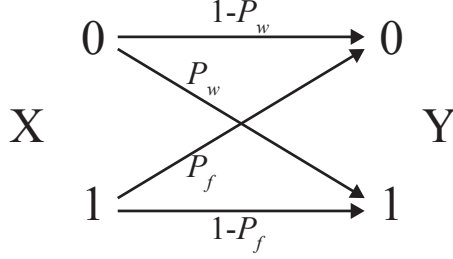


Figure 2.5: The GJ communication channel transmission diagram with the transmission probabilities. The communication channel expresses binary asymmetric channel (BAC) characteristics.

istics with On-Off Keying (OOK) modulation and it is represented in Fig. 2.5 based on the analysis that we introduced so far. Also, the communication channel has memoryless characteristics because of the fact that when the membrane voltage returns to its steady state value at the end of an AP transmission, the voltage-dependent state probabilities of the GJ channels returns to their steady state values. Thus, afterwards if another AP is transmitted, the initial conditions for the probabilities of the GJ channel states are the same as the previous transmission.

Assume that X is the transmitted bit by TC and Y is the received bit by RC. Then, we define the AP transmission probability of TC as P_{AP} , i.e.,

$$P(x) = \begin{cases} P_{AP}, & \text{if } X = 1 \\ 1 - P_{AP}, & \text{if } X = 0. \end{cases} \quad (2.18)$$

Using (2.18) and the channel transmission probabilities seen in Fig. 2.5, the joint probability distribution of X and Y , denoted by $P(x, y)$, is given as

$$P(x, y) = \begin{cases} (1 - P_{AP})(1 - P_w), & \text{if } (X = 0, Y = 0) \\ (1 - P_{AP})P_w, & \text{if } (X = 0, Y = 1) \\ P_{AP}P_f, & \text{if } (X = 1, Y = 0) \\ P_{AP}(1 - P_f), & \text{if } (X = 1, Y = 1) \end{cases} \quad (2.19)$$

The joint distribution $P(x, y)$ expresses the probability of that the observed output symbol

is y and the transmitted symbol is x . The mutual information between X and Y denoted by $I(X; Y)$ is given in [38] as follows

$$I(X; Y) = \sum_{x,y} P(x, y) \log_2 \frac{P(x, y)}{P(x)P(y)} \quad (2.20)$$

where $P(y)$ is the probability distribution of Y . To obtain $P(y)$ is straightforward using the joint distribution $P(x, y)$. The GJ communication channel capacity denoted by C_{gj} is the maximum value of the mutual information [38] and the capacity of the GJ communication channel is found as follows

$$C_{gj} = \max_{P(x)} I(X; Y) = \frac{(1 - P_w)H(P_f) - P_f H(1 - P_w)}{P_f + P_w - 1} + \log_2 \left(1 + 2 \frac{H(1 - P_w) - H(P_f)}{P_f + P_w - 1} \right) \quad (2.21)$$

where $H(\cdot)$ is the binary entropy function defined as

$$H(p) = -p \log_2 p - (1 - p) \log_2 (1 - p). \quad (2.22)$$

The channel characteristics of the GJ communication varies with several parameters such as the number of the GJ channels, the membrane resistivity, the cell length and radius. Since such physiological properties vary among individual organisms and even among different sites on the same heart, in the next section, we analyze the GJ communication channel characteristics with respect to several physiological parameters.

2.4 Numerical Analysis

In this section, we present a numerical analysis of the GJ communication parameters namely the channel capacity, the propagation delay, and the information transmission rate to show how these parameters change with the properties of cardiomyocytes and GJs. The results of the analysis can be used in the investigation of the biological properties of the GJ coupled cardiomyocytes as well as in the design of nanodevices that use the GJ communication channel.

For the numerical analysis, we model the cardiomyocyte membranes using the model presented in [26]. The propagation of the AP is simulated in a three-cell fiber as illustrated in Fig. 2.1(a). A stimulus is applied to TC to initiate the AP propagation. After

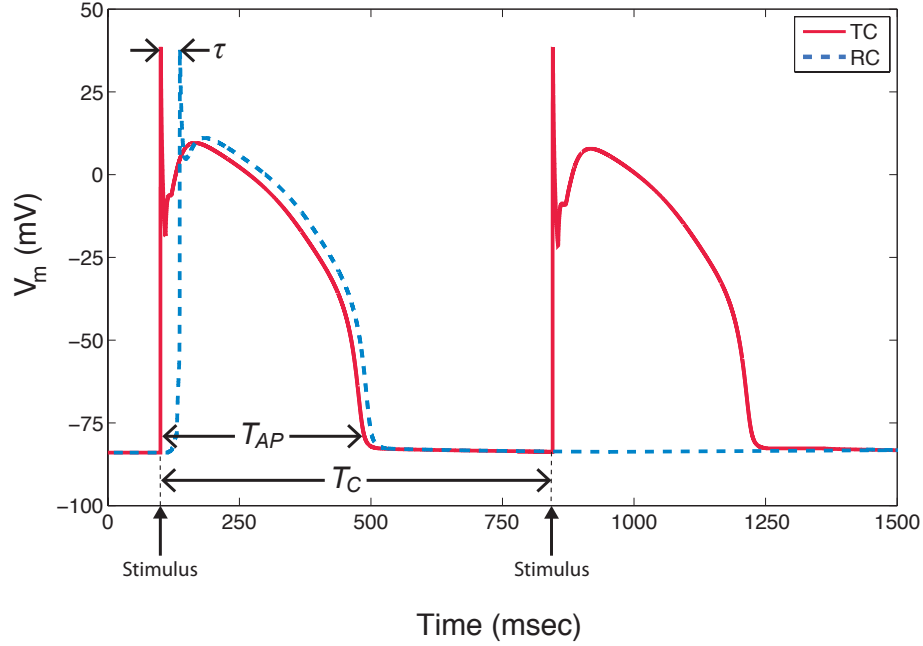


Figure 2.6: An illustration for a successful and a failed AP transmissions between TC and RC. Time instants of two stimuli that are applied to TC and the membrane potential changes of TC and RC are shown. The simulation parameters are $N = 110$, $L = 100\mu m$, $r = 11\mu m$, $R_i = 250\Omega cm$, $R_e = 100\Omega cm$, $R_m = 20k\Omega cm^2$, $\rho = 100nM$, $P_{max} = 0.3$, $M = 30000$, $n = 1.6$, $T_s = T_{AP}$, $V_e = V_i/5$ [26, 37, 40].

exciting TC, an AP propagates to RC through the GJ between TC and RC. Since the occurrence probabilities of the GJ channel states depend on the junctional voltage between cardiomyocytes, we simulate the AP propagation by using the expected value of the total GJ conductance. For discrete time steps $\Delta t = 0.01ms$, the junctional voltage is found as the difference between the membrane voltages of TC and RC. Then, at the obtained junctional voltage, the expected value of the total conductance is evaluated and replaced with the previous total conductance value assuming the total GJ conductance is constant for $\Delta t = 0.01ms$. The expected value of the total conductance is

$$E[G_{gj}(V_j)] = E[NG_{ch}] = N(p_{HH}G_{HH} + p_{HL}G_{HL} + p_{LH}G_{LH}) \quad (2.23)$$

where the expectation of G_{ch} is found by using the probability mass function of the single GJ channel conductance in (2.10). After simulating the AP propagation by using the

Table 2.1: Simulation Parameters

<i>Parameter</i>	<i>Symbol</i>	<i>Value Range</i>
Number of GJ channels	N	105 – 120
Cardiomyocyte length	L	90 – 105 μm
Cardiomyocyte radius	r	10.0 – 11.5 μm
Membrane resistivity	R_m	19 – 20k Ωcm^2
Free Ca ²⁺ concentration	ρ	590 – 600nM

expectation of G_{gj} given in (2.23), we use the junctional voltage between TC and RC membranes for the channel capacity analysis.

An example of a successful and a failed transmission of APs between TC and RC can be seen in Fig. 2.6 which illustrates the membrane voltage changes of TC and RC over time. The channel propagation delay, denoted by τ , is the delay between the upstrokes of the action potentials generated in TC and RC. The AP pulse duration, denoted by T_{AP} , is the time duration between the AP initiation instant and the time that the membrane potential is restored to its initial value. The cycle length, denoted by T_C , is the time between two successive stimuli that are applied to TC. That is, T_C is the signaling interval of TC. Therefore, the information transmission rate, denoted by R , is given by $R = 1/T_C$. In Fig. 2.6, the channel propagation delay τ , the AP pulse duration T_{AP} , and the cycle length T_C can be seen.

The junctional voltage attained from the simulation is used to evaluate p_{HH} , p_{HL} , and p_{LH} by using (2.7) and (2.8). Since the junctional voltage V_j is time varying and the probabilities depend on V_j , time average of the probabilities are used for (2.12). The numerical analysis of the mutual information expression in (2.20) is performed with the parameters given in Table 2.1. However, the derivations of mathematical expressions for both the channel propagation delay τ and the action potential pulse duration T_{AP} are too complex because of the nonlinear and stochastic nature of the membrane ion channels generating the AP [26]. Therefore, the numerical values of τ and T_{AP} are obtained from the simulation results of the AP generation model as performed in the physiological investigations [39]. The numer-

ical analysis is conducted on MATLAB. For the analysis, we keep the following parameters constant at their typical physiological values which are $R_i = 250\Omega cm$, $R_e = 100\Omega cm$ [40], $P_{max} = 0.3$, $M = 30000$, $n = 1.6$ [37] and we assume $V_i = 5V_e$ and $T_s = T_{AP}$.

2.4.1 Channel Capacity

2.4.1.1 Effect of Number of Gap Junction Channels

For the first analysis, we investigate the effect of the number of the GJ channels N in the GJ on the capacity of the GJ communication channel C_{gj} . The analysis is carried out for the GJ between TC and RC for which the number of the GJ channels are varied from $N = 105$ to $N = 120$. We set the rest of the parameters as $L = 100\mu m$, $r = 11\mu m$, $R_m = 20k\Omega cm^2$ and $\rho = 100nM$ [26, 37, 40]. The critical GJ conductance value for the given parameter set is $G_{gj}^* = 5.80nS$ found by using (2.3). In Fig. 2.7(a), the mutual information $I(X;Y)$ is shown with varying AP generation probability P_{AP} for different number of the GJ channels. A change in the number of the GJ channels clustered in the GJ affects directly the conductance of the GJ. Therefore, a lower number of the GJ channels results in a smaller conductance value which causes P_f to become larger and it can be seen in Fig. 2.3. In other words, less number of the GJ channels makes the transmission of bit 1 more erroneous; thus, the capacity of the GJ communication channel decreases accordingly as seen in Fig. 2.7(a). For $N = 105$, the capacity is $C_{gj} = 0.19bit/use$ attained with $P_{AP} = 0.39$ and for $N = 120$, the capacity is $C_{gj} = 0.97bit/use$ attained with $P_{AP} = 0.49$. For N greater than 120, the capacity saturates and becomes $C_{gj} = 1bit/use$. Thus, the channel capacity of the GJ communication designed for nanodevices can be increased with an increase in the number of the GJ channels.

2.4.1.2 Effect of Cardiomyocyte Length

In this analysis, we examine the GJ communication channel capacity variation with the length of cardiomyocytes, L . We change the value of L while keeping the other parameters constant for $N = 110$, $r = 11\mu m$, $R_m = 20k\Omega cm^2$, and $\rho = 100nM$ [26, 37, 40]. The

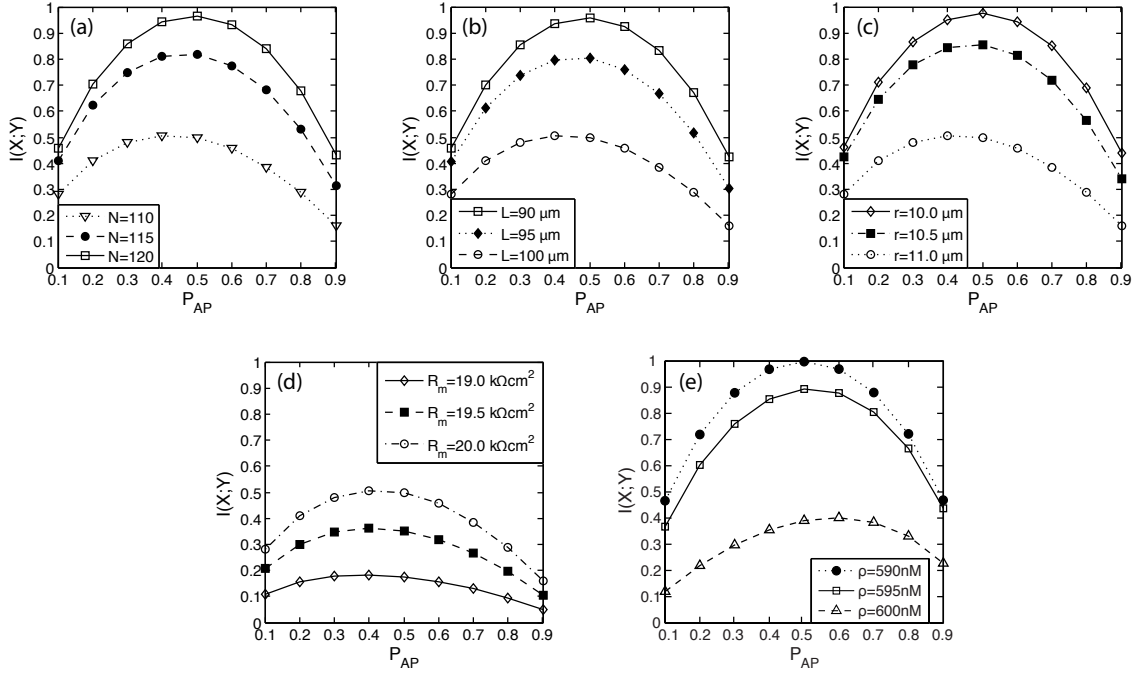


Figure 2.7: $I(X;Y)$ in *bit* for several (a) number of the GJ channels, N , (b) length of the cardiomyocyte, L , (c) radius of the cardiomyocyte, r , (d) the membrane resistivity of the cardiomyocyte, R_m , and (e) the free Ca^{2+} concentration in the cytoplasm, ρ , with varying P_{AP} .

change of the mutual information $I(X;Y)$ with varying AP generation probability of TC for different L values is shown in Fig. 2.7(b). The typical length of a ventricular cardiomyocyte is $L = 100\mu\text{m}$ and for this length, $C_{gj} = 0.51\text{bit}/\text{use}$ is reached with $P_{AP} = 0.42$. For lengths larger than $100\mu\text{m}$, the critical conductance value increases as a result of (2.3). Thus, the increase in the critical conductance value yields an increase in P_f and hence a dramatical decrease in the capacity. The capacity reduction due to an increase in the length can be seen in Fig. 2.7(b). For $L = 105\mu\text{m}$, we find $C_{gj} = 0.21\text{bit}/\text{use}$ reached with $P_{AP} = 0.39$, and for $L = 90\mu\text{m}$, we find $C_{gj} = 0.96\text{bit}/\text{use}$ reached with $P_{AP} = 0.49$. Therefore, the capacity of the GJ communication channel between shorter cardiomyocytes is higher than the capacity between longer cardiomyocytes. As a result, the capacity of the GJ communication used for the communication of nanodevices can be improved by using

short nanodevices.

2.4.1.3 Effect of Cardiomyocyte Radius

The effect of the radius of the cardiomyocytes on the GJ communication channel capacity is investigated by changing the value of the radius r , while setting the other parameters as $N = 110$, $L = 100\mu m$, $R_m = 20k\Omega cm^2$ and $\rho = 100nM$ [26, 37, 40]. To understand change of the channel capacity with respect to r , we compute $I(X;Y)$ for different values of r with varying AP generation probability. The result of the analysis is shown in Fig. 2.7(c). The capacity decreases significantly with increasing r . For example, we find for $r = 10\mu m$, $C_{gj} = 0.98bit/use$ attained with $P_{AP} = 0.49$ and for $r = 11.5\mu m$, $C_{gj} = 0.16bit/use$ attained with $P_{AP} = 0.38$. As a result, the GJ communication channel between the thinner cardiomyocytes has larger capacity compared to the thicker cardiomyocytes. Thus, using thin nanodevices can increase the capacity the GJ communication between nanodevices.

2.4.1.4 Effect of Membrane Resistivity of Cardiomyocyte

We investigate the effect of the membrane resistivity R_m of cardiomyocytes on the GJ communication channel capacity. The membrane resistivity plays a critical role for the AP initiation and the propagation as described in the Section II-A. Only R_m value is changed and the other parameters are set to $N = 110$, $L = 100\mu m$, $r = 11\mu m$ and $\rho = 100nM$ [26, 37, 40]. An increase in R_m decreases the critical conductance value given in (2.3); therefore, increasing R_m yields a reduction in P_f and hence an increase in the channel capacity. The increase in the channel capacity because of the increase in R_m can be seen in Fig. 2.7(d). The results of the numerical analysis show that for $R_m = 19k\Omega cm^2$, $C_{gj} = 0.18bit/use$ achieved with $P_{AP} = 0.38$ and for $R_m = 20k\Omega cm^2$, $C_{gj} = 0.51bit/use$ achieved with $P_{AP} = 0.42$. As a result, the GJ communication between cardiomyocytes having higher membrane resistivity also has higher channel capacity. Hence, the channel capacity of the GJ communication designed for nanodevices can be increased by using membranes with high resistivity values.

2.4.1.5 Effect of Free Calcium Concentration

In this part, we investigate the effect of the free Ca^{2+} concentration ρ in the cytoplasm of the cardiomyocytes on the GJ communication channel capacity. In this analysis, we use the parameter values as $N = 1000$, $L = 100\mu\text{m}$, $r = 11\mu\text{m}$ and $R_m = 20k\Omega\text{cm}^2$ [26, 40]. In Fig. 2.7(e), the mutual information $I(X;Y)$ is shown for different concentration ρ values. An increase in the free Ca^{2+} concentration increases the probability of the spontaneous AP wave initiation P_w as stated in Section 2.2.4. Therefore, increasing the free Ca^{2+} concentration decreases the capacity of the GJ communication channel C_{gj} given in (2.21). For example, we find $P_w = 2.98 \times 10^{-4}$ and $C_{gj} = 0.99\text{bit/use}$ for $\rho = 590\text{nM}$ and $P_w = 0.41$ and $C_{gj} = 0.40\text{bit/use}$ for $\rho = 600\text{nM}$. That is, if fluctuations in the free Ca^{2+} concentration result in $\rho > 590\text{nM}$, the capacity of the GJ communication channel is reduced significantly. Thus, we can say that high Ca^{2+} concentration in the cytoplasm causes more erroneous transmission of the information due to increased P_w .

2.4.2 Channel Propagation Delay

An AP pulse transmitted by TC to RC propagates through the GJ channels between TC and RC. During the AP propagation, the membrane voltage changes with time as shown in Fig. 2.6. As illustrated in the figure, there is a propagation delay τ . In Fig. 2.8, variation of the propagation delay with respect to the number of the GJ channels is shown. We use the typical physiological values for the remaining parameters which are $L = 100\mu\text{m}$, $r = 11\mu\text{m}$, $R_m = 20k\Omega\text{cm}^2$ and $\rho = 100\text{nM}$ [26, 37, 40]. The delay of the AP propagation from TC to RC decreases with increasing the number of the GJ channels. We find $\tau = 11.58\text{ms}$ for $N = 100$, and $\tau = 0.56\text{ms}$ for $N = 1600$. Furthermore, the delay shows an abrupt decrease for increasing N from 100 to 300, and further increasing N causes the delay to decrease slowly. For N less than 300, the coupling between TC and RC is so weak that increasing N leads a large decrease in τ . On the other hand, for N larger than 300, TC and RC are well coupled so that increasing N slightly decreases τ . Consequently, we can say that further increasing N saturates the channel propagation delay to the propagation delay of

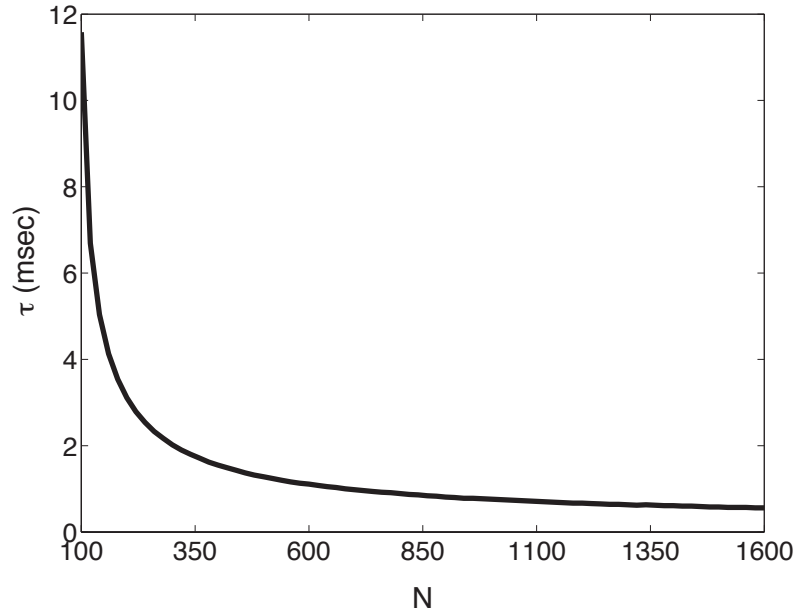


Figure 2.8: The channel propagation delay, τ , between TC and RC with respect to the number of the GJ channels in the GJ, N .

the cytoplasm of the cardiomyocyte, i.e., the effect of discreteness of the cardiac fiber due to the GJ connections diminishes.

2.4.3 Information Transmission Rate

We model the GJ communication between two cardiomyocytes, i.e., TC and RC, as a binary digital communication with OOK modulation as stated previously. Assuming the cycle length is the same as the AP duration, i.e., $T_C = T_{AP}$, the information transmission rate, R , in *bit/sec* for the GJ communication is given as $R = \frac{1}{T_{AP}}$ where T_C and T_{AP} are the cycle length and the AP duration, respectively, as shown in Fig. 2.6. The AP generation in a cardiomyocyte is achieved by the voltage dependent conductance of the ion channels embedded in the membrane as explained in Section II-A. In Fig. 2.9, T_{AP} and R with respect to the maximum conductance of the calcium channels, denoted by \bar{G}_{Ca} , is shown. T_{AP} variation for different \bar{G}_{Ca} values is found from the simulation results of the cardiac

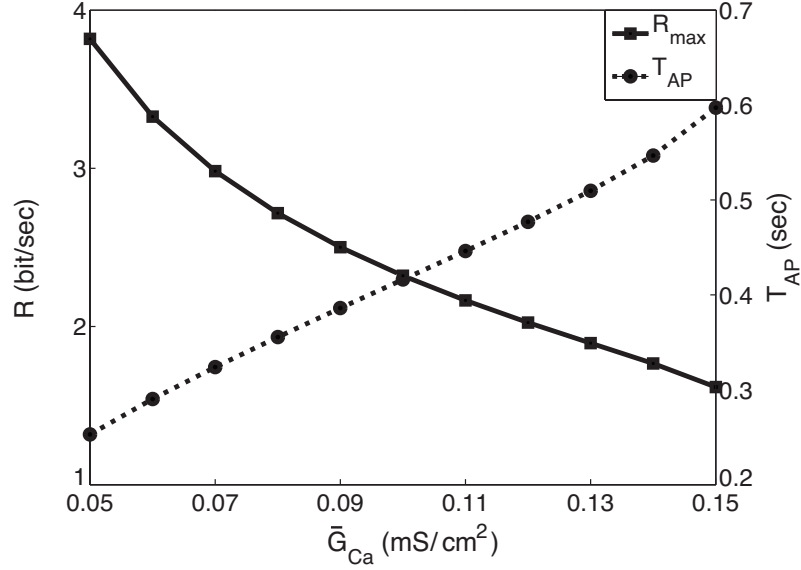


Figure 2.9: The information transmission rate, R , and the AP duration, T_{AP} , with respect to the maximum conductance of the calcium channels, G_{Ca} .

AP model in [26] and the variation of R for different \bar{G}_{Ca} values is obtained accordingly. In our previous analyses, we use the typical physiological value of $G_{Ca} = 0.09 mS/cm^2$ [26]. In this part, we fix the other model parameters as $N = 1000$, $L = 100 \mu m$, $r = 11 \mu m$, $R_m = 20 k\Omega cm^2$, and $\rho = 100 nM$ [26, 37, 40]. According to Fig. 2.9, T_{AP} increases and R decreases with an increase in \bar{G}_{Ca} . We find $T_{AP} = 259 msec$ and $R = 3.86 bit/sec$ for $\bar{G}_{Ca} = 0.05 mS/cm^2$ and $T_{AP} = 598 msec$ and $R = 1.67 bit/sec$ for $\bar{G}_{Ca} = 0.15 mS/cm^2$. The analysis presented in [41] also shows that the reduced permeability of the calcium channels results in shorter AP durations which confirms our results. Moreover, since $C_{gj} = 1 bit$ is found for $N = 1000$, the transmission rate of TC is the same as the reception rate of RC. Although increasing R is a desired objective in the classical communication, for the GJ communication, an increase in R due to the reduced \bar{G}_{Ca} may cause several arrhythmias which are discussed in the next section.

2.5 Gap Junction Communication Channel Parameters and Cardiac Diseases

The GJ communication between cardiomyocytes enables the electrical signal conduction, i.e., the AP propagation, in the heart. Synchronous propagation of the APs leads the heart to contract and relax as a single unit. Therefore, the GJ communication channel failures and deficiencies cause several disorders in the synchronous propagation of the APs and hence arrhythmias in the heart. Since the fundamental three-cell network model used in this chapter constitutes the large communication network of cardiomyocytes in the heart, the properties of the three-cell network reflect the properties of the large network. Thus, the information about the large network of cardiomyocytes can be inferred from the results presented above. In this section, we investigate the relations between cardiac diseases and the GJ communication parameters which are the channel capacity, the propagation delay and the information transmission rate.

2.5.1 Channel Capacity and Cardiac Diseases

In this part, the relation between cardiac diseases and the channel capacity of the GJ communication is investigated. In the previous section, the effects of several parameters on the channel capacity are shown. We present the relation between these parameters and cardiac diseases using the results of several medical researches. For each parameter, the relation between the channel capacity and cardiac diseases is observed.

2.5.1.1 Number of Gap Junction Channels

The numerical analysis performed in the previous section shows that a decrease in the GJ coupling due to a reduction in the total number of the GJ channels clustered in a GJ causes capacity of the channel to decrease. According to results of investigations of heart diseases, a reduced GJ coupling leads to several heart diseases such as sudden death due to spontaneous ventricular arrhythmia [42] or an increase in incidence of ventricular tachycardias [43]. We can conclude that the reduction in the channel capacity due to the reduced GJ coupling is related with the increased incidence of the cardiac diseases.

2.5.1.2 Length of Cardiomyocyte

In the GJ communication, the channel capacity decreases with an increase in the length of the cardiomyocyte, L , as shown in Fig. 2.7(b). The study presented in [44] investigates effects of the structural properties of cardiomyocytes on ischemic cardiomyopathy (ICM) and the results show that the length of cardiomyocytes is significantly longer in patients with ICM. We can say that a reduction in the capacity of the GJ channel causes more erroneous transmission of the information; as a result, the coordination between cardiomyocytes decreases and the cardiac tissue becomes diseased. It can be concluded that the decrease in the GJ communication channel capacity due to an increase in L , and an increase in the occurrence of ICM due to longer cardiomyocytes is correlated.

2.5.1.3 Radius of Cardiomyocyte

The channel capacity of the GJ communication decreases with an increase in the radius of cardiomyocytes as illustrated in Fig. 2.7(c). The results of the study presented in [45] reveal that the radius of cardiomyocytes is significantly longer in hypertensive patients compared to normal subjects. In this case, an increase in the radius of cardiomyocytes causes both a decrease in the channel capacity and an increase in the occurrence of hypertensive disease. Therefore, the decrease in the channel capacity due to the increase in the cell radius is correlated with the increase in the incidence of the hypertension.

2.5.1.4 Membrane Resistivity

The numerical analysis shows that a reduction in the membrane resistivity decreases the channel capacity of the GJ communication as seen in Fig. 2.7(d). According to an analysis presented in [46], a decrease in the cardiomyocyte membrane resistivity is related to the impairment of the impulse propagation and it can cause severe cardiac arrhythmias. This relation also confirms our result; that is, according to (2.3), a decrease in R_m increases the critical conductance value and a high critical conductance value can lead to an AP propagation impairment. Consequently, the reduction in the channel capacity due to the

reduced membrane resistivity is accompanied with the cardiac arrhythmia.

2.5.1.5 Free Calcium Concentration

From the numerical analysis, we observe that the GJ communication channel capacity decreases with an increase in the free Ca^{2+} concentration inside the cytoplasm of the cardiomyocytes as seen in Fig. 2.7(e). The free Ca^{2+} concentration overload causes several triggered arrhythmias such as Delayed-Afterdepolarizations (DADs) and Early-Afterdepolarizations (EADs) [47]. Furthermore, these triggered arrhythmias are major initiators of ventricular tachycardia which is an immediate precursor of ventricular fibrillation and a major cause of sudden death by heart failure [47]. We can conclude that the GJ communication channel capacity reduction due to the increased free Ca^{2+} concentration inside the cytoplasm is correlated with the increased occurrence of the ventricular tachycardia.

2.5.2 Channel Propagation Delay and Cardiac Diseases

According to the results of the AP propagation delay analysis, an increase in the number of the GJ channels decreases the propagation delay as shown in Fig. 2.8. However, a decrease in N causes the propagation delay to increase and it is accompanied with a decrease in the channel capacity. That is, a decrease in the number of the GJ channels increases the propagation delay and decreases the channel capacity. As stated above, the reduction of the GJ coupling due to the decrease in the number of GJ channel N causes several cardiac diseases. Therefore, it can be concluded that the AP propagation delay between cardiomyocytes is higher for the cases of the spontaneous ventricular arrhythmia [42] and the ventricular tachycardia [43].

2.5.3 Information Transmission Rate and Cardiac Diseases

The results of the numerical analysis show that a decrease in the maximum calcium channel conductance \bar{G}_{Ca} increases the information transmission rate between TC and RC. Although in classical communication, increasing R is a desired objective, the physiological

properties of cardiomyocytes cannot support very high transmission rates. In other words, at higher transmission rates, each received AP pulse also leads the receiver cardiomyocyte to contract and relax at higher rates due to the excitation-contraction coupling property of cardiomyocytes. Therefore, since heart cannot support very high beating rates, an increase in R causes several arrhythmias. In [48], heart rates >100 beats/min are referred to as tachycardia causing the heart to be arrhythmic. Furthermore, prolongation of the AP duration, T_{AP} , is a reason of the development of EADs causing a number of arrhythmias in the heart including long-QT syndrome and heart failure [36, 49]. As a result, we can say that both very low and very high rate R increase the occurrence of the cardiac diseases stated above.

2.5.4 Application on Nanomedicine

Nanomedicine is the application of the molecular nanotechnology on the medicine and the availability of such technologies brings dramatic progress in the medical services [5]. Investigation, prediction, diagnosis and treatment of diseases are some areas that are covered by nanomedicine. To be able to perform these applications, the nanomedicine proposes the use of nanodevices, e.g., nanosensors, nanovehicles, and nanoactuators [5, 50].

Based on the observations stated above, the most important deductions are those in diseased myocardium, the channel capacity of the GJ communication is lower and the propagation delay is higher than for the case of healthy myocardium. Furthermore, the causes of very high or very low information transmission rates contribute to the occurrence of cardiac diseases. As a result, the information theoretical analysis of the GJ communication may provide valuable insights into causes of the cardiac diseases. The channel capacity, the channel propagation delay, and the transmission rate can be used as metrics for investigation, prediction, diagnosis and treatment of several cardiac diseases in nanomedicine. These parameters can be measured and monitored by using multiple intra-body nanodevices and nanosensors communicating with cardiomyocytes via GJ channels. For instance, in [51], the use of nanoparticles for molecular imaging, advanced therapeutics, and drug delivery systems in treatment of cardiovascular diseases is discussed. In addition, the information

theoretical analysis of the GJ communication can be used for simulation tools of drug tests to confirm reliability of drugs. Hence, diagnosis and treatment techniques of cardiac diseases using the information theoretical model of the GJ communication stands as a promising application of the emerging nanomedicine.

Chapter 3

RECEIVER DESIGN FOR MOLECULAR COMMUNICATION

In the Molecular Communication (MC), molecules are utilized to encode, transmit, and receive information. Transmission of the information is achieved by means of diffusion of molecules and the information is recovered based on the molecule concentration variations at the receiver location. The MC is very prone to intersymbol interference (ISI) due to residual molecules emitted previously. Furthermore, the stochastic nature of the molecule movements adds noise to the MC. For the first time, we propose four methods for a receiver in the MC to recover the transmitted information distorted by both ISI and noise. We introduce sequence detection methods based on maximum a posteriori (MAP) and maximum likelihood (ML) criterions, both a linear equalizer and a nonlinear decision-feedback equalizer based on minimum mean-square error (MMSE) criterion. We present a channel estimator to estimate time varying MC channel at the receiver. The performances of the proposed methods based on bit error rates are evaluated. The sequence detection methods reveal the best performance at the expense of computational complexity. However, the MMSE equalizer has the lowest performance with the lowest computational complexity. The results show that using these methods significantly increases the information transmission rate in the MC.

3.1 Introduction

Molecular communication (MC) is a promising paradigm for communication at nanoscale [1, 4] and it is inspired by the communication of the biological systems at cellular level [6]. The construction of nanonetworks by interconnecting nanodevices via MC channels expands the capabilities of single nanodevices by means of cooperation between them [2, 3]. In the MC, molecules are utilized to encode, transmit, and receive information. It is believed

that the integration process of the molecular transceivers in nanodevices is more feasible due to their size and natural domain unlike the classical communication techniques [8]. In the MC, the information transmission relies on the diffusion process, i.e., the propagation of molecules by means of the laws of free diffusion in an aqueous medium, enabling the transmission of the information. Several nature-inspired and theoretically modeled MC techniques exist in the literature. For example, in [6], based on the diffusion of pheromones, spores, and pollen, a long range interconnection of nanodevices deployed over distances from a few centimeters to several meters is discussed. On the other hand, short range MC channel between cardiomyocytes is constructed by gap junction channels [17]. In [2], flagellated bacteria and catalytic nanomotors are two proposed communication techniques for the transport of DNA encoded information between emitters and receivers by means of a physical carrier. Morphogenesis is also proposed as a method for communication of nanodevices [10].

The research on the information theoretical investigation of the MC has been heavily conducted in the literature [11], [52], [16], [53]. However, to the date, there is little effort addressing the design of a receiver nanodevice which detects the transmitted information from the received concentration signal. Although in [7], [15], the diffusion-based MC channel is analyzed from an information theoretical perspective, noise sources are not incorporated to the analysis. For the first time, the noise sources in the MC are analyzed in [8].

For the MC, the information is encoded in the concentration of the emitted molecules with on-off keying (OOK) modulation in [7], [15], [14]. As described in [11], an emitted concentration pulse changes the molecule concentration at the receiver location. Because of the diffusion of the emitted molecules from regions of high concentration to those of low concentration, the molecule concentration at the receiver location decreases if the molecule emission ceases. However, the emitted molecules do not vanish completely in the reception space. That is, if a new concentration pulse is emitted before the molecule concentration at the receiver location becomes negligibly low, the receiver senses the effects of both the previously emitted concentration pulses and the currently transmitted pulse. Therefore, a low signaling interval, i.e., a high transmission rate, causes intersymbol interference (ISI)

in the MC. If the transmitter waits long enough to send a new concentration pulse, the effect of the ISI can be eliminated; then, the information transmission rate becomes very low. Nevertheless, having high transmission rates is desirable to improve communication capabilities of nanodevices.

For the first time in the literature, in order to recover the transmitted information distorted by both the ISI and the noise at high transmission rates in the MC, we propose the following solutions. Firstly, the sequence detection methods based on maximum a posteriori (MAP) and maximum likelihood (ML) criteria are presented. Secondly, we present a linear equalizer based on minimum mean-square error (MMSE) criterion. Finally, a nonlinear MMSE decision-feedback equalizer (MMSE-DFE) is proposed. These methods are well covered for the classical communication systems [54, 55]. However, most of these techniques are developed for the communication channels having additive white Gaussian noise (AWGN) at the output of the channel. Since in the MC, the noise that is added to the received signal is signal-dependent which makes the noise nonstationary [8], the existing techniques in the classical communication cannot be applied directly to the MC. In this chapter, we modify the detection methods stated above to properly implement for a receiver in the MC. The proposed methods significantly decrease the bit error probabilities and hence increase the communication capabilities of nanodevices communicating via MC. The study presented in this chapter is given in [56]. Since the magnetic recording channels have also signal-dependent noise at the output of the channel [57, 58], the signal detection methods used for magnetic recording channels are useful in the design of a receiver for the MC.

The rest of this chapter is organized as follows. Section 3.2 describes the model of the MC. In Section 3.3, the sequence detection methods based on MAP and ML criteria are presented. A linear equalizer which satisfies the MMSE criterion is described in Section 3.4. A nonlinear type of equalizer which is a decision-feedback equalizer is presented in Section 3.5. In Section 3.6, to estimate the time varying channel, a channel estimator is presented. The performance of these methods based on bit error rates are evaluated in Section 3.7.

3.2 Molecular Communication Model

The MC model that is considered in this chapter consists of a Transmitter Nanodevice (TN), molecular diffusion channel, signal-dependent additive noise at the output of the channel, and a Receiver Nanodevice (RN) as illustrated in Fig. 3.1. TN encodes the binary information bits, $\{a_j\}$, into the molecule concentration pulses. The concentration pulse, denoted by $s(t)$, is the time variation of the molecule concentration emitted by TN for the transmission of one information bit. The transmitted concentration signal propagates until it reaches the receiver location. The propagation relies on the particle diffusion process in the aqueous medium. At the reception space, the molecule concentration, denoted by $y(t)$, changes according to both the time and the distance between TN and RN. Furthermore, a signal-dependent concentration noise, $n(t)$, is added to the molecule concentration signal in the reception space. RN samples the noisy molecule concentration, denoted by $z(t)$, in the reception space, and decides the transmitted information sequence based on these samples. In the model, we consider following assumptions:

- The communication takes place in a 3D *aqueous* environment having infinite extent which is indexed through the Cartesian axes x , y , and z .
- The size of the TN is considered negligible with respect to the distance between the TN and the RN. Therefore, the TN is approximated as a *point source* emitting desired molecule concentration signals at the location $(x = 0, y = 0, z = 0)$.
- The emitted molecules by TN propagates from the TN location $(x = 0, y = 0, z = 0)$ to the RN location $(x = x_R, y = y_R, z = z_R)$ only by means of the laws of *free diffusion* in an aqueous medium. That is, the emitted molecules are subject to the Brownian motion.
- The particle concentration measurement takes place inside the reception space having a *spherical shape* with radius ρ . The received molecule concentration, $z(t)$, is assumed *homogeneous* inside the reception space.

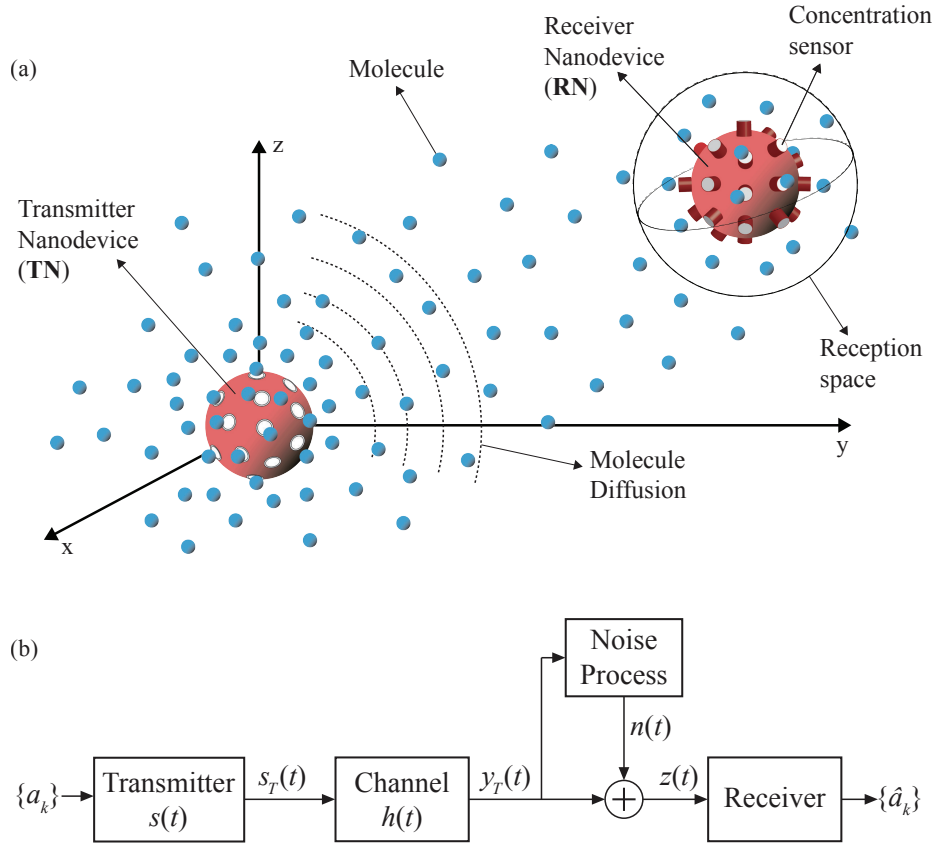


Figure 3.1: The diffusion-based MC model between TN and RN. (a) Graphical representation. (b) Block diagram representation.

- The communication between TN and RN is considered as the binary digital communication with OOK modulation with equally likely transmitted binary information bits.

Firstly, we derive the impulse response of the molecular diffusion channel, i.e., $h(t)$. According to Fick's second law of diffusion [7], the concentration of the molecules, denoted by $c(x, y, z, t)$, at location (x, y, z) and at time t is described by the following equation

$$\frac{1}{D} \frac{\partial c(x, y, z, t)}{\partial t} = \nabla^2 c(x, y, z, t) \quad (3.1)$$

where D is the diffusion coefficient of the medium and $\nabla^2 c(x, y, z, t)$ is the sum of the 3D spatial second derivatives of $c(x, y, z, t)$. The impulse response of the molecular diffusion

channel is found by solving (3.1) with initial condition

$$c(x, y, z, t = 0) = \delta(x, y, z) \quad (3.2)$$

where the molecules are emitted by TN which is a point source located at $(x = 0, y = 0, z = 0)$. The response of (3.1) to the impulse given in (3.2) is

$$c(x, y, z, t) = \frac{m}{(4\pi tD)^{3/2}} \exp\left[-\frac{(x)^2 + (y)^2 + (z)^2}{4tD}\right]. \quad (3.3)$$

where m is the total number of the emitted molecules. Therefore, in a 3D medium, if RN is located at (x_R, y_R, z_R) , the impulse response of the diffusion channel $h(t)$ is given by

$$h(t) = \frac{m}{(4\pi tD)^{3/2}} \exp\left[-\frac{|r|^2}{4tD}\right] \quad (3.4)$$

where $|r|$ is the Euclidean distance between RN and TN, i.e., $|r| = \sqrt{(x_R)^2 + (y_R)^2 + (z_R)^2}$. To have a compact notation, we drop (x, y, z) term in $h(x, y, z, t)$ because TN and RN are located at fixed positions. Since the diffusion coefficient D depends on several factors such as the temperature and viscosity of the fluid which are time varying properties, the diffusion-based molecular channel is also time varying.

We consider the transmitter concentration pulse as a rectangular pulse given as

$$s(t) = A \text{rect}\left(\frac{t - T_e/2}{T_e}\right) \quad (3.5)$$

where A is the amplitude of the molecule concentration emitted by TN and T_e is the duration of the molecule emission. Therefore, the response of the channel to the input signal $s(t)$ is denoted by $y(t)$ and can be obtained using the convolution operation as $y(t) = s(t) * h(t)$. The physical meaning of $y(t)$ is the noiseless molecule concentration variation in the reception space caused by one emitted pulse. The variation of $y(t)$ with respect to time is shown in Fig. 3.2. Assuming the communication starts at time $t = 0$, the total emitted molecule concentration into the aqueous environment, denoted by $s_T(t)$, for the transmitted information sequence $\{a_j\}$ is given as

$$s_T(t) = \sum_{j=0}^{\infty} a_j s(t - jT) \quad (3.6)$$

where T is the duration of the signaling interval. Since the response of the channel to the pulse $s(t)$ is given by $y(t)$, the total noiseless received concentration by RN is

$$y_T(t) = \sum_{j=0}^{\infty} a_j y(t - jT) \quad (3.7)$$

The emission of a new pulse before the previously emitted molecules vanish in the reception space causes ISI because $y(t)$ is a infinite duration signal and do not disappear completely in the reception space in a short time as illustrated in Fig. 3.2. That is, the currently emitted pulse is distorted due to the previous transmissions which can be seen in (3.7). Since $y(t)$ decreases after reaching its maximum value at $t = t_{max}$, the signaling interval T should satisfy the condition $T \gg t_{max}$ in order to have negligible ISI. However, an increase in the signaling interval decreases the transmission rate given as $R = 1/T$ and a low information transmission rate is undesirable. It is aimed to have high transmission rates to improve the communication capabilities of nanodevices using the MC. As a result, to deal with the distortion caused by the ISI at higher transmission rates, we introduce several methods for RN which are discussed in the subsequent sections.

At the output of the channel, an additive signal-dependent noise is added to the ISI distorted signal $y_T(t)$. Then, the total molecule concentration variation in the reception space caused by the transmitted information sequence $\{a_j\}$ is given by

$$z(t) = \sum_{j=0}^{\infty} a_j y(t - jT) + n(t) \quad (3.8)$$

where $n(t)$ is the particle counting noise generated by a random process [8]. To describe the noise introduced in [8], firstly, we need to define the noiseless and noisy number of molecules inside the reception space, denoted by $N_p(t)$ and $\hat{N}_p(t)$, respectively, given as

$$N_p(t) = V_R y_T(t); \quad \hat{N}_p(t) = V_R z(t) \quad (3.9)$$

where $V_R = (4/3)\pi\rho^3$ is the volume of the spherical reception space. As given in [8], $\hat{N}_p(t)$ is distributed with Poisson probability distribution function (pdf) whose parameter is $N_p(t)$ at observation time t . Therefore, both the expectation and variance of the number of molecules in the reception space is $N_p(t)$. Furthermore, in a reliable MC between TN and RN, we can

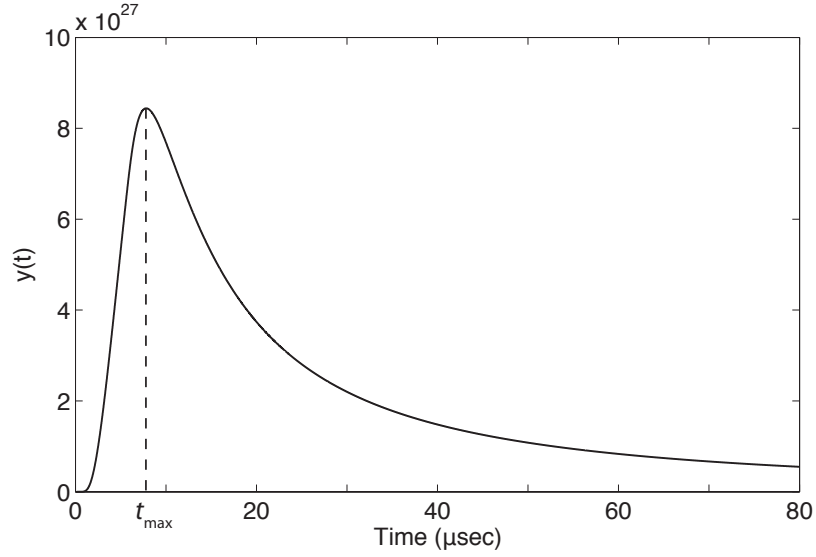


Figure 3.2: The noiseless molecule concentration variation at RN, $y(t)$, for $D = 2.2 \times 10^{-9} \text{m}^2/\text{s}$, $r = 250 \text{nm}$, $m = 10^5$, $A = 4 \times 10^9$, $T_e = 4.7 \mu\text{s}$.

assume that $N_p(t) \gg 100$ condition is satisfied at any instant. Thus, the Gaussian approximation of the Poisson distribution for $\hat{N}_p(t)$ can be used, i.e., $\hat{N}_p(t) \sim \mathcal{N}(N_p(t), N_p(t))$. By using (3.9) and the pdf of $\hat{N}_p(t)$, the received noisy molecule concentration in the reception space, $z(t)$, is distributed as $z(t) \sim \mathcal{N}(y_T(t), y_T(t)/V_R)$. Finally, the probability distribution of the noise, $n(t)$, is given as $n(t) \sim \mathcal{N}(0, y_T(t)/V_R)$. Thus, the variance of the additive Gaussian noise $n(t)$ depends on both $y(t)$ and the transmitted information sequence $\{a_j\}$ which makes the noise nonstationary. Furthermore, based on the independency of the Brownian movement of different molecules in the aqueous medium, the noise samples are assumed independent of each other at different observation times [8].

We assume that RN is able to sample the molecule concentration inside the reception space at a rate R , and the TN and RN are synchronized, i.e., both transmission and reception start at the same time $t = 0$. Therefore, the received signal samples by the RN is given as

$$z_k = \sum_{j=0}^{\infty} a_j y_{k-j} + n_k, \quad k = 0, 1, \dots \quad (3.10)$$

where $z_k = z(kT)$, $y_{k-j} = y((k-j)T)$, and $n_k = n(kT)$. However, the channel response is causal, i.e., $y_k = 0$ if $k < 0$. Furthermore, in a practical system, it is acceptable to assume that the length of the ISI is finite and given by $I + 1$; that is, $y_k = 0$ for $k > I$. Thus, z_k depends on the currently transmitted bit a_k and I previously transmitted bits a_{k-1}, \dots, a_{k-I} . Then,

$$z_k = \sum_{j=k-I}^k a_j y_{k-j} + n_k = \sum_{j=0}^I y_j a_{k-j} + n_k, \quad k = 0, 1, \dots \quad (3.11)$$

Using (3.11), the discrete-time equivalent model of the diffusion-based MC channel is shown in Fig. 3.3. The pdf of z_k is

$$z_k \sim \mathcal{N}(\mu_k, \sigma_k^2) \quad (3.12)$$

where the mean and variance, respectively, are

$$\mu_k = \sum_{j=0}^I y_j a_{k-j}; \quad \sigma_k^2 = \frac{1}{V_R} \sum_{j=0}^I y_j a_{k-j} \quad (3.13)$$

and the pdf of the noise samples is given as

$$n_k \sim \mathcal{N}(0, \sigma_k^2) \quad (3.14)$$

After describing the propagation and noise models of the diffusion-based MC, we present several methods for RN to recover the transmitted information bits that are distorted by both the ISI and noise.

3.3 Sequence Detection

In the presence of the ISI, the sequence detection is equivalent to the problem of estimating the state of a finite-state machine (FSM) [54]. For ISI with length $I + 1$, the state of the FSM at any instant depends on the I most recent inputs. Since we consider binary communication, the channel has 2^I states. Therefore, the channel can be described by a 2^I -state trellis and the transmitted information sequence corresponds to a path through the trellis. In Fig. 3.4, a trellis is illustrated for $I = 2$. Each branch represents a state transition having a weight called the branch metric. The sum of the weights of each branch in a path

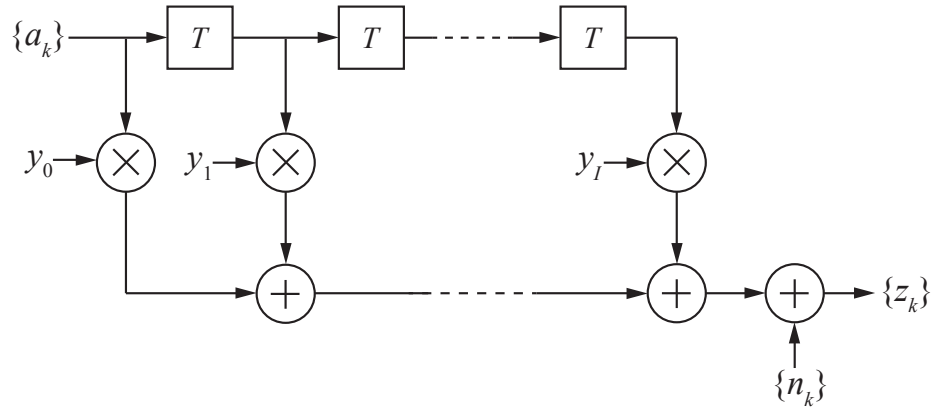


Figure 3.3: Discrete-time equivalent model of the molecular diffusion channel with inter-symbol interference.

is called the path metric. A sequence detector selects a path (sequence) corresponding to the received signal sequence $\{z_k\}$ based on the path metric of the each possible path, which is discussed later in this section. We consider two criteria to obtain the branch metrics: the maximum a posteriori (MAP) and maximum likelihood (ML) where the former selects the sequence maximizing the a posteriori probability density function and the latter selects the sequence maximizing the likelihood function in the trellis search. Furthermore, RN can reduce the complexity of the sequence detector and the number of sequences in the trellis search by using the Viterbi algorithm to discard the unlikely sequences when the new samples are received by the RN [59].

3.3.1 MAP Sequence Detection

The MAP sequence detector determines the transmitted sequence of information bits $\{a_j\}$ by maximizing the joint pdf of the transmitted bits and the received samples [57]. That is,

$$\hat{\mathbf{a}}_0^N = \arg \max_{\mathbf{a}_0^N} f(\mathbf{z}_0^N, \mathbf{a}_0^N) \quad (3.15)$$

where $N + 1$ is the length of the transmitted sequence of bits, $\hat{\mathbf{a}}_0^N$ denotes the detected sequence for the transmitted information sequence \mathbf{a}_0^N , the pdf $f(\mathbf{z}_0^N, \mathbf{a}_0^N)$ is the joint pdf

of the received concentration signal samples $\underline{\mathbf{z}}_0^N$ and the transmitted bits $\underline{\mathbf{a}}_0^N$. The bold and underlined symbols indicate the sequence of those symbols whose starting and ending elements are indicated in the subscript and superscript indexes, respectively. By Bayes rule, the joint pdf can be factored as follows

$$\begin{aligned} f(\underline{\mathbf{z}}_0^N, \underline{\mathbf{a}}_0^N) &= P(\underline{\mathbf{a}}_0^N) f(\underline{\mathbf{z}}_0^N | \underline{\mathbf{a}}_0^N) \\ &= \prod_{k=0}^N P(a_k | \underline{\mathbf{a}}_{k+1}^N) \prod_{k=0}^N f(z_k | \underline{\mathbf{z}}_{k+1}^N, \underline{\mathbf{a}}_0^N) \end{aligned} \quad (3.16)$$

where $P(\underline{\mathbf{a}}_0^N)$ and $P(a_k | \underline{\mathbf{a}}_{k+1}^N)$ are the joint and conditional probability mass functions of the transmitted binary information bits, respectively, $f(\underline{\mathbf{z}}_0^N | \underline{\mathbf{a}}_0^N)$ and $f(z_k | \underline{\mathbf{z}}_{k+1}^N, \underline{\mathbf{a}}_0^N)$ are the conditional pdf's. Since a_k 's are assumed as independent,

$$P(a_k | \underline{\mathbf{a}}_{k+1}^N) = P(a_k) \quad (3.17)$$

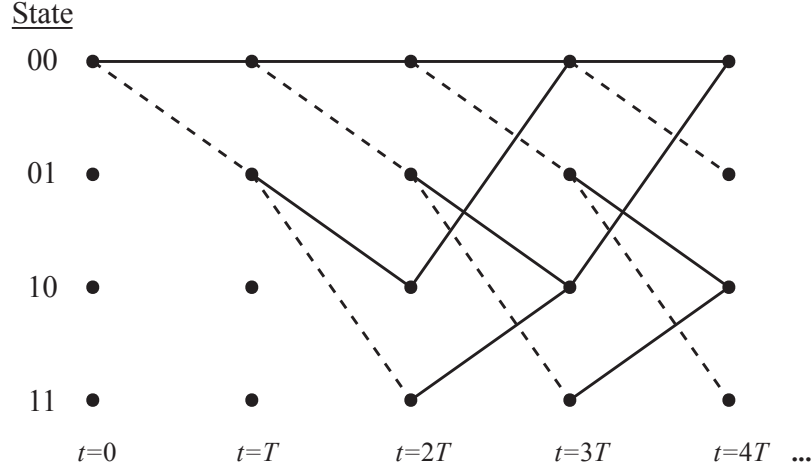
The noise samples are also independent and the channel has a finite ISI length; thus, we can exploit these properties of the MC to simplify (3.16). The conditional pdf of each observation can be further simplified as follows

$$f(z_k | \underline{\mathbf{z}}_{k+1}^N, \underline{\mathbf{a}}_0^N) = f(z_k | \underline{\mathbf{a}}_{k-I}^k) \quad (3.18)$$

The conditional pdf of z_k depends only on $\underline{\mathbf{a}}_{k-I}^k$ which also can be seen in (3.11).

Maximizing the joint pdf given in (3.16) is equivalent to minimizing its negative logarithm. Therefore, the MAP detector is given as

$$\begin{aligned} \hat{\underline{\mathbf{a}}}_0^N &= - \arg \min_{\underline{\mathbf{a}}_0^N} \ln \left[\prod_{k=0}^N P(a_k) \prod_{k=0}^N f(z_k | \underline{\mathbf{a}}_{k-I}^k) \right] \\ &= - \arg \min_{\underline{\mathbf{a}}_0^N} \left[\sum_{k=0}^N \ln P(a_k) + \sum_{k=0}^N \ln f(z_k | \underline{\mathbf{a}}_{k-I}^k) \right] \\ &= - \arg \min_{\underline{\mathbf{a}}_0^N} \sum_{k=0}^N \left[\ln P(a_k) + \ln f(z_k | \underline{\mathbf{a}}_{k-I}^k) \right] \\ &= \arg \min_{\underline{\mathbf{a}}_0^N} \sum_{k=0}^N \mathcal{M}^{\text{MAP}}(z_k, \underline{\mathbf{a}}_{k-I}^k) \end{aligned} \quad (3.19)$$

Figure 3.4: A trellis diagram for $I = 2$ with 2^I states.

where $\mathcal{M}^{\text{MAP}}(z_k, \underline{\mathbf{a}}_{k-I}^k)$ is the branch metric of trellis search in the Viterbi algorithm for the MAP criterion and given by

$$\mathcal{M}^{\text{MAP}}(z_k, \underline{\mathbf{a}}_{k-I}^k) = -\ln P(a_k) - \ln f(z_k | \underline{\mathbf{a}}_{k-I}^k) \quad (3.20)$$

By using the pdf of the noise samples, the conditional pdf of the concentration samples is given as

$$f(z_k | \underline{\mathbf{a}}_{k-I}^k) = \frac{1}{\sqrt{2\pi\sigma_k^2}} \exp \left[-\frac{(z_k - \mu_k)^2}{2\sigma_k^2} \right] \quad (3.21)$$

where μ_k and σ_k^2 are given in (3.13). After substituting the pdf given in (3.21) into the expression for the branch metric (3.20), and eliminating constant terms that are common, the MAP branch metric becomes

$$\mathcal{M}^{\text{MAP}}(z_k, \underline{\mathbf{a}}_{k-I}^k) = \ln \sigma_k^2 + \frac{(z_k - \mu_k)^2}{\sigma_k^2} - 2 \ln P(a_k) \quad (3.22)$$

3.3.2 ML Sequence Detection

The ML sequence detection method determines the transmitted sequence of information bits $\{a_j\}$ by maximizing the likelihood function [54], i.e.,

$$\hat{\underline{\mathbf{a}}}_0^N = \arg \max_{\underline{\mathbf{a}}_0^N} f(\underline{\mathbf{z}}_0^N | \underline{\mathbf{a}}_0^N) \quad (3.23)$$

where the likelihood function $f(\mathbf{z}_0^N | \mathbf{a}_0^N)$ is the joint pdf of the received concentration signal samples \mathbf{z}_0^N conditioned on the transmitted bits \mathbf{a}_0^N . Furthermore, if the transmitted binary information bits are equally probable, i.e., $P(a_k) = \frac{1}{2}$, the MAP sequence detection is identical to the ML sequence detection. The ML sequence detector is the optimum detector minimizing the error probability of a sequence [54]. With arguments similar to those for MAP sequence detection, the ML sequence detection can be simplified as follows

$$\hat{\mathbf{a}}_0^N = \arg \min_{\mathbf{a}_0^N} \sum_{k=0}^N \mathcal{M}^{\text{ML}}(z_k, \mathbf{a}_{k-I}^k) \quad (3.24)$$

where $\mathcal{M}^{\text{ML}}(z_k, \mathbf{a}_{k-I}^k)$ is the branch metric of the trellis search for the ML criterion. By using (3.22) and eliminating the constant terms, the ML branch metric is

$$\mathcal{M}^{\text{ML}}(z_k, \mathbf{a}_{k-I}^k) = \ln \sigma_k^2 + \frac{(z_k - \mu_k)^2}{\sigma_k^2} \quad (3.25)$$

A similar result is found in [58] for the magnetic recording channels which have also signal dependent noise. After deriving the branch metrics, the Viterbi algorithm can be easily implemented to reduce the computational complexity of the MAP and ML sequence detection methods.

3.4 Minimum Mean-Square Error Equalizer

The MAP sequence detection in the presence of a priori symbol probabilities and the ML detection in the presence of equally probable symbols minimize the probability of a sequence error [54]. However, the complexities of the MAP and ML detectors grow exponentially with an increase in the length of the ISI even if the Viterbi algorithm is implemented. At nanoscale, the implementation of a complex circuitry is not practical. In this section, to mitigate the ISI, we present a linear equalizer based on the minimum mean-square error (MMSE) criterion called MMSE equalizer. The MMSE equalizer is a suboptimum linear equalizer with significantly less complexity compared to the MAP and ML sequence detectors [54].

In the MMSE equalization, the equalizer is designed to minimize the mean-square error (MSE), i.e., $\varepsilon_k = a_{k-d} - \tilde{a}_k$ where a_{k-d} is the transmitted bit in the $(k-d)$ th signaling

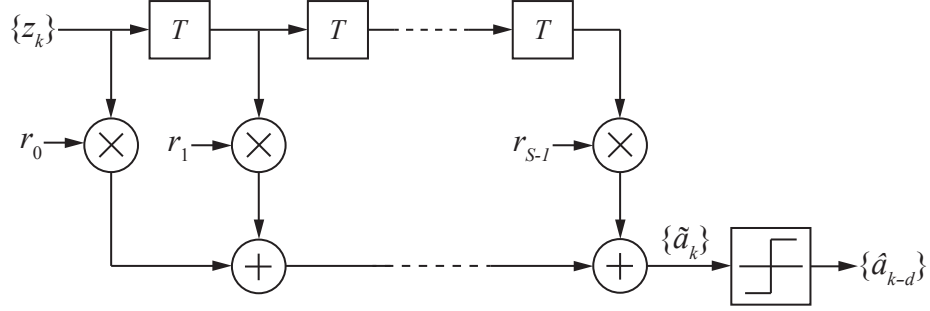


Figure 3.5: The block diagram of MMSE equalizer with S tap coefficients.

interval, \tilde{a}_k is the estimate of that bit at the output of the equalizer and d is the equalizer delay. The equalizer delay is found as follows. Let y_{d_1} be the greatest magnitude component of $\{y_k\}$. Also, let the number of MMSE equalizer taps be equal to $S = 2d_2 + 1$ where d_2 is an integer. Then, we choose the equalizer delay as $d = d_1 + d_2$ [60]. Since the MMSE equalizer is linear, its output as a linear combination of input samples is given by

$$\tilde{a}_k = \sum_{q=0}^{S-1} r_q z_{k-q} \quad (3.26)$$

where r_0 through r_{S-1} are tap weight coefficients of the MMSE equalizer as illustrated in Fig. 3.5. The output \tilde{a}_k is quantized to the nearest information bit in Euclidian distance to decide \hat{a}_k by using a simple quantizer. We assume that the number of taps of the MMSE equalizer is the same as the ISI length, i.e., $S = I + 1$.

To minimize the MSE which is defined as $J = E|\varepsilon_k|^2$, we can obtain a set of linear equations by using the orthogonality principle in the mean-square estimation [54]. That is, the coefficients $\{r_p\}$ are selected to make the error ε_k orthogonal to the signal samples $\{z_{k-p}\}$, i.e., $E[\varepsilon_k z_{k-p}] = 0$ for $0 \leq p \leq S-1$. Then, by using (3.11) and (3.26), the following set of equations are found

$$E \left[\left(a_{k-d} - \sum_{q=0}^{S-1} r_q z_{k-q} \right) z_{k-p} \right] = 0, \quad p = 0, 1, \dots, S-1 \quad (3.27)$$

or, equivalently,

$$\sum_{q=0}^{S-1} r_q \mathbb{E}[z_{k-q} z_{k-p}] = \mathbb{E}[a_{k-d} z_{k-p}], \quad p = 0, 1, \dots, S-1 \quad (3.28)$$

We use $\Gamma_{pq} = \mathbb{E}[z_{k-q} z_{k-p}]$ and $\xi_p = \mathbb{E}[a_{k-d} z_{k-p}]$ for a compact notation. After taking the expectations, we get

$$\begin{aligned} \Gamma_{pq} &= \sum_{m=0}^I y_m y_{m+p-q} + \sigma_{k-p}^2 \delta_{pq}, \quad p, q = 0, \dots, S-1 \\ \xi_p &= y_{d-p}, \quad p = 0, 1, \dots, S-1 \end{aligned} \quad (3.29)$$

where δ_{pq} is the Kronecker delta function, σ_{k-p}^2 is the variance of the concentration sample z_{k-p} , and y_{d-p} is the $(d-p)$ th coefficient of the equivalent discrete time channel. Thus, (3.28) can be written as

$$\sum_{q=0}^{S-1} \Gamma_{pq} r_q = \xi_p, \quad p = 0, 1, \dots, S-1 \quad (3.30)$$

Unlike the additive stationary Gaussian noise, the variance of the noise is signal-dependent in the diffusion-based MC. As a result, for different transmitted information sequences, there is a different optimum solution for the MMSE equalizer tap weights. The detected bits \hat{a}_k through $\hat{a}_{k-S-I+1}$ are required to evaluate the variances σ_k^2 through σ_{k-S+1}^2 in (3.29), assuming the decisions are correct. Hence, the output of the decision device is used in the MMSE equalizer to solve (3.30) which makes the proposed MMSE equalizer signal sensitive. That is, the equalizer tap coefficients are adaptively updated based on the detected bits. Since using \hat{a}_k in the estimation of a_k is inconsistent, we set $\hat{a}_k = \frac{1}{2}$ in the estimation of a_k as an *ad hoc* method to prevent this inconsistency. $\hat{a}_k = \frac{1}{2}$ has equal Euclidian distances to both $\hat{a}_k = 0$ and $\hat{a}_k = 1$, that is, a_k can be 0 or 1 with equal probabilities, which is consistent with the equally likely transmitted bits. Also note that, the use of the wrong decisions causes error propagation which may deteriorate the performance of the MMSE equalizer

It is convenient to use matrix form to solve the set of equations given in (3.30) as follows

$$\mathbf{\Gamma} \underline{\mathbf{r}}_{\text{opt}} = \underline{\boldsymbol{\xi}} \quad (3.31)$$

where \mathbf{r}_{opt} is the column vector of S optimum equalizer tap weights $\{r_p\}$ given as $\mathbf{r}_{\text{opt}} = [r_0, r_1, \dots, r_{S-1}]^T$ and $\mathbf{\Gamma}$ denotes the Hermitian covariance matrix with elements Γ_{pq} given in (3.29), and $\underline{\boldsymbol{\xi}}$ is the column vector with elements ξ_p given in (3.29). Therefore, for k th received signal z_k , the optimum equalizer tap weights to estimate \tilde{a}_k are found as

$$\mathbf{r}_{\text{opt}} = \mathbf{\Gamma}^{-1} \underline{\boldsymbol{\xi}} \quad (3.32)$$

where $\mathbf{\Gamma}^{-1}$ is the inverse of the matrix $\mathbf{\Gamma}$. Due to the nonstationary characteristic of the noise, the optimum tap coefficients of the MMSE equalizer are updated at each sample using the previously detected bits. Thus, the MMSE equalizer needs to perform the operation given in (3.32) for each sample, which increases the complexity of the equalizer. However, the proposed method for the MMSE equalizer is not as complex as the sequence detection methods described in Section 3.3.

3.5 Minimum Mean-Square Error Decision-Feedback Equalizer

In this section, we consider an MMSE decision-feedback equalizer (MMSE-DFE) which is a nonlinear type of equalizer to mitigate the ISI. The MMSE-DFE is also suboptimum; however, its performance is generally better than that of suboptimum linear equalizers, e.g., the MMSE equalizer [54]. Furthermore, the MMSE-DFE still is not as complex as the optimum ML and MAP sequence detection methods. The MMSE-DFE consists of two sections that are a feedforward filter and a feedback filter as shown in Fig. 3.6. The decisions are made on the output of the equalizer and they are propagated through the feedback filter to eliminate the ISI. Since the input of the feedback filter is the output of a decision device, the MMSE-DFE has a nonlinear characteristics. The output of the MMSE-DFE is the estimate of the transmitted bit and it is given by

$$\tilde{a}_k = \sum_{q=0}^{L-1} f_q z_{k-q} + \sum_{q=1}^M b_q \hat{a}_{k-q-1} \quad (3.33)$$

where z_k is the noisy and ISI-distorted signal at the input of the MMSE-DFE and \hat{a}_k is the k th detected bit.

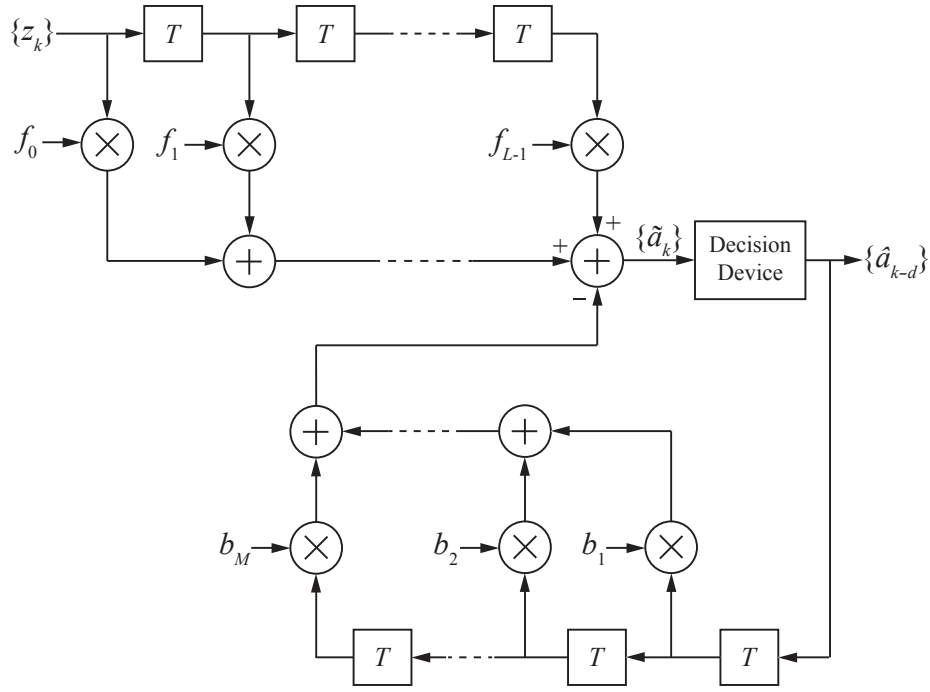


Figure 3.6: The block diagram of the MMSE-DFE.

The feedforward filter is based on the MMSE criterion and as analyzed in Section IV, its coefficients f_0 through f_{L-1} are given by the system of linear equations

$$\sum_{q=0}^{L-1} \Psi_{pq} f_q = \varphi_p, \quad p = 0, 1, \dots, L-1 \quad (3.34)$$

where Γ_{pq} and φ_p are defined as

$$\Psi_{pq} = \sum_{m=0}^I y_m y_{m+p-q} + \sigma_k^2 \delta_{pq}, \quad p, q = 0, \dots, L-1 \quad (3.35)$$

$$\varphi_p = y_{1-p}, \quad p = 0, 1, \dots, L-1$$

As stated in Section IV, the coefficients of the feedforward filter are found by using the matrix form representation of the system of the linear equations given in (3.34) as follows

$$\underline{\mathbf{f}}_{\text{opt}} = \underline{\Psi}^{-1} \underline{\varphi} \quad (3.36)$$

where $\underline{\mathbf{f}}_{\text{opt}}$ is the vector containing the optimum equalizer tap weights $\{f_q\}$, i.e., $\underline{\mathbf{f}}_{\text{opt}} = [f_0, f_1, \dots, f_{L-1}]^T$, $\underline{\Psi}^{-1}$ is the inverse of the Hermitian covariance matrix with elements

Ψ_{pq} given in (3.35), and $\underline{\varphi}$ is the column vector with elements φ_p given in (3.35). As in the case of the MMSE equalizer, the optimum coefficients for the feedforward filter of the MMSE-DFE are evaluated and updated at each sampling time.

The coefficients of the feedback filter of the MMSE-DFE detector are expressed in terms of the coefficients of the feedforward filter [54] as follows

$$b_k = - \sum_{q=0}^{L-1} f_q y_{k-q} = - \underline{\mathbf{f}}_{\text{opt}}^T \underline{\mathbf{y}}_k, \quad k = 1, 2, \dots, M \quad (3.37)$$

where $\underline{\mathbf{y}}_k$ is the L -dimensional column vector defined as $\underline{\mathbf{y}}_k = [y_k, y_{k-1}, \dots, y_{k-L+1}]^T$. The values of the coefficients of the feedback filter b_1 through b_M completely eliminate the ISI caused by the previously transmitted bits provided that the previous decisions are correct and that $M = L + I - 1$ [60]. We choose $L = I + 1$ and $M = 2I$. Thus, for the coefficients of the feedback filter given in (3.37), the output of the MMSE-DFE given in (3.33) reduces to

$$\begin{aligned} \tilde{a}_k &= f_0 y_1 a_{k-1} + \sum_{q=0}^I f_q n_{k-q} \\ &= \beta a_{k-1} + w_k \end{aligned} \quad (3.38)$$

where w_k is the correlated Gaussian noise term and $\beta = f_0 y_1$. The correlation length of the noise is the same as the ISI length $I + 1$ which can be seen from (3.38).

In Section 3.4, the output of the MMSE equalizer is quantized by a decision device to the nearest bit in Euclidian distance. However, for a decision device of the MMSE-DFE, we propose an alternative method to minimize the probability of the decision error. Motivated by the ML sequence detection, the decisions are made as follows

$$\begin{aligned} \hat{a}_{k-1} &= \arg \max_{a_{k-1}} f(\tilde{a}_k | \underline{\mathbf{a}}_{k-1}^k, \underline{\hat{\mathbf{a}}}_{k-I}^{k-2}, \underline{\tilde{\mathbf{a}}}_{k-I}^{k-1}) \\ &= - \arg \min_{a_{k-1}} \ln f(\tilde{a}_k | \underline{\mathbf{a}}_{k-1}^k, \underline{\hat{\mathbf{a}}}_{k-I}^{k-2}, \underline{\tilde{\mathbf{a}}}_{k-I}^{k-1}) \\ &= \arg \min_{a_{k-1}} \mathcal{H}(a_k, a_{k-1}) \end{aligned} \quad (3.39)$$

where $\mathcal{H}(a_k, a_{k-1})$ is the comparison metric given by

$$\mathcal{H}(a_k, a_{k-1}) = - \ln f(\tilde{a}_k | \underline{\mathbf{a}}_{k-1}^k, \underline{\hat{\mathbf{a}}}_{k-I}^{k-2}, \underline{\tilde{\mathbf{a}}}_{k-I}^{k-1}) \quad (3.40)$$

where $\mathcal{H}(0,0)$, $\mathcal{H}(0,1)$, $\mathcal{H}(1,0)$, and $\mathcal{H}(1,1)$ are the metric values of the possible combinations of a_k and a_{k-1} . In this case, the input samples of the decision device, i.e. \tilde{a}_k 's, are not independent due to the correlated noise term v_k . By Bayes rule, the pdf given in (3.39) can be written as

$$f(\tilde{a}_k | \underline{\mathbf{a}}_{k-1}^k, \hat{\underline{\mathbf{a}}}_{k-I}^{k-2}, \tilde{\underline{\mathbf{a}}}_{k-I}^{k-1}) = \frac{f(\tilde{\underline{\mathbf{a}}}_{k-I}^k | \underline{\mathbf{a}}_{k-1}^k, \hat{\underline{\mathbf{a}}}_{k-I}^{k-2})}{f(\tilde{\underline{\mathbf{a}}}_{k-I}^{k-1} | \underline{\mathbf{a}}_{k-1}^k, \hat{\underline{\mathbf{a}}}_{k-I}^{k-2})} \quad (3.41)$$

By using the pdf of the independent molecule concentration samples at the output of the channel, the expression given in (3.41) can be written as

$$\begin{aligned} & \frac{f(\tilde{\underline{\mathbf{a}}}_{k-I}^k | \underline{\mathbf{a}}_{k-1}^k, \hat{\underline{\mathbf{a}}}_{k-I}^{k-2})}{f(\tilde{\underline{\mathbf{a}}}_{k-I}^{k-1} | \underline{\mathbf{a}}_{k-1}^k, \hat{\underline{\mathbf{a}}}_{k-I}^{k-2})} \\ &= \sqrt{\frac{(2\pi)^I \det \mathbf{c}_k \exp[-\frac{1}{2} \mathbf{N}_k^T \mathbf{C}_k^{-1} \mathbf{N}_k]}{(2\pi)^{I+1} \det \mathbf{C}_k \exp[-\frac{1}{2} \mathbf{n}_k^T \mathbf{c}_k^{-1} \mathbf{n}_k]}} \end{aligned} \quad (3.42)$$

where \mathbf{C}_k is the $(I+1) \times (I+1)$ covariance matrix of the data samples $\tilde{\underline{\mathbf{a}}}_{k-I}^k$ given $\underline{\mathbf{a}}_{k-1}^k, \hat{\underline{\mathbf{a}}}_{k-I}^{k-1}$ and the \mathbf{c}_k is the $I \times I$ lower principal submatrix of

$$\mathbf{C}_k = \begin{bmatrix} \cdot & \cdot \\ \cdot & \mathbf{c}_k \end{bmatrix} \quad (3.43)$$

\mathbf{N}_k is the $(I+1)$ -dimensional column vector of the differences between \tilde{a}_k 's and their mean values given $\underline{\mathbf{a}}_{k-1}^k, \hat{\underline{\mathbf{a}}}_{k-I}^{k-2}$, i.e.,

$$\mathbf{N}_k = [(\tilde{a}_k - \beta a_{k-1}), \dots, (\tilde{a}_{k-I-1} - \beta \hat{a}_{k-I})]^T \quad (3.44)$$

\mathbf{n}_k is the vector including the last I elements of \mathbf{N}_k , i.e.,

$$\mathbf{n}_k = [(\tilde{a}_{k-1} - \beta \hat{a}_{k-2}), \dots, (\tilde{a}_{k-I} - \beta \hat{a}_{k-I-1})]^T \quad (3.45)$$

Using (3.42) for the comparison metric calculation and canceling constant terms, we get

$$\mathcal{H}(a_k, a_{k-1}) = \ln \frac{\det \mathbf{C}_k}{\det \mathbf{c}_k} + \mathbf{N}_k^T \mathbf{C}_k^{-1} \mathbf{N}_k - \mathbf{n}_k^T \mathbf{c}_k^{-1} \mathbf{n}_k \quad (3.46)$$

Therefore, the decision strategy of the decision device is

$$\hat{a}_{k-1} = \begin{cases} 1, & \text{if } \min \mathcal{H}(a_k, a_{k-1}) = \{\mathcal{H}(0,1) \text{ or } \mathcal{H}(1,1)\} \\ 0, & \text{if } \min \mathcal{H}(a_k, a_{k-1}) = \{\mathcal{H}(0,0) \text{ or } \mathcal{H}(1,0)\} \end{cases} \quad (3.47)$$

The decision device computes the comparison metric given in (3.46) for each decision; thus, such a decision device is more complex than a simple quantizer as used for the MMSE equalizer in Section 3.4. In the performance analysis, we analyze the improvement in the performance of the MMSE-DFE after implementing a decision device that uses the metric given (3.46).

3.6 Adaptive Receiver

To recover the transmitted bits from the molecule concentration samples distorted by both the ISI and noise, we present the following methods: the MAP and ML sequence detectors, MMSE equalizer and MMSE-DFE in the previous sections. For each case, the RN needs the knowledge of the discrete-time equivalent channel coefficients of the diffusion-based MC channel, i.e., y_0 through y_I . However, the molecular diffusion channel is time-varying caused by the time variation of the diffusion coefficient D . Therefore, even if the RN knows the initial channel coefficients, since the molecular diffusion channel is time-varying, initial knowledge of the RN is not useful after the channel coefficients change.

To find the discrete-time equivalent coefficients of a channel that is unknown or time varying, we adopt a channel estimator presented in [54, 55]. The channel estimator of the RN recursively estimates the tap coefficients of the channel to minimize the MSE between the actual received sequence and the output of the estimator. That is, the channel estimator approximates the actual discrete-time equivalent channel with a similar structure to the actual channel. The steepest-descent algorithm can be used for the estimation of the channel tap coefficients. The operation of the channel estimator is as follows. Firstly, at each sampling time a new data sample z_k and the detected information bit for the corresponding data sample \hat{a}_k are fed to the channel estimator as illustrated in Fig. 3.7. The estimate for the data sample \tilde{z}_k is obtained by multiplying the sequence of detected bits $\{\hat{a}_j\}$ by the corresponding estimate of the coefficient $\{\tilde{y}_j\}$ and summing the results of all multiplications,

$$\tilde{z}_k = \sum_{j=0}^I \tilde{y}_j \hat{a}_{k-j}, \quad k = 0, 1, \dots \quad (3.48)$$

The difference between the data sample z_k and its estimate \tilde{z}_k at k th iteration step generates

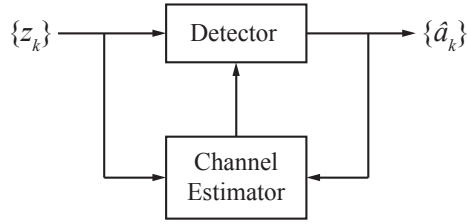


Figure 3.7: The conceptual model of the channel estimator using in a detector.

an error signal $\varepsilon^{(k)} = z_k - \tilde{z}_k$. To form a new set of estimates of the channel coefficients, the obtained error is used as

$$\tilde{y}_j^{(k+1)} = \tilde{y}_j^{(k)} + \Delta \varepsilon^{(k)} \hat{a}_{k-j}, \quad j = 0, 1, \dots, I - 1 \quad (3.49)$$

where $\tilde{y}_j^{(k)}$ is the estimate of the channel coefficient y_j at the k th iteration step, Δ is the step size, and \hat{a}_j is the j th detected information bit in the estimator. The speed of the convergence and the accuracy of the estimation are controlled by the value of the step size Δ . A delay equal to the decision delay of the transmitted bit is required to have a proper synchronization. When the MSE between z_k and \hat{z}_k is minimized, the estimates of the tap weight coefficients of the channel estimator are exactly equal to the equivalent discrete-time channel coefficients [54]. Furthermore, since the steepest descent algorithm is used in (3.49) to adjust the channel coefficient estimates, the channel estimator is able to track slow variations in the actual channel coefficients. We assume that the time variation of the molecular diffusion channel is slow compared to the convergence speed of the channel estimator. The channel estimator introduced in this section is compatible with all detectors presented above.

3.7 Performance Analysis

In this section, we present the performance analysis of the ML sequence detector, the MMSE equalizer and the MMSE-DFE detector. Since we assume that the transmitted information bits are equally likely, the MAP sequence detection is equivalent to the ML sequence detection. For the performance comparison of the proposed methods, the bit error

rates of the corresponding methods are considered. We use the Monte Carlo simulation to estimate the bit error rates. The bit error rates of the proposed detectors are evaluated with respect to the signal to noise ratio (SNR) at the RN which is defined as

$$\text{SNR} = \frac{P_y}{P_n} = \frac{\frac{1}{I+1} \sum_{n=0}^I |y_n|^2}{\text{E}[\sigma_k^2]} = \frac{\frac{1}{I+1} \sum_{n=0}^I |y_n|^2}{\frac{0.5}{V_R} \sum_{n=0}^I y_n} \quad (3.50)$$

where P_y and P_n are considered as the received signal power and the noise power, respectively, at the receiver. In the SNR definition, we use the expected value of the noise variance. As seen from (3.50), SNR depends on only the discrete time equivalent channel coefficients. Therefore, we change the amplitude of the concentration pulse A to change SNR values.

For an emitted concentration pulse, the noiseless concentration in the reception space $y(t)$ reaches its maximum at $t = t_{max}$ as stated above. Hence, we set the sampling time of RN as $T = t_{max}$ in order to sample the concentration with the highest SNR for a given concentration pulse amplitude A . Furthermore, the change in $y(t)$ at different communication distances causes t_{max} to change. Thus, the signaling interval $T = t_{max}$ and the information transmission rate $R = 1/T$ change with the communication distance. In the analysis, we set the molecule emission duration as

$$T_e = \frac{r^2}{6D_0} \quad (3.51)$$

where D_0 is the initial value of the diffusion coefficient D . The value of the T_e effects the ISI length and the signaling rate. The selection of the molecule emission duration depends on the application of the MC and the duration can be set in different ways. Since, we use the expression given in (3.51), the ISI length can be considered as $I + 1 = 6$ because $y(kT)$ for $k > 6$ becomes sufficiently small that can be ignored. Moreover, in the performance analysis, we use 2^5 -state trellis for the ML detector, $S = 6$ taps for the MMSE equalizer, $L = 6$ taps for the feedforward filter of the MMSE-DFE and $M = 10$ tap for the feedback filter of the MMSE-DFE. In the analysis, we set the radius the spherical reception space $\rho = 1\text{nm}$.

3.7.1 Time Invariant Channel

In this section, we consider the diffusion-based MC channel as time invariant by setting $D = 2.2 \times 10^{-9} \text{ m}^2/\text{s}$ and we assume that the channel is known at RN. The performances of the ML sequence detector, the MMSE equalizer, the MMSE-DFE using the decision metric given in (3.46), and the MMSE-DFE using the simple quantizer are analyzed. In Fig. 3.8(a), (b) and (c), bit error rates of the proposed detectors with respect to SNR for the communication distances $r = 50\text{nm}$, $r = 250\text{nm}$, and $r = 1\mu\text{m}$, respectively, are illustrated. We do not show the ML sequence detector performance beyond $\text{SNR} = 13\text{dB}$ since the Monte Carlo simulation takes too long time to compute. In the simulations, the signaling rates $R = 3.12\text{Mbps}$ for $r = 50\text{nm}$, $R = 127.9\text{kbps}$ for $r = 250\text{nm}$, and $R = 8.1\text{kbps}$ for $r = 1000\text{nm}$ are used. The first conclusion can be drawn from Fig. 3.8 is that for different distances, the performances of the considered methods are very similar. This is an expected result since the communication rates are adjusted at different communication distances in order to sample the concentration with the highest SNR for a given concentration amplitude A . Therefore, the same bit error rate can be achieved at a longer distance with a lower transmission rate.

Since the ML sequence detector is the optimum receiver, in the sense that it minimizes bit error probability of a sequence [54], it gives the best performance compared to the rest of the methods as seen in Fig. 3.8. On the other hand, the MMSE equalizer has the worst performance among the others. The MMSE-DFE detectors have better performance than the MMSE equalizer as expected. Furthermore, the MMSE-DFE with the decision device at the output is almost 2dB better than the MMSE-DFE with a simple quantizer at the output for a bit error rate equal to 10^{-4} . For SNR less than 10dB, the performances of the MMSE-DFE and MMSE equalizer are very close to each other. Then, we can conclude that using a feedback filter does not improve much the performance of the forward MMSE equalizer at low SNR values in the MC. Moreover, the performances of the proposed methods increase with an increase in the complexity. That is, the best performance is obtained by the ML detector which is the most complex detector and the MMSE equalizer which is the most simple detector gives the worst bit error rate.

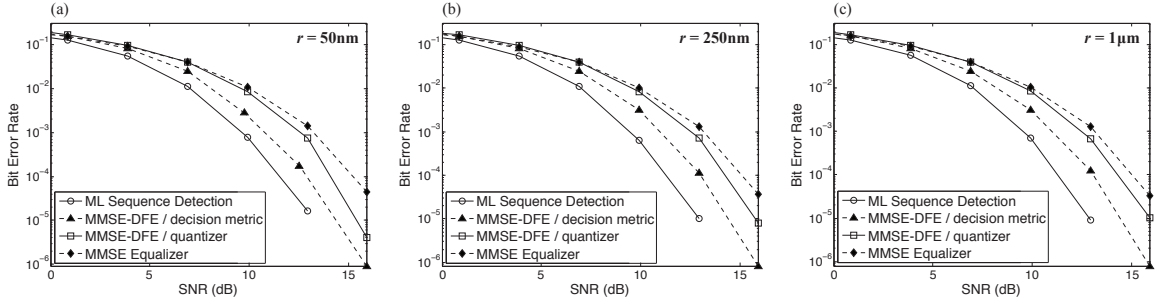


Figure 3.8: Bit error rates of four different detection approaches at different communication distances (a) $r = 50\text{nm}$, $R = 3.12\text{Mbps}$, (b) $r = 250\text{nm}$, $R = 127.9\text{kbps}$, and (c) $r = 1\mu\text{m}$, $R = 8.1\text{kbps}$ with same time invariant diffusion-based molecular channel known at RN.

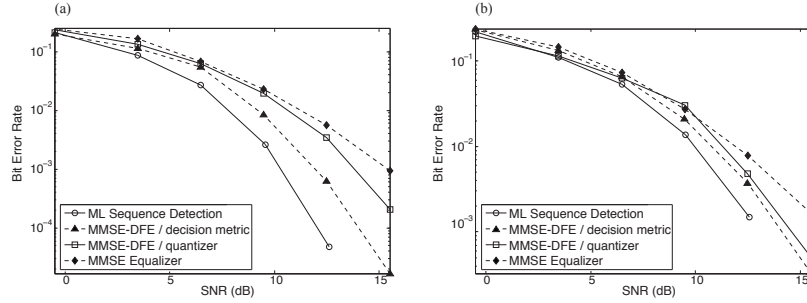


Figure 3.9: Bit error rates of four different detection methods for time varying diffusion-based molecular communication channels with (a) $D(t) = 2.2 \times 10^{-9} + 0.8 \times 10^{-9} \cos(2\pi t) \text{ m}^2/\text{s}$ and (b) $D(t) = 2.2 \times 10^{-9} + 0.8 \times 10^{-9} \cos(10\pi t) \text{ m}^2/\text{s}$.

3.7.2 Time Varying Channel

The diffusion-based MC channel has time varying characteristics depending on several factors as stated in Section II. In this part, we use the time varying diffusion channel together with the channel estimator described in Section 3.6 with a step size $\Delta = 0.001$ to investigate the performances of the proposed methods in more realistic conditions. In this part, we set the signaling rate $R = 8.1\text{kbps}$ at a communication distance $r = 250\text{nm}$ for the simulations. In the Fig. 3.9(a) and (b), the performance analyses of the proposed methods for $D(t) = 2.2 \times 10^{-9} + 0.8 \times 10^{-9} \cos(2\pi t) \text{ m}^2/\text{s}$ and $D(t) = 2.2 \times 10^{-9} + 0.8 \times 10^{-9} \cos(10\pi t) \text{ m}^2/\text{s}$, respectively, are shown. The time variation of the first channel is 5 times slower than the

time variation of the second channel. The performances of all methods decrease when the time varying channel is used, which can be seen when we compare Fig. 3.8(b) and Fig. 3.9. Although we use the channel estimator for the time varying channel, the detectors cannot exactly know the channel. That is, the transmitted information is recovered based on an estimate of the time varying channel coefficients which might decrease the performance of the proposed methods. Moreover, the convergence speed of the channel estimator should be fast enough to estimate the exact channel coefficients. The step size Δ can be adjusted according to the time variation characteristic of the channel. The performances of the proposed methods for a time varying channel whose time variation is faster can be seen in Fig. 3.9(b). We can say that the performances of all methods decrease with an increase in the time variation of the channel if the step size Δ is not adjusted accordingly.

Chapter 4

**NANOSCALE MAGNETO-INDUCTIVE COMMUNICATION
CHANNEL**

Nanonetworks constructed by interconnecting nanodevices using wireless communication allow nanodevices to perform more complex functions by means of cooperation between them. For the first time in the literature, we introduce a novel nanoscale wireless communication technique: Wireless Nanoscale Magneto-Inductive (WNMI) communication in which the magnetic coupling between nanocoils is used to establish a communication channel. The nanocoils considered in this chapter are formed by Carbon NanoTube (CNT) bundles. The WNMI communication solves high molecular absorption and frequency selective channel characteristics problems, which are encountered in nanoscale wireless electromagnetic communication, by introducing low absorption losses and flat channel characteristics. In this chapter, we first present the physical model of the point-to-point WNMI communication. Then, we introduce the waveguide technique for the WNMI communication. We derive path loss expressions for both of these methods. Afterwards, we present an information theoretical analysis for both the point-to-point and waveguide-based WNMI communication techniques to find their channel capacities. The performance analyses show that using waveguide technique in the WNMI communication significantly increases both the channel capacity and feasible communication range by greatly reducing the path loss. Based on the performance evaluations, the WNMI communication stands as a promising solution to nanoscale communication between nanodevices.

4.1 Introduction

Nanoscale communication between nanodevices is a quite novel and interdisciplinary concept which includes nanotechnology, biotechnology, and communication technology [1].

The nanonetworks constructed by interconnecting nanodevices expands the capabilities of single nanodevices by means of cooperation between them [2]. Several techniques in the literature are presented for the realization of the nanoscale communication namely electromagnetic, acoustic, or molecular communication [4], [5]. However, for the first time in the literature, we introduce a novel nanoscale wireless communication technique: Wireless Nanoscale Magneto-Inductive (WNMI) communication in which the magnetic coupling between nanocoils is used to form a wireless communication channel.

Using Electro-Magnetic (EM) waves for wireless communication at nanoscale has several disadvantages which are high absorption losses due to molecular absorption and frequency selective characteristics of the channel [61]. The molecular absorption loss is caused by the process by which part of the transmitted EM wave is converted into internal kinetic energy of some of the molecules in the communication medium [62]. In addition, since different molecule types have different resonant frequencies and the absorption at each resonance spreads over a range of frequencies, the nanoscale wireless EM communication channel is very frequency-selective [61].

The WNMI communication stands as a promising alternative method for nanoscale wireless communication because it solves the problems associated with the nanoscale wireless EM communication. First, since EM waves are not used, the WNMI communication mitigates the high absorption losses caused by molecular absorption. Second, in the WNMI communication, the channel conditions depend on the magnetic permeability of the medium [66]; thus, having a communication medium with uniform permeability enables constant channel conditions for the WNMI communication. A uniform channel can be created in a variety of media such as air, water, blood, and tissue liquid due to almost the same permeability. In spite of its advantages, the point-to-point WNMI communication is a short-range nanoscale communication since the strength of the magnetic field falls off much faster than that of EM waves [63, 65]. That is, whereas the molecular absorption in the WNMI communication is much less than that in the EM waves, the path loss of the WNMI communication may be higher than the EM communication. Nevertheless, the path loss in the WNMI communication can be greatly reduced and the communication range can be significantly increased by

forming a waveguide structure with passive relay nanonodes similar to waveguides employed in Magneto-Inductive (MI) communication [64, 66].

The MI communication has recently been introduced for wireless underground [65] and underwater communication [66]. Wireless communication with EM waves in these mediums is not feasible due to high attenuation rates. Since the magnetic permeability characteristics of underground and underwater environments are uniform and similar to air [65, 66], the MI communication is a promising method to communicate in dense mediums such as soil and water. Therefore, unlike the nanoscale wireless EM communication, the WNMI communication can be successfully utilized in solid, liquid or gas medium at the nanoscale. Furthermore, for nanomedicine applications, the WNMI communication can be employed in blood or tissue liquid without having very high attenuation rates. For example, in [67], a MI communication network is used to provide a communication link between implanted large-scale devices inside the human body, where the power for the implanted devices is provided using the MI communication. Thus, the WNMI communication can be efficiently and successfully utilized to establish a wireless communication link between implanted nanodevices inside the human body as well as between an outer device and implanted nanodevices.

In this chapter, we first present the model of the point-to-point WNMI communication between a single transmitter and a single receiver nanodevices. Both the transmitter and receiver nanodevices are equipped with a single nanocoil. As an extension of our previous study in [68], we assume that the nanocoils used for the WNMI communication are formed by Carbon NanoTube (CNT) bundles. Recently, the production and utilization of carbon nanocoils have been successfully realized using CNTs and CNT bundles [69, 70, 71]. At the nanoscale, CNT bundle-based nanocoils are more feasible than copper nanocoils due to the significantly higher conductivity and current carrying capabilities of CNTs than those of copper nanowires [72, 73]. Furthermore, since the geometry of square planar nanocoils is suitable for the manufacturing processes of integrated circuit production, we employ the square planar geometry for the nanocoils used in our model.

We use the equivalent circuit model of the transmitter and receiver nanocoils to derive an analytical expression for the path loss in the point-to-point WNMI communication chan-

nel. Then, we introduce the waveguide model for the WNMI communication by employing passive relay nanonodes between the transmitter and receiver nanodevices. We also obtain the analytical expression for the path loss in the WNMI communication waveguide. Afterwards, we have further extended our study in [68] by presenting an information theoretical analysis of both the point-to-point and waveguide-based WNMI communication techniques to find their channel capacities.

The rest of this chapter is organized as follows. In Section 4.2, we present the physical model of the point-to-point WNMI communication and underline the governing physical laws and mathematical formulations. In Section 4.3, we introduce the waveguide model of the WNMI communication. In Section 4.4, we present an information theoretical analysis for both the point-to-point and waveguide-based WNMI communication methods. In Section 4.5, we discuss the performance of the WNMI communication methods based on the numerical analyses of the path loss and channel capacity.

4.2 Physical Model of Point-to-Point WNMI Communication

In this section, we present the physical model of the point-to-point WNMI communication between a single Transmitter Nanodevice (TN) and a single Receiver Nanodevice (RN). In WNMI communication, the information transmission and reception are achieved using a CNT bundle-based nanocoil with a magnetic core in TN and RN, respectively. That is, the magnetic coupling between the transmitter and receiver nanocoils establishes the WNMI communication channel. Since CNT bundles have significantly higher conductivity and current carrying capabilities than those of copper nanowires, using CNT bundle-based nanocoils at the nanoscale is more feasible than using copper nanocoils [72, 73]. In addition, we use square planar nanocoils in our model due to their suitable geometry for the manufacturing processes of integrated circuit production. The schematic representation of a CNT bundle-based nanocoil is shown in Fig. 4.1(a). CNT bundles, which form a CNT bundle-based nanocoil, are composed of Single-Walled CNTs (SWCNTs) as seen in Fig. 4.1(b). The side view of a CNT bundle-based nanocoil is shown in Fig. 4.1(c).

The point-to-point WNMI communication model is demonstrated in Fig. 4.2(a), where

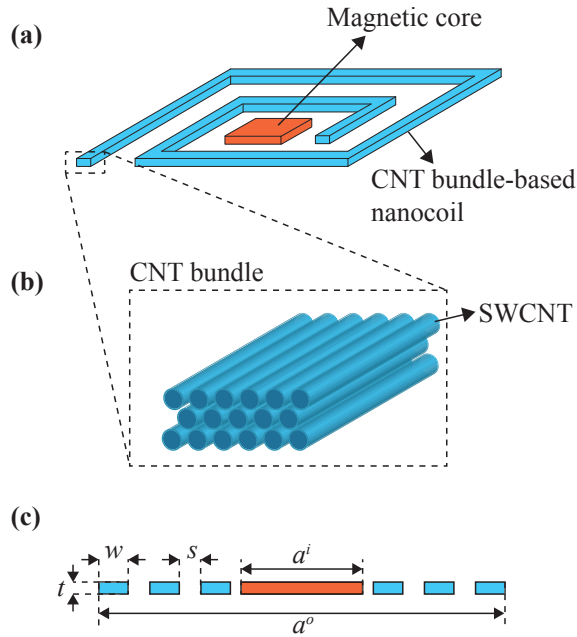


Figure 4.1: (a) The schematic representation of a CNT bundle-based nanocoil with square planar geometry. (b) The enlarged view of a CNT bundle constituting the CNT bundle-based nanocoil. (c) The side view of a CNT bundle-based nanocoil.

RN is located at a distance d from TN. A sinusoidal voltage source is used in TN, i.e., $v_T(t) = V_0 \cos(\omega t)$, where ω and V_0 are the angular frequency and amplitude of the voltage source, respectively. The sinusoidal voltage source causes a sinusoidal current to pass through the transmitter nanocoil. This current induces another sinusoidal current in the receiver nanocoil and the induced current is used to accomplish the WNMI communication between TN and RN. In Fig. 4.2(b), the transformer model of the WNMI communication is shown. The mutual inductance M between transmitter and receiver nanocoils represents the coupling between these coils. L_1 and L_2 are the self-inductances of the transmitter and receiver nanocoils, respectively. R_1 and R_2 are the resistances, and C_1 and C_2 are the parasitic capacitances of the nanocoils. Z_L is the load impedance which represents the current consumption of the nanochip included in RN. I_1 is the sinusoidal current passing through the transmitter nanocoil caused by the transmitter voltage source and I_2 is the sinusoidal current induced in the receiver nanocoil by I_1 . The voltage on the load impedance

is denoted by $v_R(t)$.

According to the transformer model illustrated in Fig. 4.2(b), the phasor analysis is given by

$$\begin{aligned} V_0 &= I_1 \left(R_1 + j\omega L_1 + \frac{1}{j\omega C_1} \right) - j\omega M I_2 \\ 0 &= I_2 \left(R_2 + j\omega L_2 + \frac{1}{j\omega C_2} + Z_L \right) - j\omega M I_1. \end{aligned} \quad (4.1)$$

Then, the equivalent circuit of the WNMI communication model can be derived as shown in Fig. 4.2(c) where

$$\begin{aligned} Z_1 &= R_1 + j\omega L_1 + 1/j\omega C_1 \\ Z_{21} &= \frac{\omega^2 M^2}{Z_L + R_2 + j\omega L_2 + 1/j\omega C_2} \\ Z_2 &= R_2 + j\omega L_2 + 1/j\omega C_2 \\ Z_{12} &= \frac{\omega^2 M^2}{R_1 + j\omega L_1 + 1/j\omega C_1} \\ V_M &= -j\omega M \frac{V_0}{R_1 + j\omega L_1 + 1/j\omega C_1}. \end{aligned} \quad (4.2)$$

Based on the equivalent circuit of the WNMI communication model, the transmitted power, denoted by P_t , and the received power, denoted by P_r , are given as

$$\begin{aligned} P_t &= \frac{1}{2} \text{Re} \left\{ \frac{|V_0|^2}{Z_1 + Z_{21}} \right\} \\ P_r &= \frac{1}{2} \text{Re} \left\{ \frac{Z_L |V_M|^2}{|Z_2 + Z_{12} + Z_L|^2} \right\} \end{aligned} \quad (4.3)$$

where $\text{Re}\{\cdot\}$ denotes the real part. The transmitted power P_t is defined as the power consumed in the transmitter nanocoil and the received power P_r is defined as the power consumed in the load impedance Z_L . To maximize the received power P_r , the load impedance is adjusted to be equal with the complex conjugate of the total impedance of the receiver nanocoil, i.e., $Z_L = Z_2^* + Z_{12}^*$. Hence, the received power becomes half of the total power consumed in the receiver nanocoil, i.e., $P_r = \text{Re}\{|V_M|^2/4(Z_2 + Z_{12} + Z_L)\}$. After some algebraic manipulations, the path loss in the point-to-point WNMI communication channel, denoted by P_L^{PTP} , is found as

$$P_L^{PTP} = \frac{P_t}{P_r} = 2 + 4 \frac{R_1 R_2}{\omega^2 M^2}. \quad (4.4)$$

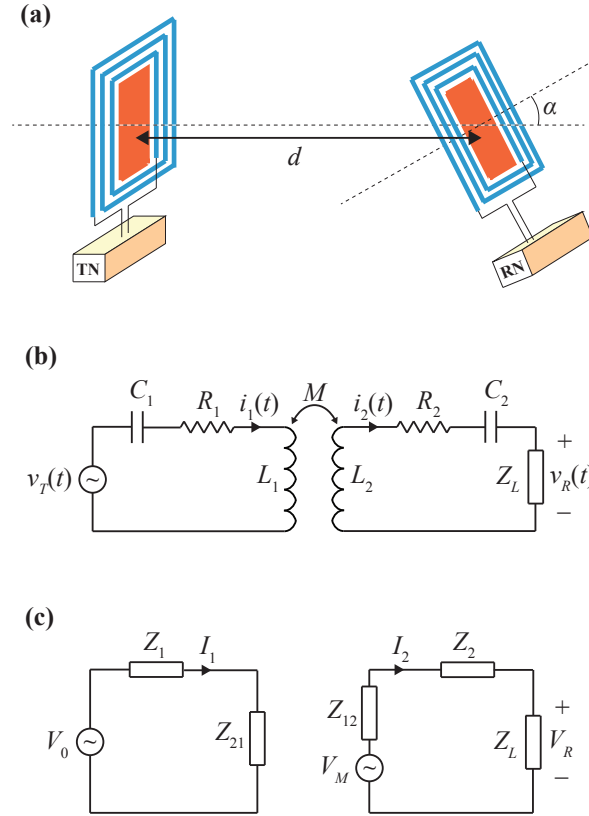


Figure 4.2: The WNMI communication model and circuit models of the WNMI communication. (a) The model of the WNMI communication. (b) The transformer model of the WNMI communication. (c) The equivalent circuit of the transformer model.

We assume that the transmitter and receiver nanocoils are identical. Thus, $R_1 = R_2 = R$, $C_1 = C_2 = C$, and $L_1 = L_2 = L$.

To be able to accurately characterize the resistance and inductance of a CNT bundle-based nanocoil, we adopt the equivalent conductivity model of CNT bundles presented in [74, 75]. The equivalent conductivity model is an efficient and accurate approximation of the magnetic inductance of the discrete SWCNTs with a single conductor which has the same dimensions as the CNT bundle. Both the magnetic inductance and the ohmic resistance characteristics of the CNT bundle are captured by adjusting the resistivity of the single

conductor to obtain a new effective resistivity, denoted by ρ_{eff} , which is given by

$$\rho_{\text{eff}} = \frac{\rho_c d_c^2}{P_m(1 - P_{\text{mod}})} \quad (4.5)$$

where ρ_c is the ohmic resistivity of an individual nanotube, d_c is the diameter of a SWCNT, P_m is the probability that a given SWCNT in the bundle is metallic, and P_{mod} is a modifier that accounts for the hexagonal spacing of bundles that results in one less SWCNT on every other row of a bundle as depicted in Fig. 4.1(b) [74]. Assuming CNTs are densely packed, P_{mod} is given as follows

$$P_{\text{mod}} = \frac{\lfloor 0.5n_h \rfloor d_c^2}{wt} \quad (4.6)$$

where w and t are the width and thickness of the CNT bundle, respectively, as shown in Fig. 4.1(c), and n_h is the number of nanotubes in the vertical dimension of the bundle given by $n_h = \lfloor t/d_c \rfloor$. Note that the equivalent conductivity model perfectly matches the ohmic resistance of an CNT bundle.

Since we use the equivalent conductivity model in this chapter, we treat a CNT bundle as a single conductor with a conductivity ρ_{eff} to find the inductance and resistance of a CNT bundle-based nanocoil. Therefore, we use the self-inductance model of a square planar nanocoil formed by a single conductor given in [76] as an accurate approximation for the self-inductance of a CNT bundle-based nanocoil which is given by

$$L = 1.17\mu \frac{N^2(a^o + a^i)}{1 + 2.75 \left(\frac{a^o - a^i}{a^o + a^i} \right)} \quad (4.7)$$

where a^o and a^i are the lengths of the inner and outer sides of the CNT bundle-based nanocoil, respectively, as illustrated in Fig. 4.1(c), N is the number of turns of the nanocoil, and μ is the magnetic permeability of the magnetic core of the nanocoil. The mutual inductance M between the transmitter and receiver nanocoils is expressed as

$$M = k\sqrt{L_1 L_2} = kL \quad (4.8)$$

where k is the coupling coefficient between the nanocoils. The coupling coefficient k can be given as [63]

$$k = \frac{\bar{a}^3}{8 \left(\sqrt{d^2 + \bar{a}^2/4} \right)^3} \cos(\alpha) \quad (4.9)$$

where d is the communication distance, i.e., the distance between transmitter and receiver nanocoils, α is the angle between the axes of the coupled coils, and \bar{a} is the average conductor side length of the square planar nanocoils, expressed as $\bar{a} = (a^i + a^o)/2$.

The resistance R of the CNT bundle-based nanocoils is found as follows

$$R = 4\bar{a}R_0N \quad (4.10)$$

where R_0 is the resistance of the unit length of the CNT bundle and it is given by $R_0 = \rho_{\text{eff}}/(wt)$ where ρ_{eff} is given in (4.5), w and t are the width and thickness of the CNT bundle, respectively. Then, assuming $d \gg \bar{a}$, the path loss expression becomes

$$P_L^{PTP} \approx \frac{748\Gamma^2 R_0^2 d^6}{\omega^2 \bar{a}^6 \mu^2 N^2 \cos^2(\alpha)} \quad (4.11)$$

where $\Gamma = 1 + 2.75 \frac{a^o - a^i}{a^o + a^i}$. The path loss is 6th-order function of d . Thus, an increase in the communication distance greatly reduces the received power. On the other hand, the received power can be increased by using a large signal frequency ω , a large number of turns N , a large average nanocoil side length \bar{a} , a large permeability of the magnetic core μ , and a small unit length resistance R_0 .

4.3 Waveguide Model for WNMI Communication

In the previous section, the WNMI communication channel was modeled for a point-to-point communication network. In the point-to-point WNMI communication, the received power falls off proportionally with d^6 which can be seen in (4.11). Therefore, the communication distance d has a severe effect on the received power, which limits the WNMI communication range. In this section, to increase the feasible communication range of the WNMI communication, we employ relay nanonodes between the transmitter and receiver nanocoils to form a magneto-inductive waveguide.

For the WNMI communication, the relay nanonodes are assumed to be passive devices; that is, a relay nanonode includes only a nanocoil and does not have a power source or processing circuitry. The signal propagation through the relay nanonodes is achieved by the magnetic coupling between nanocoils. That is, the sinusoidal current passing in the

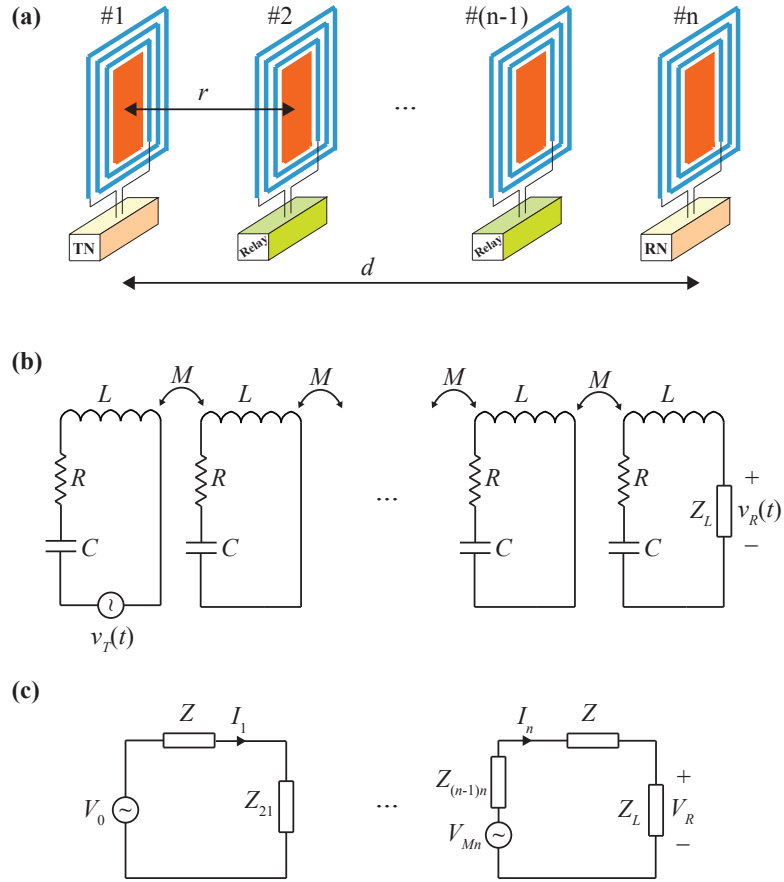


Figure 4.3: The waveguide model for the WNMI communication and circuit models of the waveguide. (a) The model of the WNMI communication waveguide. (b) The transformer model. (c) The equivalent circuit of the transformer model.

transmitter nanocoil induces a sinusoidal current in the nanocoil of the first relay nanonode. Then, the induced sinusoidal current in the first relay nanocoil also induces a sinusoidal current in the second relay nanocoil and the transmitted signal propagates in a similar manner until the induced current reaches the receiver nanocoil.

The waveguide model for the WNMI communication is shown in Fig. 4.3(a). In the waveguide, there are n identical nanocoils equally spaced including the nanocoils in the transmitter and receiver nanodevices. Therefore, if the inter-relay distance, i.e., the distance between two successive relay nanonode, is r , then, the communication distance between

transmitter and receiver nanocoils is given by $d = (n - 1)r$. Furthermore, we assume that only the adjacent nanocoils are magnetically coupled; hence, we only use the mutual inductance between the adjacent nanocoils.

The multi-stage transformer model for the WNMI communication waveguide is demonstrated in Fig. 4.3(b). The nanocoils in all nodes are assumed to be identical, and L , M , and R are given in (4.7), (4.8), and (4.10), respectively. The equivalent circuit model for the transmitter and receiver nanocoils can be seen in Fig. 4.3(c) where

$$\begin{aligned}
Z &= R + j\omega L + 1/j\omega C \\
Z_L &= Z^* + Z_{(n-1)n}^* \\
Z_{i(i-1)} &= \frac{\omega^2 M^2}{Z + Z_{(i+1)i}}; \quad i = 2, \dots, n \text{ and } Z_{(n+1)n} = Z_L \\
Z_{(i-1)i} &= \frac{\omega^2 M^2}{Z + Z_{(i-2)(i-1)}}; \quad i = 3, \dots, n \text{ and } Z_{12} = \frac{\omega^2 M^2}{Z} \\
V_{Mi} &= -j\omega M \frac{V_{M(i-1)}}{Z + Z_{(i-2)(i-1)}}; \quad i = 2, \dots, n \text{ and } V_{M1} = V_0
\end{aligned} \tag{4.12}$$

where Z_{ij} denotes the reflected impedance of the i^{th} nanocoil into the j^{th} nanocoil, and V_{Mi} denotes the induced voltage on the i^{th} nanocoil, which is similar to the results presented in [65]. According to the equivalent circuit of the WNMI communication waveguide, the transmitted power P_t and the received power P_r are expressed as

$$\begin{aligned}
P_t &= \frac{1}{2} \text{Re} \left\{ \frac{|V_0|^2}{Z + Z_{21}} \right\} \\
P_r &= \frac{1}{2} \text{Re} \left\{ \frac{|V_{Mn}|^2}{2(Z_L + Z + Z_{(n-1)n})} \right\}.
\end{aligned} \tag{4.13}$$

To maximize the received power, the angular frequency of the transmitted signal is chosen as the same as the resonant angular frequency of the equivalent RLC circuit of the planar nanocoil. The resonant angular frequency of the nanocoil is given as $\omega = 1/\sqrt{LC}$ and hence $j\omega L + (1/j\omega C) = 0$. Therefore, the impedance of a nanocoil becomes $Z = R$ and the path loss in the waveguide-based WNMI communication is given by

$$P_L^{WG} = \frac{P_t}{P_r} = \frac{2V_0^2}{|V_{Mn}|^2} \left(\frac{R + Z_{(n-1)n} + Z_L}{R + Z_{21}} \right) \tag{4.14}$$

where

$$Z_{(n-1)n} = \frac{\omega^2 M^2}{R + \frac{\omega^2 M^2}{R + \frac{\omega^2 M^2}{\ddots + Z_{12}}}} \quad (4.15)$$

$$Z_{21} = \frac{\omega^2 M^2}{R + \frac{\omega^2 M^2}{R + \frac{\omega^2 M^2}{\ddots + Z_L}}}$$

where $Z_{12} = \omega^2 M^2/R$, $Z_L = R + Z_{(n-1)n}$, and V_{Mn} is given in (4.12). Since the expression in (4.14) is too complicated to simplify, the effect of several WNMI communication parameters on the path loss in the waveguide-based WNMI communication is analyzed numerically in the performance evaluation section of this chapter.

4.4 Information Theoretical Analysis of WNMI Communication

In this section, we present an information theoretical analysis for both the point-to-point and waveguide-based WNMI communication methods to find their channel capacities. To be able to derive a closed-form expression for the channel capacity, we start from modeling the noise which arise in the WNMI communication.

At nanoscale, it can be assumed that the random thermal agitation of electrons moving through the CNTs is the major electrical noise source [77]. Thus, we consider the electrical thermal noise, which is called as the Johnson-Nyquist thermal noise, as the dominant noise source in the WNMI communication [78, 79]. The power spectral density of the Johnson-Nyquist thermal noise is nearly constant over the frequency spectrum and it can be approximated as a white Gaussian noise [80]. The power spectral density of the thermal noise is equal to $k_B T$ where T is the temperature of the communication medium in Kelvin and k_B is the Boltzmann constant given by $k_B = 1.38 \times 10^{-23}$ J/K. Although the total

noise power over the entire frequency spectrum is infinite because it is a white noise, the received noise power can be limited by using a simple filter having a bandwidth equal to B . Therefore, the total noise power over the bandwidth B is given as

$$P_n = k_B T B. \quad (4.16)$$

Since the thermal noise in the WNMI communication has white Gaussian characteristic, we use the classical channel capacity expression derived for channels having white Gaussian noise as follows

$$C = B \log_2 \left(1 + \frac{P_t/P_L}{P_n} \right) \quad (4.17)$$

where C is the channel capacity, B is the bandwidth of the WNMI communication channel, P_t is the transmitted power, P_L is the path loss, and P_n is the total noise power over the bandwidth B [38]. In both the point-to-point and waveguide-based WNMI communication methods, the path loss P_L depends on the frequency of the transmitted signal, i.e., the path loss increases as the signal frequency decreases as seen in (4.11). Thus, the channel bandwidth of the WNMI communication is limited by the path loss. In this chapter, we consider B as the 3dB bandwidth of the WNMI communication channel which is found by solving

$$P_L(f_c) = \frac{P_L(f_c - 0.5B)}{2} \quad (4.18)$$

where f_c is the central frequency of the transmitted signal defined by $f_c = \omega_c/2\pi$ and ω_c is the central angular frequency. That is, the path loss at the central frequency f_c is half of the path loss at the frequency $f_c - 0.5B$. In addition, to maximize the received power, we use the center frequency of the carrier signal as the same as the resonant frequency of the equivalent RLC circuit of the nanocoil, i.e., $f_c = 1/2\pi\sqrt{LC}$.

By using (4.11) to solve (4.18), the 3dB bandwidth of the point-to-point WNMI communication, denoted by B^{PTP} , can be easily found as follows

$$B^{PTP} = (2 - \sqrt{2}) f_c = \frac{2 - \sqrt{2}}{2\pi\sqrt{LC}}. \quad (4.19)$$

According to (4.19), the bandwidth of the point-to-point WNMI communication is directly proportional with the central frequency of the transmitted signal. The path loss expression

for the WNMI communication waveguide in (4.14) is too complex to derive an explicit formula for its the 3db bandwidth, denoted by B^{WG} . Therefore, we find B^{WG} numerically for the performance evaluation of the channel capacity.

The closed form expression of the channel capacity of the point-to-point WNMI communication, denoted by C^{PTP} , is found by substituting (4.7), (4.11), (4.19), and (4.16) in (4.17) as follows

$$C^{PTP} = \frac{0.192\sqrt{\Gamma}}{\pi N \sqrt{\mu \bar{a} C}} \log_2 \left(1 + \frac{\pi \bar{a}^{11/2} \mu^{3/2} N \cos^2(\alpha) P_t}{335 k_B T \Gamma^{3/2} R_0^2 d^6 C^{1/2}} \right) \quad (4.20)$$

The channel capacity of the waveguide-based WNMI communication, denoted by C^{WG} , is given by

$$C^{WG} = B^{WG} \log_2 \left(1 + \frac{P_t}{k_B T B^{WG} P_L^{WG}} \right) \quad (4.21)$$

where B^{WG} and P_L^{WG} are evaluated numerically for the performance evaluation of the waveguide-based WNMI communication channel capacity in the next section.

4.5 Performance Evaluation

In this section, we present the numerical performance analysis of both the point-to-point WNMI communication and the waveguide-based WNMI communication. We use the path loss and the channel capacity as the performance criterions and evaluate them with respect to several parameters namely the communication distance d , the relative permeability of the magnetic core μ_r , the outer side length of the nanocoils a^o , the thickness of the CNT bundle t , and the inter-relay distance r . The numerical evaluations are conducted on MATLAB.

In the numerical analyses, we keep the following parameters constant. For the dimensions of a CNT bundle-based nanocoil, we use $w = 4\text{nm}$ and $s = 1\text{nm}$ with $N = 5$ turns and we set $alpha = 0^\circ$. The diameter and resistivity of a SWCNT are given by $d_c = 1\text{nm}$ and $\rho_c = 10^{-8}\Omega\text{m}$, respectively [74, 81]. In addition, we consider the probability that a given SWCNT in the bundle is metallic as $P_m = 1$. We assume that the communication takes place at room temperature, i.e., $T = 300\text{K}$. We consider the parasitic capacitance of a CNT bundle-based nanocoil as $C = 0.01\mu\text{F}$. Since nanodevices cannot produce a large amount

of power, in order to get realistic results and according to the state of the art in molecular-electronics, we assume that the transmitted power by TN is $P_t = 1\text{nW}$. Furthermore, for the path loss analyses, we assume that the angular frequency of the signal source is the same as the resonant angular frequency of the equivalent RLC circuit of the CNT bundle-based nanocoil, i.e., $\omega = 1/\sqrt{LC}$.

4.5.1 Path Loss in Point-to-Point WNMI Communication

In this part, first, we numerically evaluate the path loss in the point-to-point WNMI communication P_L^{PTP} given in (4.11) with respect to the communication distance d for different relative magnetic permeabilities of the magnetic cores in the nanocoils. The relative magnetic permeability is defined as $\mu_r = \mu/\mu_0$ where μ_0 is the magnetic permeability of free space given by $\mu_0 = 4\pi \times 10^{-7}\text{H/m}$. In this part of the numerical analyses, we assume that the outer side length of the nanocoils is $a^o = 50\text{nm}$ and the thickness of the CNT bundle is $t = 10\text{nm}$. The numerical evaluation results of P_L^{PTP} in dB are illustrated in Fig. 4.4(a). According to the results, the path loss increases with an increase in the communication distance, which can be also seen in (4.11). For example, for $\mu_r = 1000$, $P_L^{PTP} = 41.1\text{dB}$ at $d = 5\text{mm}$ and $P_L^{PTP} = 101.1\text{dB}$ at $d = 50\text{mm}$. As the communication distance increases, first, the path loss exhibits a fast increase and then, it slowly increases. As a result, considering the power limitation of the nanodevices, the practical communication range of the point-to-point WNMI communication is short. Furthermore, based on the results presented in Fig. 4.4(a), an increase in the relative permeability μ_r decreases the path loss, which can be clearly seen in (4.11). For all communication distances analyzed in this part, increasing μ_r from 500 to 2500 decreases the path loss by 7dB. Therefore, using a magnetic core with large permeability in the nanocoil improves the achievable communication range of the point-to-point WNMI communication by decreasing the path loss.

Next, we analyze the path loss in the point-to-point WNMI communication with respect to the outer side length of the nanocoils a^o with different thicknesses of the CNT bundle t . For this part, we assume that the communication distance is $d = 5\text{mm}$ and the relative magnetic permeability is $\mu_r = 1000$. The results are shown in Fig. 4.4(b). According

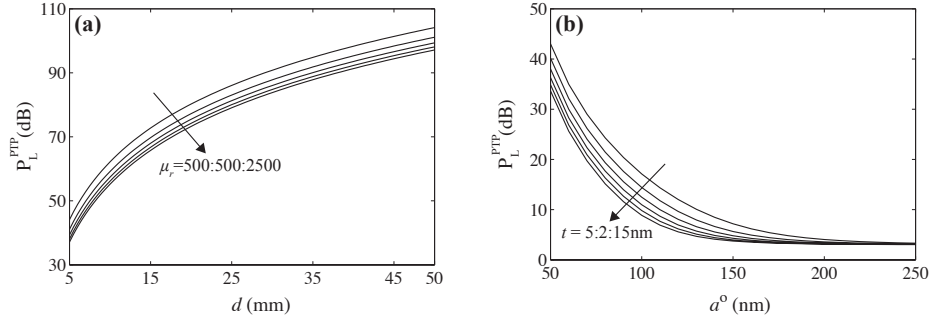


Figure 4.4: The path loss in the point-to-point WNMI communication P_L^{PTP} with respect to (a) the communication distance d for different relative permeability values μ_r and (b) the outer side length of the nanocoils a^o for different thicknesses of the CNT bundle t .

to the results, the path loss decreases with an increase in a^o . For instance, for $t = 5\text{nm}$, $P_L^{PTP} = 43.0\text{dB}$ for $a^o = 50\text{nm}$ and $P_L^{PTP} = 3.2\text{dB}$ for $a^o = 250\text{nm}$. In addition, for $a^o > 200\text{nm}$, the path loss is approximately constant at $P_L^{PTP} = 3.2\text{dB}$. Moreover, based on the results revealed in Fig. 4.4(b), the path loss decreases with an increase in the thicknesses of the CNT bundle, which is an expected result according to (4.11). For example, for $a^o = 50\text{nm}$, increasing t from 5nm to 15nm decreases the path loss by 9.37dB . As a result, increasing the outer side length of the nanocoil and the thickness of the CNT bundle increases the feasible communication range of the WNMI communication by reducing the path loss.

4.5.2 Path Loss in WNMI Communication Waveguide

In this part, we begin with the analysis of the path loss in the WNMI communication waveguide P_L^{WG} given in (4.14) with respect to the communication distance d for different relative magnetic permeabilities μ_r . For this analysis, we assume that the outer side length of the nanocoils is $a^o = 50\text{nm}$ and the thickness of the CNT bundle is $t = 10\text{nm}$. Furthermore, the inter-relay distance in the waveguide is constant and given by $r = 0.5\text{mm}$. The communication distance is increased by increasing the number of relay nanocoils in the waveguide. Note also that, the relay nanocoils in the waveguide do not require any

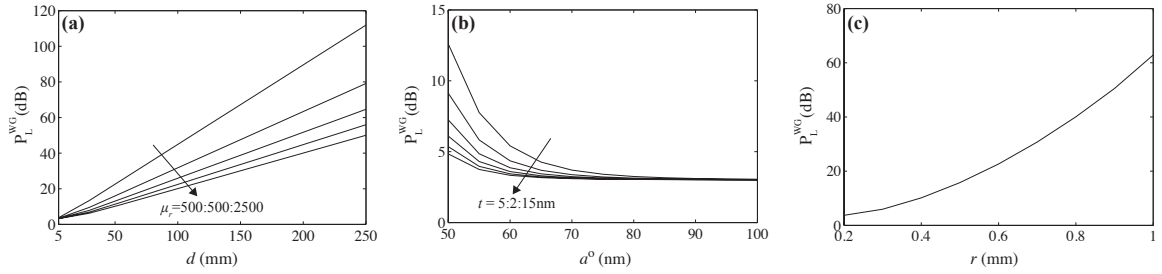


Figure 4.5: The path loss in the WNMI communication waveguide P_L^{WG} with respect to (a) the communication distance d for different relative permeability values μ_r , (b) the outer side length of the nanocoils a^o for different thicknesses of the CNT bundle t , and (c) the inter-relay distance r .

power. According to the results illustrated in Fig. 4.5(a), an increase in the communication distance increases the path loss. For instance, for $\mu_r = 1000$, $P_L^{WG} = 3.3$ dB at $d = 5$ mm, $P_L^{WG} = 15.1$ dB at $d = 50$ mm, and $P_L^{WG} = 79.5$ dB at $d = 250$ mm. Note that, for the same communication distances, the waveguide technique greatly reduces the path loss compared with the point-to-point WNMI communication. Although the path loss in dB abruptly increases in the point-to-point WNMI communication as the communication distance increases, in the WNMI waveguide, the path loss in dB increases linearly with a small slope compared with the point-to-point case. As a result, by using the waveguide technique, the range of the WNMI communication is significantly increased by greatly decreasing the path loss. Based on the results, the waveguide-based WNMI communication stands as a promising solution to long range nanoscale communication. Moreover, based on the results shown in Fig. 4.5(a), an increase in the relative permeability μ_r decreases the path loss. For example, for $d = 100$ mm, increasing μ_r from 500 to 2500 decreases the path loss by 25.9dB. Hence, using magnetic cores in the nanocoils with large permeabilities also greatly improves the feasible communication range of the waveguide-based WNMI communication by reducing the path loss.

In the second of part the path loss analysis for the WNMI communication waveguide, we investigate the path loss P_L^{WG} with respect to the outer side length of the nanocoils a^o with different thicknesses of the CNT bundle t . For this analysis, we assume that the

communication distance is $d = 20\text{mm}$, the relative magnetic permeability is $\mu_r = 1000$, and the inter-relay distance is $r = 0.5\text{mm}$. The results are demonstrated in Fig. 4.5(b). According to the results, the path loss decreases with an increase in a^o . For example, for $t = 5\text{nm}$, $P_L^{WG} = 12.6\text{dB}$ for $a^o = 50\text{nm}$ and $P_L^{WG} = 3.0\text{dB}$ for $a^o = 100\text{nm}$. Furthermore, for $a^o > 80\text{nm}$, the path loss stays approximately constant at $P_L^{WG} = 3.0\text{dB}$. Moreover, based on the results revealed in Fig. 4.5(b), the path loss decreases with an increase in the thicknesses of the CNT bundle. For instance, for $a^o = 50\text{nm}$, increasing t from 5nm to 15nm decreases the path loss by 7.8dB . Therefore, appropriately increasing the outer side length of the nanocoils and the thickness of the CNT bundle increases the feasible communication range of the waveguide-based WNMI communication by greatly decreasing the path loss.

In the last part of the path loss analysis for the waveguide, we analyze the path loss P_L^{WG} with respect to the inter-relay distance r . For this part of the analysis, we assume that the outer side length of the nanocoils is $a^o = 50\text{nm}$, the thickness of the CNT bundle is $t = 10\text{nm}$, the communication distance is $d = 50\text{mm}$, and the relative magnetic permeability is $\mu_r = 1000$. According to the results shown Fig. 4.5(c), the path loss increases with an increase in the inter-relay distance. As r increases, the magnetic coupling between relay nanonodes becomes weak causing the path loss between two relays to increase with an increase in the distance between them as shown in Fig. 4.4(a). Thus, in the waveguide, the total path loss between TN and RN becomes more severe as r is increased. For example, $P_L^{WG} = 3.7\text{dB}$ for $r = 0.2\text{mm}$ and $P_L^{WG} = 62.9\text{dB}$ for $r = 1.0\text{mm}$. Note that, although decreasing the inter-relay distance greatly reduces the path loss, the cost of the waveguide with a shorter inter-relay distance is increased because the number of relay nanocoils in the waveguide is increased. Therefore, the inter-relay distance is selected in accordance with the desired path loss and the cost of the waveguide.

4.5.3 Channel Capacity of Point-to-Point WNMI Communication

For the channel capacity analysis, we first numerically evaluate the channel capacity of the point-to-point WNMI communication C^{PTP} given in (4.20) with respect to the communication distance d for different relative magnetic permeabilities of the magnetic cores

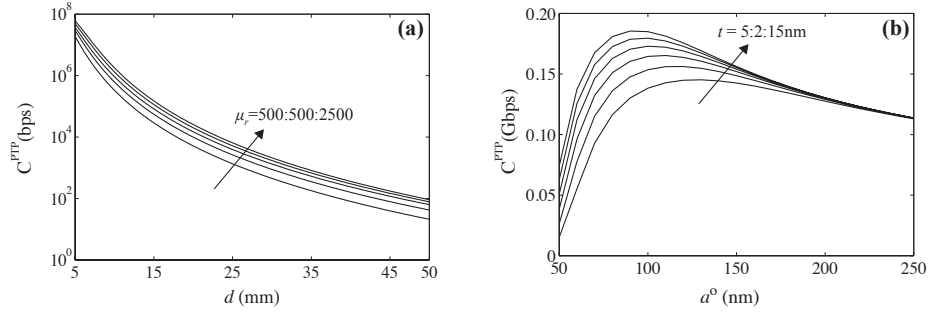


Figure 4.6: The channel capacity of the point-to-point WNMI communication C^{PTP} with respect to (a) the communication distance d for different relative permeability values μ_r and (b) the outer side length of the nanocoils a^o for different thicknesses of the CNT bundle t .

in the nanocoils. For this analysis, we assume that the outer side length of the nanocoils is $a^o = 50\text{nm}$ and the thickness of the CNT bundle is $t = 10\text{nm}$. The numerical evaluation results of C^{PTP} in bps are illustrated in Fig. 4.6(a). Based on the results, the channel capacity decreases with an increase in the communication distance, which can be also seen in (4.20). For example, for $\mu_r = 1000$, $C^{PTP} = 43.9\text{Mbps}$ at $d = 5\text{mm}$ and $C^{PTP} = 65.8\text{bps}$ at $d = 50\text{mm}$. As the communication distance increases, the channel capacity falls sharply because the received power declines proportionally with d^6 in the point-to-point WNMI communication. Furthermore, according to the results presented in Fig. 4.6(a), an increase in the relative permeability μ_r increases the channel capacity. For instance, for $d = 5\text{mm}$, increasing μ_r from 500 to 2500 increases the channel capacity from 27.6Mbps to 62.3Mbps. Thus, using a magnetic core with large permeability in the nanocoil greatly improves the channel capacity of the point-to-point WNMI communication.

Next, we analyze the channel capacity of the point-to-point WNMI communication with respect to the outer side length of the nanocoils a^o with different thicknesses of the CNT bundle t . For this part, we assume that the communication distance is $d = 5\text{mm}$ and the relative magnetic permeability is $\mu_r = 1000$. The results are shown in Fig. 4.6(b). According to the results, first, the channel capacity increases with an increase in a^o up to a certain value of a^o . Then, the capacity declines as a^o is increased. That is, the channel capacity is a concave function of a^o . Therefore, for a given t , the channel capacity can be

maximized by appropriately choosing the value of a^o according to the capacity expression in (4.20). For instance, for $t = 5\text{nm}$, the channel capacity is maximized and it reaches $C^{PTP} = 144.8\text{Mbps}$ when $a^o = 120\text{nm}$. Note that, for $t = 5\text{nm}$, $C^{PTP} = 15.2\text{Mbps}$ for $a^o = 50\text{nm}$ and $C^{PTP} = 113.0\text{Mbps}$ for $a^o = 250\text{nm}$. Furthermore, based on the results revealed in Fig. 4.6(b), the channel capacity increases with an increase in the thicknesses of the CNT bundle. For example, for $a^o = 50\text{nm}$, increasing t from 5nm to 15nm increases the channel capacity from 15.2Mbps to 74.3Mbps . Thus, the channel capacity of the point-to-point WNMI communication can be significantly increased by appropriately adjusting the outer side length of the nanocoils and the thickness of the CNT bundle.

4.5.4 Channel Capacity of WNMI Communication Waveguide

In this part, first, we analyze the channel capacity of the WNMI communication waveguide C^{WG} given in (4.21) with respect to the communication distance d for different relative magnetic permeabilities μ_r . For this analysis, we assume that the outer side length of the nanocoils is $a^o = 50\text{nm}$ and the thickness of the CNT bundle is $t = 10\text{nm}$. Furthermore, the inter-relay distance in the waveguide is constant and given by $r = 0.5\text{mm}$. We increase the communication distance by increasing the number of relay coils in the waveguide. Based on the results shown in Fig. 4.7(a), an increase in the communication distance reduces the channel capacity. For instance, for $\mu_r = 1000$, $C^{WG} = 192.2\text{Mbps}$ at $d = 50\text{mm}$ and $C^{WG} = 3.1\text{kbps}$ at $d = 250\text{mm}$. Note that, for the same communication distance, the WNMI communication waveguide has significantly larger channel capacity compared with the point-to-point WNMI communication. Thus, the waveguide-based WNMI communication supports very high transmission bit-rates for long range nanoscale communication. Moreover, based on the results shown in Fig. 4.5(a), an increase in the relative permeability μ_r greatly increases the channel capacity. For example, for $d = 200\text{mm}$, increasing μ_r from 500 to 2500 increases the channel capacity from 0.24kbps to 12.5Mbps . Therefore, using a magnetic core with a large permeability in the nanocoils significantly improves the channel capacity of the waveguide.

In the second of part, we analyze the channel capacity of the waveguide-based WNMI

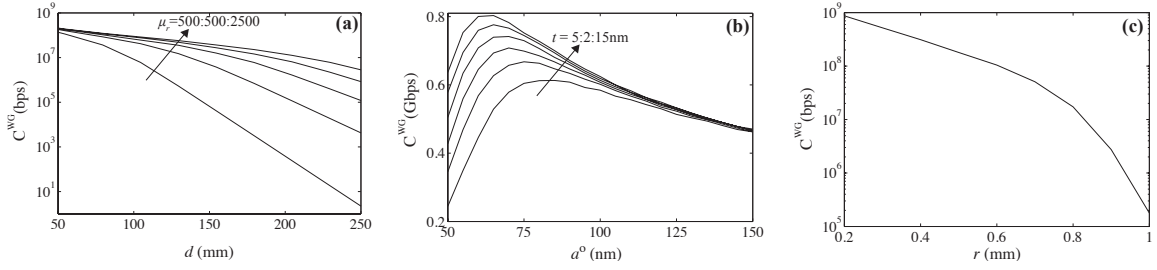


Figure 4.7: The channel capacity of the WNMI communication waveguide C^{WG} with respect to (a) the communication distance d for different relative permeability values μ_r , (b) the outer side length of the nanocoils a^o for different thicknesses of the CNT bundle t , and (c) the inter-relay distance r .

communication C^{WG} with respect to the outer side length of the nanocoils a^o with different thicknesses of the CNT bundle t . For this analysis, we assume that the communication distance is $d = 20$ mm, the relative magnetic permeability is $\mu_r = 1000$, and the inter-relay distance is $r = 0.5$ mm. The results are demonstrated in Fig. 4.7(b). According to the results, first, the channel capacity increases with an increase in a^o until a certain value of a^o . Then, the capacity decreases when a^o is increased. Since for a given t , the channel capacity is a concave function of a^o , the channel capacity of the WNMI communication waveguide can be maximized by selecting the value of a^o according to the capacity expression in (4.21). For example, for $t = 5$ nm, the channel capacity reach its maximum value given by $C^{PTP} = 612.5$ Mbps when $a^o = 80$ nm. Note that, $C^{PTP} = 244.5$ Mbps for $a^o = 50$ nm and $C^{PTP} = 462.5$ Mbps for $a^o = 150$ nm. Moreover, based on the results illustrated in Fig. 4.7(b), the channel capacity increases with an increase in the thicknesses of the CNT bundle. For instance, for $a^o = 50$ nm, increasing t from 5nm to 15nm increases the channel capacity from 244.5Mbps to 636Mbps. As a result, by appropriately selecting the outer side length of the nanocoil and the thickness of the CNT bundle, the channel capacity of the WNMI communication waveguide can be significantly improved.

In the last part of the channel capacity analysis for the waveguide, we investigate the effect of the inter-relay distance r on the channel capacity C^{WG} . For this part, we assume that the outer side length of the nanocoils is $a^o = 50$ nm, the thickness of the CNT bundle is

$t = 10\text{nm}$, the communication distance is $d = 50\text{mm}$, and the relative magnetic permeability is $\mu_r = 1000$. According to the results shown Fig. 4.7(c), the channel capacity decreases with an increase in the inter-relay distance. As we discuss in Section 4.5.2, as r increases, the path loss in the WNMI communication waveguide increases, which causes the received power to decrease. As a result, the channel capacity also decreases with an increase in r . For example, $C^{WG} = 869.8\text{Mbps}$ for $r = 0.2\text{mm}$ and $C^{WG} = 178.3\text{kbps}$ for $r = 1.0\text{mm}$. The inter-relay distance r causes a trade off between the channel capacity and the cost of the waveguide. That is, as the inter-relay distance is increased, the channel capacity is increased but the cost of the waveguide is also increased because for the same communication distance, more relay nanocoils are required when the inter-relay distance becomes shorter. Therefore, for a given communication distance, the inter-relay distance in the waveguide can be adjusted according to the desired channel capacity and the total cost of the waveguide.

Chapter 5

NANOSCALE HEAT COMMUNICATION CHANNEL

Nanonetworks constructed by interconnecting nanodevices using wireless communication allows the nanodevices to perform more complex functions by means of cooperation between them. For the first time in the literature, we introduce a novel and physically realizable nanoscale communication technique: Nanoscale Heat Communication (NHC) in which the heat transfer is used for communication at the nanoscale. The transmitted information is encoded in temperature signals using the MagnetoCaloric Effect (MCE) which is the change in temperature of a magnetic material exposed to a varying magnetic field. Thermal energy emitted or absorbed by a transmitter nanodevice is subject to the laws of thermal diffusion which changes the temperature of the communication medium. The transmitted information is decoded by a receiver nanodevice that senses the temperature variations. We derive an analytical expression for signal-to-noise ratio (SNR) in the NHC. Using the information theoretical analysis, we obtain the closed-form expression for the channel capacity. According to the performance evaluation of the channel capacity, the NHC provides a significantly higher capacity communication compared with the existing nanoscale communication techniques. Therefore, the NHC stands as a promising solution to nanoscale communication between nanomachines based on its channel capacity performance, advantages, and possible applications for emerging nanonetworks.

5.1 Introduction

Nanoscale communication between nanodevices is a quite novel and interdisciplinary concept which includes nanotechnology, biotechnology, and communication technology [1]. The nanonetworks constructed by interconnecting nanodevices expand the capabilities of single nanodevices by means of cooperation between them [2]. The realization of the nanoscale

communication can be achieved through electromagnetic, acoustic, or molecular communication [4, 5]. Although recently, Molecular Communication (MC) is considered as a promising solution for the communication of nanodevices [7, 17], there are several disadvantages of MC. For example, the limitation in the molecule storage of a nanodevice restricts the lifetime of a nanonetwork and makes the MC impractical. On the other hand, refilling the molecule storage of a nanodevice is very challenging. Furthermore, in the MC, the emission of the signal molecules in the communication medium may result in undesired accumulation of these molecules.

For the first time in the literature, we introduce a novel and radically different nanoscale communication concept: Nanoscale Heat Communication (NHC) in which the heat transfer is used for communication at the nanoscale. The NHC is based on the diffusion of the thermal energy. That is, the temperature of the transmitter nanodevice is modulated according to the transmitted information. The thermal energy emitted due to an increase in the temperature of the transmitter or absorbed due to a decrease in the temperature of the transmitter changes the temperature at the receiver location due to the laws of thermal diffusion. Then, the temperature variation at the receiver location is sensed by the receiver nanodevice using a thermal nanosensor.

The temperature modulation of the transmitter nanodevice is achieved by using the MagnetoCaloric Effect (MCE) which is a well-known phenomenon defined as the change in temperature of magnetic materials exposed to a varying magnetic field [82]. We use the MCE in the NHC because it can be successfully implemented for temperature modulation at nanoscale. By utilizing a nanosolenoid to create a magnetic field and a magnetic nanoparticle, the transmitter nanodevice can modulate the temperature of the nanoparticle to transmit the desired information. Recently, the production and utilization of carbon nanosolenoids have been successfully realized using carbon nanotubes (CNTs) [83, 84, 85]. In addition, the theoretical analyses of the CNT bundle-based inductors are presented in [86, 87]. CNTs bundle-based inductors have been proposed as a possible replacement for copper inductors due to their high conductivity and current carrying capabilities [88, 89].

Magnetic nanoparticles have been used for their ability to exhibit large MCE; e.g., the

temperature of gadolinium (Gd) nanoparticles can be increased by 2K at room temperature by applying a magnetic field having approximately 500mT strength [90]. For instance, magnetic nanoparticles are utilized in an experimental cancer treatment called magnetic hyperthermia in which the MCE is used to heat and kill a tumor [91]. Furthermore, according to the results revealed in [83], CNT-based nanosolenoids having a magnetic core with high permeability might generate a magnetic field with a strength on the order of hundreds of mT. Hence, the MCE can be conveniently utilized in the NHC to modulate the temperature of a magnetic nanoparticle. As a result, unlike the most of the existing nanoscale communication methods in the literature, the NHC technique is physically realizable and hence, the NHC can be experimentally validated.

The NHC is based on the diffusion of the thermal energy; thus, the NHC and MC are similar because the MC depends on the diffusion of molecules. However, the NHC does not have the disadvantages of the MC. In the NHC, the electrical energy is converted to the thermal energy. Therefore, in the NHC, a nanobattery is enough to provide power required for the communication unlike the MC. Recently, novel energy harvesting techniques have been proposed to recharge the energy stored in the nanobatteries [92]. For instance, an experimental study for a piezoelectric nanogenerator is shown in [93]. Thus, by using these techniques, it is possible to overcome the energy bottleneck of nanonetworks and to make their lifetime infinite.

Unlike the MC, binary bipolar encoding can be used in the NHC. That is, the temperature of the transmitter nanodevice can be modulated according to the binary bipolar encoding using the MCE. As a result, the expected temperature variation of the communication medium due to NHC becomes zero. However, in the MC, the accumulation of the molecules in the communication medium is an inevitable result [14]. Furthermore, the NHC can take place in all three states of the matter since the thermal diffusion occurs in all the states. However, the MC can be realized only in a liquid [8]. The implementation of the NHC is simple compared with the MC since a nanodevice can become a transmitter by incorporating a nanosolenoid and a magnetic nanoparticle into the nanodevice and, similarly, a nanodevice can receive the transmitted temperature signals only by using a thermal

Table 5.1: Comparison Table of Molecular Communication and Nanoscale Heat Communication

Property	Molecular Communication	Nanoscale Heat Communication
Physical phenomenon	<i>Molecular diffusion</i>	<i>Thermal diffusion</i>
Lifetime	<i>Limited</i>	<i>Unlimited</i>
Communication Medium	<i>Liquid</i>	<i>Solid, liquid, gas</i>
Effect on medium	<i>Molecule accumulation</i>	<i>No total effect</i>
Implementation	<i>Complex</i>	<i>Simple</i>

nanosensor. The summary of the comparison of the NHC and the MC is given in Table 5.1. The NHC stands as a promising solution to realize nanoscale communication between nanomachines based on its advantages over the MC.

The rest of this chapter is organized as follows. In Section 5.2, we explain the basic concepts of MCE and underline the governing physical laws and its mathematical formulations. In Section 5.3, we describe the physical model of the NHC and explain how each of the components in the communication model works. In Section 5.4, we perform an information theoretical analysis of the NHC to determine the closed-form expression for the channel capacity and the signal-to-noise ratio (SNR). Section 4.5 presents numerical analyses of both the channel capacity and the SNR for the NHC channel.

5.2 Theory of Magnetocaloric Effect

In [82], Warburg defines the MagnetoCaloric Effect (MCE) as the response of magnetic materials to a varying magnetic field which manifests as a change in the entropy and temperature of the magnetic material. The nature of the MCE is explained later and its practical use to reach ultralow temperatures is suggested independently in studies [94] and [95]. In [96], it is shown that the temperatures below 1K can be achieved successfully by the use of the MCE. Furthermore, the model of the first magnetic refrigerator working at room temperature is demonstrated in [97].

The MCE is an intrinsic property of all magnetic materials and is caused by the coupling

of the magnetic sublattice with the magnetic field [98]. In Fig. 5.1, the thermodynamics of the MCE for a ferromagnet, i.e., the entropy of the ferromagnetic material S with respect to the temperature T , for both zero magnetic field H_0 and a nonzero magnetic field H_1 is schematically illustrated. If the magnetic field H_1 is applied to the ferromagnet in an adiabatic process¹ in which the total entropy of the system remains constant, the temperature of the system increases due to MCE, which is called the adiabatic temperature change and denoted by ΔT_{ad} . The adiabatic temperature change can be visualized as the temperature difference between (S_0, T_0) and (S_0, T_1) points shown in Fig. 5.1 by the horizontal arrow, i.e., $\Delta T_{ad} = T_1 - T_0$.

The MCE can also be expressed by means of the entropy change, denoted by ΔS , when the magnetic field H_1 is applied to the ferromagnet in an isothermal process². Similar to the isothermal compression of a gas, the isothermal magnetizing of a soft ferromagnet or a paramagnet reduces the entropy of the material and the isothermal demagnetizing restores the zero magnetic field entropy of the material similar to the isothermal expansion of a gas. The isothermal entropy change is represented by the difference between (S_0, T_0) and (S_1, T_0) points illustrated in Fig. 5.1 by the vertical arrow, i.e., $\Delta S = S_0 - S_1$.

The isothermal entropy change ΔS and the adiabatic temperature change ΔT_{ad} represent two quantitative characteristics of the MCE. The ΔS and ΔT_{ad} are derived using one of the fundamental Maxwell's relations [99]

$$\left(\frac{\partial S(T, H)}{\partial H}\right)_T = \left(\frac{\partial M(T, H)}{\partial T}\right)_H \quad (5.1)$$

where $S(T, H)$ is the total entropy, $M(T, H)$ is the magnetization, H is the magnetic field strength, T is the absolute temperature and the subscript outside the parentheses indicates which variable is being held constant during differentiation. For an isothermal process, the

¹An adiabatic process is defined as a process occurring without input or output of heat within a system, i.e., the system is thermodynamically isolated. Therefore, by the second law of thermodynamics, in an adiabatic process the entropy of the system does not change.

²An isothermal process is defined as a process in which the temperature remains constant. In an isothermal process, there is heat transfer between the system and the surroundings which causes the entropy of the system change by the second law of thermodynamics.

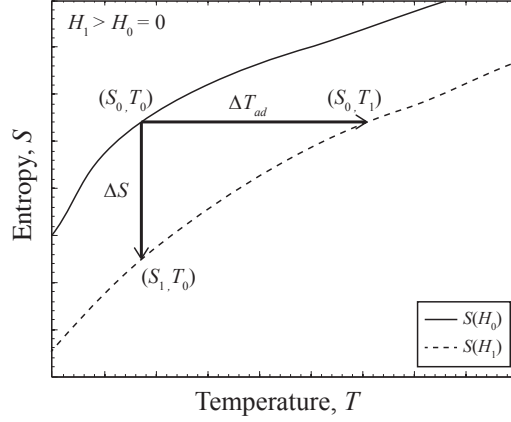


Figure 5.1: The schematic demonstration of the entropy of the ferromagnetic material with respect to the temperature for zero magnetic field H_0 and a nonzero magnetic field H_1 .

integration of the expression given in (5.1) yields

$$\Delta S = \int_{H_i}^{H_f} \left(\frac{\partial M(T, H)}{\partial T} \right)_H dH \quad (5.2)$$

where H_i and H_f are the initial and final magnetic fields, respectively, applied to the magnetic material. According to (5.2), the isothermal entropy change is proportional to the magnetic field change and to the derivative of the magnetization with respect to temperature at constant magnetic field. Furthermore, for an adiabatic process, another fundamental expression to describe the MCE is [99]

$$\Delta T_{ad} = - \int_{H_i}^{H_f} \frac{T}{C(T, H)_H} \left(\frac{\partial M(T, H)}{\partial T} \right)_H dH \quad (5.3)$$

where $C(T, H)_H$ is the heat capacity of the magnetic material at constant magnetic field as indicated by the subscript H . Therefore, the adiabatic temperature change is directly proportional to the absolute temperature, to the magnetic field change and to the derivative of magnetization with respect to temperature at constant magnetic field; it is inversely proportional to the heat capacity.

5.3 Physical Model of Nanoscale Heat Communication

The NHC, which is proposed in this study for the first time in the literature, is a novel communication paradigm to realize wireless communication between nanodevices. The NHC model that is used in this study consists of a transmitter nanodevice (TN), a receiver nanodevice (RN), a thermal diffusion channel between TN and RN, and a noise caused by the stochastic fluctuations in the temperature at the output of the channel. In this section, we introduce the NHC model by describing how each of the components in the communication model works.

5.3.1 Transmitter

The transmitter nanodevice (TN) uses the binary bipolar encoding for the transmission of the binary information bits $\{a_j\}$. To transmit the information, the temperature of TN is modulated according to the bipolar encoded signal. That is, a binary bit 0 is transmitted by a zero temperature change and a binary bit 1 is transmitted alternately by a positive temperature change and a negative temperature change with the same magnitude. Therefore, the expected temperature change of the communication medium is zero. The communication takes place in a 3D medium having a significantly larger extent than the size of nanodevices. Furthermore, the communication medium can be solid, liquid, or gas.

The NHC with bipolar encoding is achieved by the utilization of the magnetocaloric effect (MCE) in TN. The MCE is used in the NHC since it can be successfully implemented to modulate the temperature at nanoscale. Fig. 5.2(a) shows the simplified model of TN. TN includes a CNT-based nanosolenoid, a thermal insulator shell, a spherical magnetic nanoparticle, a nanobattery, and a switch. The CNT-based nanosolenoid is used to create the desired magnetic field and change the temperature of the magnetic nanoparticle by means of the MCE. Since a copper nanosolenoid has a significantly large resistance and low quality factor due to nanoscale dimensions of copper wires, we use a CNT-based nanosolenoid in TN for the NHC. CNT-based nanosolenoids have extremely high conductivity and current carrying capabilities [88, 89]. Therefore, the Joule heating in the CNT-based

nanosolenoid is significantly lower compared with a copper nanosolenoid. Furthermore, we assume that the nanosolenoid is enclosed by a thermal insulator shell to prevent the Joule heating from interfering with the temperature signals transmitted by TN.

The information transmission process in the NHC is described as follows:

1. Initially, the switch is open and there is no current flowing through the nanosolenoid; thus, there is no magnetic field created by the nanosolenoid as shown in Fig. 5.2(a). The temperature of the magnetic nanoparticle is the same as the temperature of the medium, denoted by T , i.e., the system is in thermal equilibrium.
2. Then, if the next information bit to be transmitted is a binary bit 0, the switch remains open and the thermal equilibrium condition is sustained because the binary bit 0 is transmitted by a zero temperature change. However, if the next information bit to be transmitted is a binary bit 1, the switch is closed instantaneously which causes a current flow through the nanosolenoid; thus, a magnetic field H is created by the nanosolenoid as illustrated in Fig. 5.2(b). Since the magnetic field H is applied instantaneously to the magnetic nanoparticle, the process of the application of magnetic field can be approximated as an adiabatic process. Thus, the temperature of the nanoparticle increases by ΔT_{ad} due to the MCE. Then heat flows from the nanoparticle to the communication medium due to the temperature difference. For example, the temperature of Gd nanoparticles increase by 2K by applying a magnetic field having 500mT strength at room temperature [90]. With the advances in nanotechnology, CNT-based nanosolenoids having a magnetic core with high permeability can generate a magnetic field with a strength on the order of hundreds of mT [83]. Thus, the MCE can be conveniently used in the NHC to modulate the temperature of a magnetic nanoparticle.
3. In the NHC, the temperature of the magnetic nanoparticle is modulated according to the binary bipolar encoding; then, the expected value of the temperature change of the medium is zero. Furthermore, since the extent of the communication medium is

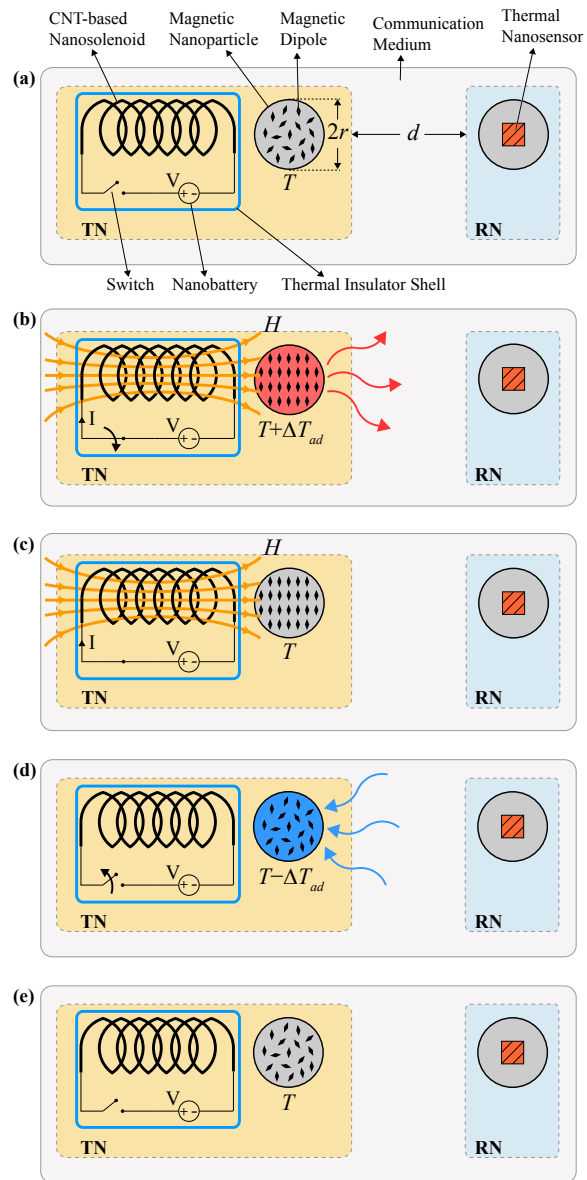


Figure 5.2: The NHC model and the temperature encoding mechanism with binary bipolar coding.

assumed to be significantly larger compared with the size of the magnetic nanoparticle, the heat capacity of the communication medium is also significantly larger than the heat capacity of the nanoparticle. For instance, 1L water at room temperature

$T = 300\text{K}$ has a heat capacity $C_V = 4140\text{J/K}$ and a nanoparticle has a heat capacity on the order of 10^{-18}J/K [100]. Thus, the steady state temperature change of the communication medium caused by the NHC is negligible compared with the temperature of the medium T and hence T can be assumed to be unchanged. Then, the magnetic nanoparticle returns its initial temperature T after the thermal equilibrium is reached as shown in Fig. 5.2(c).

4. After transmitting the binary bit 1, if the next information bit to be transmitted is a binary bit 0, the switch remains closed and the magnetic field H is held constant. However, if the next information bit to be transmitted is a binary bit 1, the switch is opened instantaneously, which cuts off the current flowing through the nanosolenoid; thus, the magnetic field H disappears as shown in Fig. 5.2(d). Since the magnetic field H that is applied to the magnetic nanoparticle instantaneously vanishes, the process of the removal of the magnetic field can be approximated as an adiabatic process. Hence, the temperature of the nanoparticle decreases by ΔT_{ad} due to the MCE. Then, heat flows from the communication medium to the nanoparticle because of the temperature difference.
5. The heat capacity of the communication medium is large enough that the temperature of the medium T is assumed to be unchanged (see item(c) above) and hence the temperature of the nanoparticle returns its initial value T after the thermal equilibrium is reached as shown in Fig. 5.2(e). That is, the system reaches its initial condition (see item (a) above). Therefore, the information transmission process continues from item (a) in a cyclic manner.

The inductance of the nanosolenoid opposes the rate of change of the current flowing through it when the switch in the TN is closed or opened. Therefore, when the switch is closed or opened instantaneously, the current flowing through the nanosolenoid exponentially increases or decreases, respectively, [101]. According to the transient analysis of the

TN circuit, the time constant of this exponential increase and decrease is given by

$$\tau = \frac{L}{R} \quad (5.4)$$

where R and L are the resistance and inductance of the nanosolenoid, respectively. When the switch is closed or opened, in order for the current to reach its steady state value, approximately 5τ time is required [101]. The adiabatic temperature change ΔT_{ad} of the magnetic nanoparticle described in Section 5.2 is proportional to the magnetic field H created by the solenoid, and the magnetic field is proportional to the current flowing through the nanosolenoid. Thus, when the switch is closed or opened, 5τ time passes for the magnetic field to reach its steady state value. Since a CNT-based nanosolenoid has an inductance on the order of 1nH and a resistance on the order of 10Ω [87], 5τ is on the order of 0.5ns which is an extremely short duration. Hence, during such an extremely short time, the heat transfer between the magnetic nanoparticle and the surroundings is negligible and the generation and removal process of the magnetic field can be assumed as an adiabatic process.

When the switch is closed instantaneously, the temperature of the magnetic nanoparticle adiabatically increases by ΔT_{ad} after 5τ time. At the end of the adiabatic process, the temperature of the magnetic nanoparticle changes according to the thermal diffusion. In other words, the initial condition for the temperature of the magnetic nanoparticle is $T + \Delta T_{ad}$ before the thermal diffusion takes place. Thus, the adiabatic temperature change can be modeled as an impulse function with a magnitude ΔT_{ad} . Furthermore, the radius of the spherical magnetic nanoparticle is considered negligible with respect to the distance between the TN and the RN; that is, $r \ll d$. Therefore, the magnetic nanoparticle is approximated as a point source emitting desired temperature signals at the location $(x = 0, y = 0, z = 0)$. Finally, the temperature variation of the magnetic nanoparticle is expressed as

$$s(x, y, z, t) = \Delta T_{ad} \delta(x, y, z, t). \quad (5.5)$$

According to the information transmission process described above, the total temperature variation of the nanoparticle located in TN is given by

$$s_T(x, y, z, t) = \sum_{j=-\infty}^{\infty} b_j s(x, y, z, t - jT_s) \quad (5.6)$$

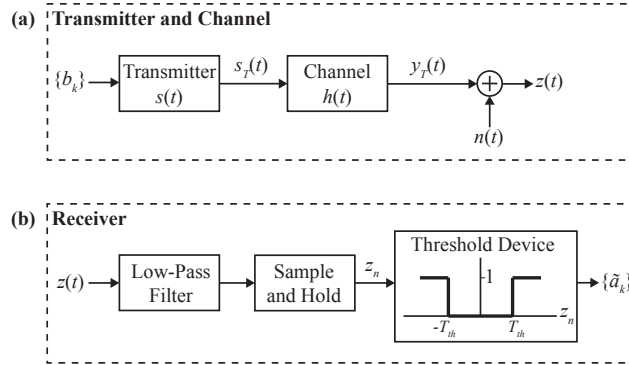


Figure 5.3: The block diagram representation of (a) transmitter and channel, and (b) receiver for the NHC model.

where $\{b_j\}$ is the bipolar encoded sequence of the binary information sequence $\{a_j\}$ and T_s is the signaling interval. The block diagram representation of the transmitter and channel can be seen in Fig. 5.3(a).

5.3.2 Signal Propagation

The transmission of the information from TN to RN is achieved by the propagation of the temperature signals transmitted by TN. The propagation of the temperature signals is caused by the thermal diffusion. To derive the impulse response of the thermal diffusion channel, we use the heat equation which describes the variation in temperature in a given region over time [102]. The heat equation is given by

$$\frac{\partial u(x, y, z, t)}{\partial t} = \alpha \nabla^2 u(x, y, z, t) \quad (5.7)$$

where $u(x, y, z, t)$ is the temperature of the point (x, y, z) at time t , $\nabla u(x, y, z, t)$ is the sum of the 3D spatial second derivatives of $u(x, y, z, t)$, and α is the thermal diffusivity of the medium assuming that the thermal diffusion takes place in a 3D medium. The impulse response of the thermal diffusion channel can be found by solving (5.7) for a point heat source with an initial condition for the temperature of the source

$$u(x, y, z, t = 0) = \delta(x, y, z). \quad (5.8)$$

The response of (5.7) to the impulse given in (5.8) yields the impulse response of the thermal diffusion channel, denoted by $h(t)$, and it is given as follows

$$h(t) = \frac{V}{(4\pi t\alpha)^{3/2}} \exp\left(-\frac{|d|^2}{4t\alpha}\right), \quad t > 0 \quad (5.9)$$

where V is the volume of the magnetic nanoparticle, i.e., $V = (4/3)\pi r^3$, $|d|$ is the Euclidean distance between RN and TN, i.e., $|d| = \sqrt{(x_R)^2 + (y_R)^2 + (z_R)^2}$, and (x_R, y_R, z_R) is the location of RN in 3D Cartesian coordinate system. To have a compact notation, we drop (x, y, z) term in $h(x, y, z, t)$ because TN and RN are located at fixed positions. Since the thermal diffusivity constant is assumed to be time-invariant, the NHC channel is time-invariant.

The temperature change at the RN location caused by the temperature variation of the magnetic nanoparticle can be obtained as

$$y(t) = s(t) * h(t) = \frac{\Delta T_{ad}V}{(4\pi t\alpha)^{3/2}} \exp\left(-\frac{|d|^2}{4t\alpha}\right), \quad t > 0 \quad (5.10)$$

where $*$ denotes the convolution operator. The total temperature change at RN location is

$$y_T(t) = \sum_{j=-\infty}^{\infty} b_j y(t - jT_s). \quad (5.11)$$

5.3.3 Noise

At the output of the thermal diffusion channel, a noise is added to the total temperature variation signal $y_T(x, t)$. The additive noise, denoted by $n(t)$, is a result of thermal fluctuations which are random deviations of a system from its equilibrium. The thermal fluctuations are generated by an additive Gaussian noise process with a power spectral density (PSD) given as

$$S_n(f) = \frac{k_B T^2}{C_V} \quad (5.12)$$

where T is the temperature of the communication medium, C_V is the heat capacity of the medium at constant volume, and k_B is Boltzmann constant [103]. Since in the NHC, the temperature of the magnetic nanoparticle is modulated according to the binary bipolar encoding, the expected value of the temperature change of the medium is zero. Furthermore,

since the heat capacity of the communication medium is assumed to be significantly larger than the heat capacity of the magnetic nanoparticle, the steady state temperature change of the medium is considered as negligibly small compared with the temperature of the medium T . For example, 1L water at room temperature $T = 300\text{K}$ has a heat capacity $C_V = 4140\text{J/K}$ and a nanoparticle has a heat capacity on the order of 10^{-18}J/K [103]. Therefore, the temperature of the medium T and the PSD of the noise are assumed to be constant. Consequently, based on the aforementioned assumptions, the additive noise in the NHC can be modeled as an additive white Gaussian noise (AWGN) with a PSD in (5.12).

5.3.4 Receiver

The receiver nanodevice (RN) is located at a distance of d from TN and the total instantaneous temperature variation at the receiver location is given by

$$z(t) = y_T(t) + n(t). \quad (5.13)$$

RN includes a thermal nanosensor in order to detect the temperature signals transmitted by TN. The temperature sensor converts the temperature signals to electrical signals. To increase the signal-to-noise ratio (SNR) of the received electrical signals, the power of the noise is limited by a low pass filter (LPF) with unity gain before sampling the temperature. The bandwidth of the LPF, denoted by B , is chosen to be $B \geq 2/T_s$ so that the bipolar signaling wave shape is preserved at the filter output, yet the noise power is reduced by the filter [104]. It is assumed that RN samples the output of the LPF with a sampling time T_s which is equal to the signaling interval of TN. Thus, assuming the detection is coherent and there is no intersymbol interference (ISI), the signal of the temperature variation sampled by RN is given as

$$z_k = \Delta T_{max} b_k + n_k \quad (5.14)$$

where $z_k = z(kT_s)$, $n_k = n(kT_s)$, and ΔT_{max} is defined as the maximum temperature change at the receiver location and it is given by

$$\Delta T_{max} = \max_t y(t) = \frac{\Delta T_{ad} V}{(\frac{2}{3} \pi e d^2)^{3/2}}. \quad (5.15)$$

The delay required for the temperature of the reception space reaches its maximum value, denoted by t_{max} , is given as

$$t_{max} = \arg \max_t y(t) = \frac{d^2}{6\alpha}. \quad (5.16)$$

The output of the sample and hold device is passed through a threshold device. The output of the threshold device gives the detected bits that are transmitted by TN. If $|z_n| > T_{th}$, the output of the threshold device is 1, otherwise 0 where T_{th} is the threshold temperature. To have a negligible ISI, the sampling time T_s should be large enough, i.e., $T_s \gg t_{max}$. The block diagram representation of the receiver can be seen in Fig. 5.3(b).

5.4 An Information Theoretical Analysis of Nanoscale Heat Communication

In this section, we present an information theoretical analysis of the NHC. According to the communication model described above, the NHC channel is a time-invariant additive white Gaussian noise (AWGN) channel and the binary bipolar signaling is used for the information transmission. In order to characterize the channel of the NHC, first, we derive the information transmission probabilities of the channel.

Since the channel noise is AWGN, it is a zero-mean wide-sense stationary Gaussian process. We know that for a Gaussian process at the input, the output of the linear processor is also a Gaussian process. Therefore, the noise sample at the output of the sampler device is a zero mean Gaussian random variable and the total output sample z_n is a Gaussian random variable whose mean value depends on the transmitted bipolar information bit b_n as in (5.14). That is, $\{z_n | +1 \text{ sent}\} \sim \mathcal{N}(\Delta T_{max}, \sigma_0^2)$, $\{z_n | -1 \text{ sent}\} \sim \mathcal{N}(-\Delta T_{max}, \sigma_0^2)$, $\{z_n | 0 \text{ sent}\} \sim \mathcal{N}(0, \sigma_0^2)$ where σ_0^2 is the variance of the noise samples and it is equal to the average received noise power, denoted by \bar{P}_n , i.e., $\sigma_0^2 = \bar{P}_n$. The power of the noise is limited by the low-pass filter (LPF) before sampling the temperature; hence, the average received noise power \bar{P}_n is given by

$$\bar{P}_n = \int_{-B}^B S_n(f) df = \frac{2Bk_B T^2}{C_V}. \quad (5.17)$$

If the threshold of the threshold device is $T_{th} = \Delta T_{max}/2$, then the probability of erroneous

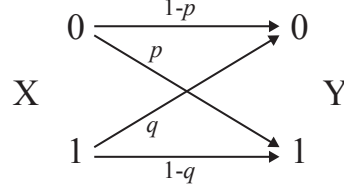


Figure 5.4: The binary asymmetric channel (BAC) representation for the NHC.

transmission of bit 1 is given by

$$\begin{aligned}
 q &= \frac{1}{2} \Pr(0 \text{ received} | +1 \text{ sent}) + \frac{1}{2} \Pr(0 \text{ received} | -1 \text{ sent}) \\
 &= Q \left(\sqrt{\frac{\Delta T_{max}^2}{4\bar{P}_n}} \right) = Q \left(\sqrt{\frac{\Delta T_{max}^2 C_V}{8k_B B T^2}} \right)
 \end{aligned} \tag{5.18}$$

where $Q(\cdot)$ is the Q-function. The probability of erroneous transmission of bit 0 is given by

$$p = \Pr(1 \text{ received} | 0 \text{ sent}) = 2Q \left(\sqrt{\frac{\Delta T_{max}^2}{4\bar{P}_n}} \right) = 2Q \left(\sqrt{\frac{\Delta T_{max}^2 C_V}{8k_B B T^2}} \right). \tag{5.19}$$

Since $p \neq q$, the NHC channel exhibits binary asymmetric channel (BAC) characteristics. The BAC channel model of the NHC is illustrated in Fig. 5.4 based on the analysis that we introduced so far.

Assume that X is the transmitted bit by TN and Y is the received bit by RN. Then, we assume that TN transmits bit 1 with a probability P_T , i.e.,

$$P_X(x) = \begin{cases} P_T, & \text{if } x = 1 \\ 1 - P_T, & \text{if } x = 0. \end{cases} \tag{5.20}$$

Using (5.20) and the channel transmission probabilities seen in Fig. 5.4, the joint probability distribution of X and Y , denoted by $P_{XY}(x, y)$, is given as

$$P_{XY}(x, y) = \begin{cases} (1-p)(1-P_T), & \text{if } (x=0, y=0) \\ p(1-P_T), & \text{if } (x=0, y=1) \\ qP_T, & \text{if } (x=1, y=0) \\ (1-q)P_T, & \text{if } (x=1, y=1). \end{cases} \tag{5.21}$$

The joint distribution $P_{XY}(x, y)$ expresses the probability of that the observed output symbol is y and the transmitted symbol is x . The mutual information between X and Y denoted by $I(X; Y)$ is given in [38] as follows

$$I(X; Y) = \sum_{x, y} P_{XY}(x, y) \log_2 \frac{P_{XY}(x, y)}{P_X(x)P_Y(y)} \quad (5.22)$$

where $P_Y(y)$ is the probability distribution of Y . It is straightforward to obtain $P_Y(y)$ using the joint distribution $P_{XY}(x, y)$. The NHC channel capacity, denoted by C , is the maximum value of the mutual information [38] and the channel capacity C is found as follows

$$C = \max_{P(x)} I(X; Y) = \frac{(1-p)H(q) - qH(1-p)}{q+p-1} + \log_2 \left(1 + 2 \frac{H(1-p) - H(q)}{q+p-1} \right) \quad (5.23)$$

where $H(\cdot)$ is the binary entropy function defined as

$$H(q) = -q \log_2 q - (1-q) \log_2 (1-q). \quad (5.24)$$

Furthermore, the operational channel capacity in bits/sec (bps) is given as

$$C_{op} = \frac{C}{T_s} \quad (5.25)$$

where T_s is the signaling time of the NHC.

In order to derive an expression for the average received signal power, we start with the general expression for the PSD of the digital signal in (5.11), which is given in [104] as

$$S_y(f) = \frac{|Y(f)|^2}{T_s} \sum_{k=-\infty}^{\infty} R_k e^{j2\pi f k T_s} \quad (5.26)$$

where R_k is the autocorrelation function of the bipolar encoded data, which is given as

$$R_k = \mathbb{E}[b_j b_{j+k}] \quad (5.27)$$

and $Y(f)$ is the Fourier Transform of $y(t)$ given by

$$Y(f) = \frac{\Delta T_{ad} V \exp\left(-d\sqrt{\frac{\pi|f|}{\alpha}}\right)}{4\alpha\pi d|f|} \left[|f| \cos\left(d\sqrt{\frac{\pi|f|}{\alpha}}\right) - jf \sin\left(d\sqrt{\frac{\pi|f|}{\alpha}}\right) \right] \quad (5.28)$$

To simplify the mathematical analysis, we consider a transmitted binary information sequence $\{a_k\}$ in which 0's and 1's are equally likely, i.e., $\Pr(a_k = 0) = \Pr(b_k = 0) = 1/2$ and $\Pr(a_k = 1) = \Pr(b_k = \pm 1) = 1/2$. Therefore, the autocorrelation function for the bipolar encoded data is simply given by

$$R_k = \begin{cases} 1/2, & k = 0 \\ -1/4, & |k| = 1 \\ 0, & |k| \geq 2. \end{cases} \quad (5.29)$$

Then, the summation term in (5.26) becomes

$$\sum_{k=-\infty}^{\infty} R_k e^{j2\pi f k T_s} = \frac{1}{2} - \frac{1}{4} e^{j2\pi f T_s} - \frac{1}{4} e^{-j2\pi f T_s} = \frac{1}{2} - \frac{1}{2} \cos 2\pi f T_s = \sin^2(\pi f T_s). \quad (5.30)$$

Since the received signal is passed through the LPF, the average received signal power, denoted by \bar{P}_s , is given by

$$\bar{P}_s = \int_{-B}^B S_y(f) df = \frac{\Delta T_{ad}^2 V^2}{16 T_s \alpha^2 d^2 \pi^2} \int_{-B}^B \exp\left(-2d^2 \sqrt{\frac{\pi|f|}{\alpha}}\right) \sin^2(\pi f T_s) df. \quad (5.31)$$

The average received noise power \bar{P}_n is given in (5.17). Therefore, the received signal-to-noise ratio (SNR) for the NHC is found as follows

$$\text{SNR} = \frac{\bar{P}_s}{\bar{P}_n} = \frac{\Delta T_{ad}^2 V^2 C_V}{32 k_B \pi^2 B T_s \alpha^2 d^2 T^2} \int_{-B}^B \exp\left(-2d^2 \sqrt{\frac{\pi|f|}{\alpha}}\right) \sin^2(\pi f T_s) df. \quad (5.32)$$

5.5 Performance Evaluation

In this section, we present the performance analysis of the signal-to-noise ratio (SNR) in (5.32) and the channel capacity in (5.23) and (5.25). In the numerical analyses, we show how the SNR and channel capacity of the NHC vary according to several parameters namely the adiabatic temperature change, the thermal diffusivity constant, and the distance between TN and RN. The results of the numerical analyses are used to determine the appropriate configuration of the NHC parameters to achieve high channel capacity.

The analyses are carried out with a single TN and a single RN configuration as described in Section 5.3. For the analysis, the radius of the magnetic nanoparticle is $r = 5\text{nm}$ which

is a typical nanoparticle radius size [105]. Since $T_s \gg t_{max}$ condition should be satisfied to have a negligible ISI, we assume $T_s = 10t_{max}$. As we state in Section 5.3, if $B \geq 2/T_s$ condition is fulfilled, the received signal shape at the output of the low-pass filter (LPF) is not distorted. Then, we set $B = 2/T_s$. The Boltzmann constant is $k_B = 1.38 \times 10^{-23}$ J/K. The communication is assumed to take place at room temperature, i.e., $T = 300$ K. Since nanodevices can be used in many different environments and the NHC can take place in all three state of the matter, the communication medium for the NHC depend on the application for which nanodevices are used. For the numerical analyses, we consider the communication medium as water with 1L volume. The constant volume molar heat capacity of water at 300K is 74.53J/mol·K [100]. Thus, since the molar mass of water is 18g, the heat capacity of the medium is found as $C_V = 74.53 \cdot (1000\text{g}/18\text{g})\text{J/K} = 4.14 \times 10^3$ J/K. The thermal diffusivity of the water at 300K is $\alpha = 1.43 \times 10^{-7}$ m²/s [106]. The numerical analyses are performed using MATLAB.

5.5.1 Effect of Communication Distance

In the first analysis, we investigate the effect of the communication distance d on the SNR and the channel capacity of the NHC. In this part of the analysis, the adiabatic temperature change and the thermal diffusivity constant are kept unchanged at $\Delta T_{ad} = 2$ K and $\alpha = 1.43 \times 10^{-7}$ m²/s, respectively. The SNR variation with respect to the communication distance d is illustrated in Fig. 5.5(a). The SNR decreases with an increase in d because as the communication distance increases, the received power of the temperature signal \bar{P}_s decreases, which can be seen in (5.31). For example, SNR = 107.7dB at $d = 100$ nm and SNR = -21.1dB at $d = 2.5\mu\text{m}$.

In Fig. 5.6(a), the variation of the channel capacity C in bit/use with respect to the communication distance d is shown. For short communication distances, since the SNR is too high as seen in Fig. 5.5(a), the effect of the noise on the information transmission is negligible; that is, the erroneous transmission probabilities p and q are too small. For instance, for a communication distance $d < 1.0\mu\text{m}$, the SNR > 15 dB and the channel capacity has its maximum value $C = 1.0$ bit/use. On the other hand, for long communication

distances, since the SNR decreases and becomes negative, the effect of the noise turns out significant and reduces the channel capacity. For example, for $d > 1.0\mu\text{m}$, C decreases and becomes $C = 0.03\text{bit/use}$ at $d = 2.5\mu\text{m}$ as shown in Fig. 5.6(a).

The channel capacity $C_{op} = C/T_s$ in bps changes with respect to the communication distance d as shown in Fig. 5.7(a). Note that, the variations of the channel capacity in bit/use and bps with respect to d are different because substituting $T_s = 10t_{max}$ and (5.16) in (5.25) yields $C_{op} = 0.6\alpha C/d^2$. Thus, the channel capacity C_{op} in bps decreases with an increase in d as seen in Fig. 5.7(a), although the channel capacity in bit/use is constant and $C = 1.0\text{bit/use}$ for $d < 1.0\mu\text{m}$. For $d > 1.0\mu\text{m}$, C in bit/use also decreases as d increases, which causes the C_{op} in bps to decrease faster with respect to d . For example, the channel capacity is $C_{op} = 8.58\text{Mbps}$ at $d = 100\text{nm}$ and it becomes $C_{op} = 0.37\text{kbps}$ at $d = 2.5\mu\text{m}$. Therefore, we can say that the NHC can provide very high communication rates over a long communication range compared with existing nanoscale communication techniques in the literature.

5.5.2 Effect of Adiabatic Temperature Change

In this analysis, we investigate the effect of the adiabatic temperature change ΔT_{ad} on the SNR and the channel capacity. The communication distance and the thermal diffusivity constant are kept unchanged at $d = 500\text{nm}$ and $\alpha = 1.43 \times 10^{-7}\text{m}^2/\text{s}$, respectively, during this part of the analysis. The SNR variation with respect to the adiabatic temperature change ΔT_{ad} is demonstrated in Fig. 5.5(b). The SNR increases with an increase in ΔT_{ad} , which is an expected result because as ΔT_{ad} increases, the received power of the temperature signal \bar{P}_s increases as seen in (5.31). For example, $\text{SNR} = -16.6\text{dB}$ for $\Delta T_{ad} = 0.1\text{K}$ and $\text{SNR} = 43.3\text{dB}$ for $\Delta T_{ad} = 2.0\text{K}$.

The channel capacity C in bit/use with respect to the adiabatic temperature change ΔT_{ad} is shown in Fig. 5.6(b). For a small adiabatic temperature change, since the SNR is too low as seen in Fig. 5.5(b), the effect of the noise on the information transmission is significant which makes the channel capacity to become too low. For example, for a adiabatic temperature change $\Delta T_{ad} = 0.1\text{K}$, the channel capacity is $C = 0.08\text{bit/use}$. On

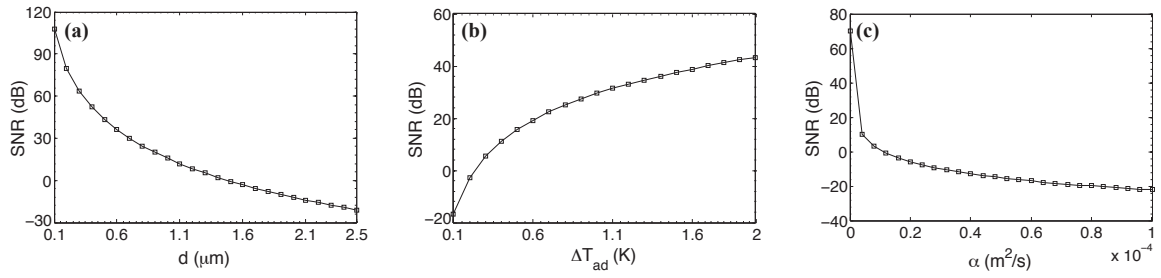


Figure 5.5: The numerical analysis results performed over the SNR in dB with respect to the (a) communication distance d , (b) adiabatic temperature change ΔT_{ad} , and (c) thermal diffusivity constant α .

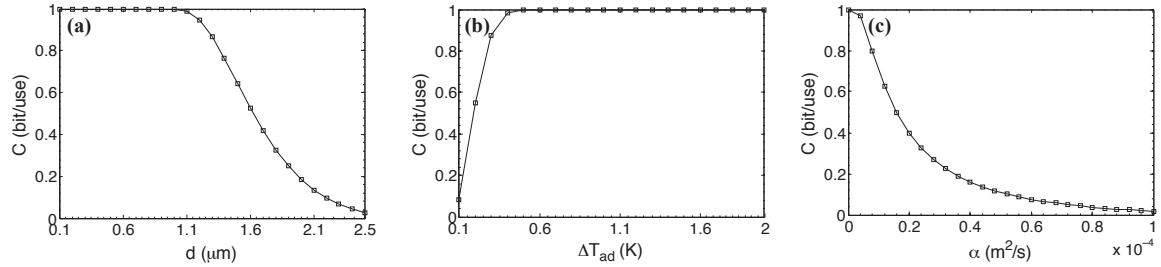


Figure 5.6: The numerical analysis results performed over the channel capacity C in bit/use with respect to (a) the communication distance d , (b) the adiabatic temperature change ΔT_{ad} , (c) the thermal diffusivity constant α .

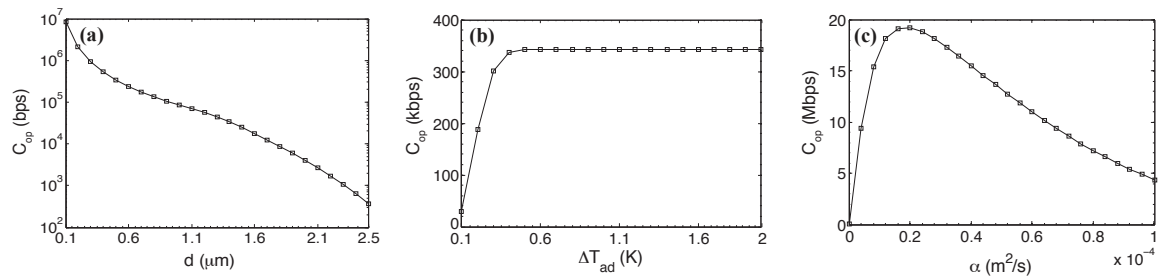


Figure 5.7: The numerical analysis results performed over the channel capacity C_{op} in bps with respect to (a) the communication distance d , (b) the adiabatic temperature change ΔT_{ad} , (c) the thermal diffusivity constant α .

the other hand, for a large adiabatic temperature change, since the SNR is high, the effect of the noise on the information transmission is negligible; that is, the erroneous transmission

probabilities p and q are too small. For instance, for $\Delta T_{ad} > 0.5\text{K}$, the $\text{SNR} > 15\text{dB}$ and the channel capacity C in bit/use has its maximum value $C = 1.0\text{bit/use}$ as shown in Fig. 5.6(b).

The channel capacity C_{op} in bps changes with respect to the adiabatic temperature change ΔT_{ad} as shown in Fig. 5.7(b). Note that, since the signalling time T_s does not depend on ΔT_{ad} , the variations of the channel capacity in bit/use and bps with respect to ΔT_{ad} are the same. That is, for an adiabatic temperature change $\Delta T_{ad} = 0.1\text{K}$, the channel capacity is $C_{op} = 28.9\text{kbps}$ and for an adiabatic temperature change $\Delta T_{ad} > 0.5\text{K}$, the channel capacity saturates and becomes $C_{op} = 343.2\text{kbps}$ as illustrated in Fig. 5.7(b). Therefore, the channel capacity can be increased by increasing the adiabatic temperature change. However, since the channel capacity saturates as ΔT_{ad} increases, to minimize the effect of the temperature signals on the communication medium, the smallest ΔT_{ad} providing $C = 1.0\text{bit/use}$ can be used. According to the results, the NHC can provide very high communication rates with very low adiabatic temperature changes.

5.5.3 Effect of Thermal Diffusivity Constant

In the last analysis, we investigate the effect of the thermal diffusivity constant α of the communication medium on the SNR and the channel capacity of the NHC. For this part of the analysis, the communication distance and the adiabatic temperature change are kept unchanged at $d = 500\text{nm}$ and $\Delta T_{ad} = 2\text{K}$, respectively. The SNR variation with respect to the thermal diffusivity constant α is shown in Fig. 5.5(c). The SNR decreases with an increase in α . This is an expected result because as the thermal diffusivity constant increases, the average received power of the temperature signal \bar{P}_s decreases, which can be seen in (5.31). Furthermore, substituting $T_s = 10t_{max}$, $B = 2/T_s$, and (5.16) in (5.17) yields $\bar{P}_n = 2.4\alpha k_B T^2 d^{-2} C_V^{-1}$. Therefore, increasing α also increases the average received noise power \bar{P}_n . In addition, the SNR decreases abruptly when α is increased from $10^{-8}\text{m}^2/\text{s}$ to $4 \times 10^{-6}\text{m}^2/\text{s}$; then, it decreases slowly. For instance, $\text{SNR} = 69.9\text{dB}$ for $\alpha = 10^{-8}\text{m}^2/\text{s}$ and $\text{SNR} = -22.2\text{dB}$ for $\alpha = 10^{-4}\text{m}^2/\text{s}$.

The channel capacity C in bit/use with respect to α is shown in Fig. 5.6(c). For

low thermal diffusivity constants, since the SNR is too high as seen in Fig. 5.5(c), the effect of the noise on the information transmission is negligible; that is, the erroneous transmission probabilities p and q are too small. For example, for a thermal diffusivity constant $\alpha < 4 \times 10^{-6} \text{m}^2/\text{s}$, the SNR $> 10\text{dB}$ and the channel capacity is very high, i.e., $C > 0.97\text{bit/use}$. On the other hand, for a high thermal diffusivity constant, since the SNR is very low, the effect of the noise becomes significant and reduces the channel capacity. For instance, $C = 1.0\text{bit/use}$ for $\alpha = 10^{-8}\text{m}^2/\text{s}$ and $C = 0.02\text{bit/use}$ for $\alpha = 10^{-4}\text{m}^2/\text{s}$ as seen in Fig. 5.6(c).

The channel capacity C_{op} in bps changes with respect to the thermal diffusivity constant α as shown in Fig. 5.7(c). Note that, the variations of the channel capacity in bit/use and bps with respect to d are different because $C_{op} = 0.6\alpha C/d^2$ as found in Section V-A; that is C_{op} depends on α . Since C also depends on α , the effect of the α on C_{op} is not straightforward. The results show that increasing α from $10^{-8}\text{m}^2/\text{s}$ to $2 \times 10^{-5}\text{m}^2/\text{s}$ increases the channel capacity C_{op} from 24.4kbps to 19.2Mbps. However, further increasing α decreases C_{op} because C becomes too low for high α values and its effect on C_{op} becomes significant. For instance, increasing α from $2 \times 10^{-5}\text{m}^2/\text{s}$ to $10^{-4}\text{m}^2/\text{s}$ decreases C_{op} from 19.2Mbps to 4.4Mbps.

According to the results, we can say that the channel capacity of the NHC can reach very high communication rates by selecting a communication medium having an appropriate thermal diffusivity constant. For example, the channel capacity is $C_{op} = 0.34\text{Mbps}$ for water at 300K whose thermal diffusivity constant is $\alpha = 1.43 \times 10^{-7}\text{m}^2/\text{s}$, and the channel capacity is $C_{op} = 19.2\text{Mbps}$ for air at 300K whose thermal diffusivity constant is $\alpha = 1.9 \times 10^{-5}\text{m}^2/\text{s}$.

Chapter 6

CONCLUSIONS AND FUTURE RESEARCH DIRECTIONS

In this thesis, design and analysis of several nanoscale communication techniques are performed for realization of a reliable and efficient communication between nanodevices. The following four topics have been investigated under this research and each of them is described in the following sections:

1. Nanoscale Molecular Gap Junction Communication Channel
2. Receiver Design for Molecular Communication
3. Nanoscale Magneto-Inductive Communication Channel
4. Nanoscale Heat Communication Channel

6.1 Research Contributions

In this section, we summarize the contributions of each chapter and underline the important results.

6.1.1 Nanoscale Molecular Gap Junction Communication Channel

In this study, we model the GJ communication channel between cardiomyocytes from the information theoretical perspective for the first time in the literature. Firstly, we introduce the AP propagation model between TC and RC and point out the conditions for the success and the failure of the AP propagation. Afterwards, we describe the stochastic GJ channel model. Then, as a result of the information theoretical analysis, we derive a closed-form expression for the capacity of the GJ communication channel between TC and RC. Finally,

the capacity of the GJ communication channel is analyzed numerically by using the capacity expression for different physiological parameters namely the number of the GJ channels, the cell length, the cell radius, the membrane resistivity, and the free calcium concentration. The results of the numerical analysis of the GJ communication channel capacity and the propagation delay show that a decrease in the channel capacity and an increase in the propagation delay are highly correlated to several cardiac diseases such as spontaneous ventricular arrhythmia and ischemic cardiomyopathy. It is also observed that very high or very low information transmission rates cause cardiac arrhythmias. Consequently, the model of the communication channel between cardiomyocytes presented in this thesis can be used to get new insights into reasons of the cardiac diseases and hence diagnose and treat these diseases with the advances in nanomedicine. Furthermore, the numerical results reveal that the capacity of the GJ communication designed for nanodevices can be improved using the GJ communication model presented in this study.

6.1.2 Receiver Design for Molecular Communication

In the MC, high signaling rates causes ISI because of the infinite duration impulse response of the diffusion-based molecular channel. In addition, the MC suffers from a signal-dependent noise at the receiver. For the first time in the literature, four signal detection methods for nanodevices communicating via diffusion-based molecular communication channel are proposed in this thesis. We present the sequence detection methods based on MAP and ML criteria, the MMSE equalizer, and the MMSE-DFE to mitigate both the ISI and noise in the MC. Firstly, the diffusion-based molecular channel is described, the impulse response of the channel is obtained. Then, the nonstationary particle counting noise is incorporated to the model to design the detection methods properly. Succeeding that we present the MAP and ML sequence detection methods and derive branch metrics of the trellis search in the Viterbi algorithm. Next, a linear equalizer based on MMSE criterion is introduced. Then, a nonlinear type equalizer, MMSE-DFE, is presented. To improve the performance of the MMSE-DFE, we propose a decision device based on ML detection method at the output of the MMSE-DFE.

According to the simulation results, while the best performance is achieved by the ML sequence detector which is the most complex detector, the MMSE equalizer has the worst performance which is the most simple detector. The performance of the MMSE-DFE stands between MMSE equalizer and ML sequence detector. Furthermore, the usage of a decision device instead of a simple quantizer increases the performance of the MMSE-DFE. A detector can be selected based on the required reliability of the communication and the feasible complexity of the detector at nanoscale. Moreover, since the diffusion-based molecular channel is time varying, we propose using a channel estimator at RN. Our results reveal that in MC, very high information transmission rates can be achieved with very low bit error rates by using the detection methods presented above. Thus, the detection methods obtained in this thesis significantly improves the communication capabilities of nanodevices.

6.1.3 Nanoscale Magneto-Inductive Communication Channel

In this thesis, we propose a novel nanoscale wireless communication technique, i.e., the WNMI communication which relies on the magnetic coupling between the CNT bundle-based nanocoils. We present the realistic physical communication models for both the point-to-point and waveguide-based WNMI communication methods. Then, we derive the analytical expressions for the path loss in these WNMI communication methods. Afterwards, we analyze both the point-to-point and waveguide-based WNMI communication techniques from an information theoretical perspective to find their channel capacities.

The numerical performance analyses of the path loss show that using the waveguide structure in the WNMI communication significantly improves the feasible communication range by greatly reducing the path loss. Furthermore, the channel capacity of the waveguide-based WNMI communication is considerably higher than that of the point-to-point WNMI communication. The results of the numerical analyses also reveal that the channel capacity of the WNMI communication methods can be significantly increased by appropriately adjusting the permeability of the magnetic core in the nanocoils, the physical dimensions of the nanocoils, and the distance between relay nanonodes in the waveguide.

The WNMI communication stands as a promising alternative communication technique

for wireless communication at nanoscale. First, the novel WNMI communication overcomes the problems encountered in the nanoscale wireless EM communication by introducing low absorption losses and flat channel characteristics. Second, although the path loss might be more severe in the WNMI communication than in the nanoscale EM communication, using the waveguide technique solves the high path loss problem in the WNMI communication. Last, the numerical results show that the channel capacity of the WNMI communication methods can reach very high values, which allows very high transmission bit-rates at nanoscale.

6.1.4 Nanoscale Heat Communication Channel

In this thesis for the first time in the literature, we propose the NHC technique in which the heat transfer is used for the transmission of information at the nanoscale. In the NHC, the information is encoded using a well-known phenomenon, MCE, which is the variation in temperature of magnetic materials exposed to a changing magnetic field. Recently, the MCE has been used in experimental cancer treatments called magnetic hyperthermia in which the magnetic nanoparticles placed in a tumor are exposed to a varying magnetic field, which heats up the nanoparticles and kills the tumor. The NHC can be utilized for the magnetic hyperthermia. For instance, nanodevices communicating with the NHC can perform complex tasks such as diagnosis of cancer and precise detection of tumors. Afterwards, the magnetic nanoparticles, which are initially employed for the NHC, can be used by nanodevices to kill the detected tumors using the magnetic hyperthermia in a coordinated way.

The NHC method has several advantages over MC even though both of the methods are based on the diffusion. First, in the NHC, it is possible to overcome the energy bottleneck of nanonetworks and to make their lifetime infinite by using, for example, a piezoelectric nanogenerator. Second, in the NHC, since the binary bipolar encoding is used, the expected temperature variation of the communication environment due to the NHC is zero. Third, the NHC can be utilized in all three states of the matter, which expands the application area of nanodevices communicating with the NHC. Last, the implementation of the NHC

is simple. That is, a nanodevice can become a transmitter by incorporating a nanosolenoid and a magnetic nanoparticle into the nanodevice. Similarly, a nanodevice can receive the transmitted temperature signals only by a thermal nanosensor.

We present a realistic physical communication model for the NHC between a single transmitter-receiver pair by describing how the transmitter, channel, and receiver in the NHC model works. Then, we analyze the NHC channel from an information theoretical perspective to obtain the closed-form expressions for the channel capacity and SNR. The numerical results show that the channel capacity performance of the NHC can reach very high rates over a long communication range compared with existing nanocommunication methods in the literature. Furthermore, according to the results, the amplitude of the temperature signals does not need to be very high. Therefore, the NHC is compatible to be used inside a living organism without harming living cells in the communication environment. Moreover, the channel capacity can be increased significantly by selecting a communication medium having an appropriate thermal diffusivity constant. As a result, the NHC stands as a promising solution to nanoscale communication between nanomachines based on its channel capacity performance, advantages, and possible applications for emerging nanonetworks.

6.2 Future Research Directions

Investigation of GJ communication channel between cardiomyocytes from an information theoretical perspective, and providing relations between GJ communication parameters and cardiac diseases broadens the contributions of this study and can promote the development of nanomedicine field. Therefore, this study provide a background for developing new diagnosis and treatment strategies for cardiac diseases in nanomedicine, which opens a novel research area. Furthremore, our ongoing works aim to investigate the GJ communication for multiple cells in a 2D and 3D network of cardiomyocytes.

The performance analyses of our receiver designs for diffusion-based molecular communication show that using appropriate receivers significantly increases data rates in molecular communication. Thus, for future implementation of molecular communication systems, our

pioneering study constitutes a significant background information.

In this thesis, we present two novel and physically realizable nanoscale communication methods namely WNMI communication and NHC. The performance analyses indicate that these nanoscale communication methods have significantly high communication capabilities. Thus, both methods stand as promising solutions to nanoscale wireless communication between nanodevices based on their channel capacity performances, advantages, and possible applications for emerging nanonetworks. The models of these novel nanoscale communication techniques could be experimentally validated and utilized for future nanonetwork frameworks.

REFERENCES

- [1] S. Hiyama, Y. Moritani, T. Suda, R. Egashira, A. Enomoto, M. Moore and T. Nakano, "Molecular Communication," in *Proc. of NSTI Nanotech. 2005*, Anaheim, California, USA, 2005.
- [2] M. Gregori, I. F. Akyildiz, "A new nanonetwork architecture using flagellated bacteria and catalytic nanomotors," *IEEE JSAC*, vol. 28, no. 4, pp. 612-619, 2010.
- [3] B. Atakan, S. Balasubramaniam, O. B. Akan, "Body Area NanoNetworks with Molecular Communications in Nanomedicine," *IEEE Com. Mag.*, vol. 50, no. 1, pp. 28-34, January 2012.
- [4] I. F. Akyildiz, F. Brunetti, C. Blazquez, "Nanonetworks: A new communication paradigm," *Computer Networks (Elsevier)*, vol. 52, no. 12, pp. 2260-2279, 2008.
- [5] R. A. Freitas, "Nanomedicine, Vol. I: Basic Capabilities," Landes Bioscience, 1999.
- [6] L. P. Giné and I. F. Akyildiz, "Molecular communication options for long range nanonetworks," *Computer Networks (Elsevier)*, vol. 53, no. 16, pp. 2753-2766, Nov 2009.
- [7] M. Pierobon, I. F. Akyildiz, "A Physical End-to-End Model for Molecular Communication in Nanonetworks," *IEEE JSAC*, vol. 28, no. 4, pp. 602-611, May 2010.
- [8] M. Pierobon, I. F. Akyildiz, "Diffusion-based Noise Analysis for Molecular Communication in Nanonetworks," *IEEE Transactions on Signal Processing*, vol. 59, no. 6, pp. 2532-547, June 2011.

-
- [9] M. Kuscü, O. B. Akan, "A Physical Channel Model and Analysis for Nanoscale Molecular Communications with Förster Resonance Energy Transfer (FRET)," *IEEE Transactions on Nanotechnology*, vol. 11, no:1, pp 200-207, 2012.
- [10] B. J. MacLennan, "Morphogenesis as a model for nano communication," *Nano Communication Networks*, vol. 1, no. 3, pp. 199-208, 2010.
- [11] M. Pierobon, I. F. Akyildiz, "Information Capacity of Diffusion-based Molecular Communication in Nanonetworks," in *Proc. of IEEE Int. Conf. on Comp. Comm, INFOCOM, Miniconf.*, China, April 2011.
- [12] A. Eckford, "Nanoscale communication with brownian motion," in *Proc. 41st Annu. Conf. Inf. Sci. Syst.*, 2007, pp. 160-165.
- [13] P. J. Thomas *et al.*, "The diffusion mediated biochemical signal relay channel," in *Proc. 17th Annu. Conf. Neural Inf. Process. Syst.*, 2003.
- [14] B. Atakan, O. B. Akan, "An information theoretical approach for molecular communication," in *Proc. 2nd Int. Conf. Bio-Inspired Models Netw., Inf., Comput. Syst.*, 2007, pp. 33-40.
- [15] B. Atakan, O. B. Akan, "On molecular multiple-access, broadcast, and relay channels in nanonetworks," in *Proc. 3rd Int. Conf. Bio-Inspired Models Netw., Inf., Comput. Syst.*, 2008, Art. no. 16.
- [16] T. Nakano, J. Q. Liu, "Design and analysis of molecular relay channels: An information theoretic approach," *IEEE Transactions on Nanobioscience*, vol. 9, no. 3, pp. 213-221, Jun 2009.
- [17] D. Kilinc, O. B. Akan, "An Information Theoretical Analysis of Nanoscale Molecular Gap Junction Communication Channel Between Cardiomyocytes," *IEEE Transactions on Nanotechnology*, vol.12, no.2, pp.129-136, March 2013.

-
- [18] N. M. Kumar, N. B. Gilula, "The gap junction communication channel," *Cell*, vol. 84, pp. 381-388, 1996.
- [19] T. Nakano et al., "Molecular Communication through Gap Junction Channels," *Springer Transactions on Computational Systems Biology X*, vol. 5410, pp. 81-99, 2008.
- [20] T. Nakano et al., "Molecular communication for nanomachines using intercellular calcium signaling," in *Proc. of the 5th IEEE Conf. on Nanotechnology*, vol. 2, pp. 478-481, Nagoya, Japan, 2005.
- [21] H. Niessen et al., "Selective permeability of different connexin channels to the second messenger inositol 1,4,5-triphosphate," *J. Cell Sci.*, vol. 113, pp. 1365-1372, 2000.
- [22] G. Sohl, K. Willecke, "Gap junctions and the connexin protein family," *Cardiovasc. Res.*, vol. 62, pp. 228-232, 2004.
- [23] D. A. Jaye, Y. Xiao, D. C. Sigg, "Basic Cardiac Electrophysiology: Excitable Membranes," in *Cardiac Electrophysiology Methods and Models*, D. C. Sigg, P. A. Iaizzo, Y. Xiao, B. He, Ed. Springer, 2010, pp. 41-51.
- [24] A. P. de Carvalho, B. F. Hoffman, M. de P. Carvalho, "Two components of the cardiac action potential. I. Voltage-time course and the effect of acetylcholine on atrial and nodal cells of the rabbit heart," *J. Gen. Physiol.*, vol. 54, pp. 607-635, 1969.
- [25] A. L. Hodgkin, A. F. Huxley, "A quantitative description of membrane current and its application to conduction and excitation in nerve," *J. Physiol.*, vol. 117, pp. 500-544, 1952.
- [26] C. H. Luo, Y. A. Rudy, "A dynamic model of the cardiac ventricular action potential. I. Simulations of ionic currents and concentration changes," *Circ. Res.*, vol. 74, pp. 1071-1096, 1994.

- [27] C. H. Luo, Y. A. Rudy, "A dynamic model of the cardiac ventricular action potential. II. Afterdepolarizations, triggered activity, and potentiation," *Circ. Res.*, vol. 74, pp. 1097-1113, 1994.
- [28] J. P. Keener, "The effects of discrete gap junction coupling on propagation in myocardium," *J. Theor. Biol.*, vol. 148, pp. 49-82, 1991.
- [29] G. W. Beeler, H. Reuter, "Reconstruction of the action potential of myocardial fibres," *J. Physiol. (Lond.)*, vol. 268, pp.177-210, 1977.
- [30] L. Ebihara, E. A. Johnson, "Fast sodium current in cardiac muscle, a quantitative description," *Biophys. J.*, vol. 32, pp. 779-790, 1980.
- [31] S. Dhein, *Cardiac Gap Junctions: Physiology, Regulation, Pathophysiology and Pharmacology*, Karger, Basel, 1998.
- [32] S. Baigent, S. Jaroslav, A. Warner, "Modeling the effect of gap junction nonlinearities in systems of coupled cells," *J. Theor. Biol.*, vol. 186, pp. 223-239, 1997.
- [33] F. F. Bukauskas et al., "Gating properties of gap junction channels assembled from connexin43 and connexin43 fused with green fluorescent protein," *Biophys. J.*, vol. 81, pp. 137-152, 2001.
- [34] V. Valiunas et al., "Formation of heterotypic gap junction channels by connexins 40 and 43," *Circ. Res.*, vol. 86, pp. E42-E49, 2000.
- [35] H. Z. Wang, J. Li, L. F. Lemanski, and R. D. Veenstra, "Gating of mammalian cardiac gap junction channels by transjunctional voltage," *Biophys. J.*, vol. 63, pp. 139-151, 1992.
- [36] H. B. Nuss et al., "Cellular basis of ventricular arrhythmias and abnormal automaticity in heart failure," *Am. J. Physiol.*, vol. 277, pp. H80-H91, 1999.

- [37] L. T. Izu et al., "Evolution of Cardiac Calcium Waves from Stochastic Calcium Sparks," *Biophysical J.*, vol. 80, pp. 103-120, Jan. 2001.
- [38] C. E. Shannon, "A mathematical theory of communication," *The Bell System Technical Journal*, vol. 27, pp. 379-423, 623-656, Jul 1948.
- [39] S. Rohr, "Role of gap junctions in the propagation of the cardiac action potential," *Cardiovasc. Res.*, vol. 62, pp. 309-322, 2004.
- [40] M. S. Spach, J. F. Heidlage, P. C. Dolber, and R. C. Barr, "Extracellular discontinuities in cardiac muscle: evidence for capillary effects on the action potential foot," *Circ. Res.*, vol. 83, pp. 1144-1164, 1998.
- [41] J. J. Fox, J. L. McHarg, and R. F. Gilmour, "Ionic mechanism of cardiac alternans," *Am. J. Physiol.*, vol. 282, pp. H516-H530, 2002.
- [42] D. E. Gutstein et al., "Conduction slowing and sudden arrhythmic death in mice with cardiac-restricted inactivation of connexin43," *Circ. Res.*, vol. 88, pp. 333-339, 2001.
- [43] D. L. Lerner, K. A. Yamada, R. B. Schuessler, J. E. Saffitz, "Accelerated onset and increased incidence of ventricular arrhythmias induced by ischemia in Cx43-deficient mice," *Circ.*, vol. 101, pp. 547-552, 2000.
- [44] A. M. Gerdes, et al., "Structural remodeling of cardiac myocytes from patients with chronic ischemic heart disease," *Circ.*, vol. 86, pp. 426-430, 1992.
- [45] K. Amann et al., "Myocyte/capillary mismatch in the heart of uremic patients," *J. Am. Soc. Nephrol.*, vol. 9, pp. 1018-1022, 1998.
- [46] W. C. De Mello, "Cell swelling, impulse conduction, and cardiac arrhythmias in the failing heart. Opposite effects of angiotensin II and angiotensin (1-7) on cell volume regulation," *Mol. Cell. Biochem.*, vol. 330, pp. 211-217, 2009.

- [47] D. M. Bers, "Calcium and cardiac rhythms: Physiological and pathophysiological," *Circ.Res.*, vol. 90, pp. 14-17, 2002.
- [48] J. T. Nguyen, X. Li, and F. Lu, "The Electrocardiogram and Clinical Cardiac Electrophysiology," in *Cardiac Electrophysiology Methods and Models*, D.C. Sigg, et al., Ed. Springer, 2010, pp. 91-116.
- [49] J. K. Donahue, M. Strom, and I. D. Greener, "Introduction to Translational Research," in *Cardiac Electrophysiology Methods and Models*, D.C. Sigg, et al., Ed. Springer, 2010, pp. 441-455.
- [50] S. M. Moghimi et al., "Nanomedicine: current status and future prospects," *The FASEB Journal*, vol. 19, pp. 311-330, 2005.
- [51] B. Godin et al., "Emerging applications of nanomedicine for the diagnosis and treatment of cardiovascular diseases," *Trends Pharmacol. Sci.*, vol. 31, 199-205, 2010.
- [52] B. Atakan, O. B. Akan, "Deterministic Capacity of Information Flow in Molecular Nanonetworks," *Nano Communication Networks Journal (Elsevier)*, vol. 1, no. 1, pp. 31-42, March 2010.
- [53] A. Einolghozati, M. Sardari, F. Fekri, "Capacity of diffusion based Molecular Communication with ligand receptors," in *2011 IEEE Information Theory Workshop*.
- [54] J. G. Proakis, *Digital Communications*, 5th ed. New York: McGrawHill, 2001.
- [55] F. Magee, J. Proakis, "Adaptive maximum-likelihood sequence estimation for digital signaling in the presence of intersymbol interference (Corresp.)," *IEEE Trans. Inf. Theory*, vol.19, pp. 120-124, 1973.
- [56] D. Kilinc, O. B. Akan, "Receiver Design for Molecular Communication," to appear in *IEEE Journal on Selected Areas in Communications (JSAC)*, 2013.

-
- [57] A. Kavcic, J. M. F. Moura, "The Viterbi algorithm and Markov noise memory," *IEEE Trans. Inf. Theory*, vol.46, pp.291-301, 2000.
- [58] A. Kavcic, J. M. F. Moura, "Correlation-sensitive adaptive sequence detection," *IEEE Trans. Magn.*, vol. 34, no.3, pp.763-771, 1998.
- [59] B. Sklar, "How I learned to love the trellis," *IEEE Signal Processing Magazine*, vol.20, no.3, pp. 87-102, May 2003.
- [60] G. L. Stuber, *Principles of Mobile Communication*, 3rd ed. Kluwer Academic Publishers, Boston, 1996.
- [61] I. F. Akyildiz, J. M. Jornet, and M. Pierobon, "Propagation Models for Nanocommunication Networks," in *Proc. of EUCAP 2010, Fourth European Conference on Antennas and Propagation*, April 2010, pp. 4229-4232.
- [62] R. M. Goody and Y. L. Yung, *Atmospheric Radiation: Theoretical basis*, 2nd ed. Oxford University Press, 1989.
- [63] K. Finkenzeller, *RFID Handbook: Radio-Frequency Identification Fundamentals and Applications*, 2nd ed: Wiley, 2004.
- [64] Z. Sun and I. Akyildiz, "Underground wireless communication using magnetic induction," in *Proc. 2009 IEEE International Conference on Communications*, pp. 1-5.
- [65] Z. Sun and I. Akyildiz, "Magnetic induction communications for wireless underground sensor networks," *IEEE Transactions on Antenna and Propagation*, vol. 58, no. 7, pp. 2426-2435, July 2010.
- [66] B. Gulbahar, O. B. Akan, "A Communication Theoretical Modeling and Analysis of Underwater Magneto-Inductive Wireless Channels," *IEEE Trans. Wireless Commun.*, vol. 11, no. 9, pp. 3326-2234, 2012.

- [67] M. Sun, S. A. Hackworth, Z. Tang, G. Gilbert, S. Cardin, and R. J. Scلابassi, "How to pass information and deliver energy to a network of implantable devices within the human body," in *Proc. IEEE Conf. on Engineering in Medicine and Biology Society*, Aug. 2007, pp. 5286-5289.
- [68] D. Kilinc, O. B. Akan, "Nanoscale Magneto-Inductive Communication," to appear in *Proc. Asilomar Conference on Signals, Systems, and Computers*, California, USA, November 2013.
- [69] D. J. Bell, L. X. Dong, Y. Sun, L. Zhang, B. J. Nelson, D. Grutzmacher, "Manipulation of nanocoils for nanoelectromagnets," in *Proc. of the 5th IEEE Conf. on Nanotechnology*, Nagoya, 2005, pp.303-306.
- [70] H. Tohmyoh, H. Takeda, and M. Saka, "Fabrication of a Free-Standing Pt Micro-Ring on an Electrode Chip as a Small Magnetic Source," *J. Micromech. Microeng.*, vol. 19, pp. 085013 (5 pages), 2009.
- [71] X. Q. Chen, S. L. Zhang, D. A. Dikin, W. Q. Ding, R. S. Ruoff, L. J. Pan, and Y. Nakayama, "Mechanics of a Carbon Nanocoil," *Nano Lett.*, vol. 3, pp. 1299-1304, 2003.
- [72] P. L. McEuen and J. Y. Park, "Electron transport in single-walled carbon nanotubes," *Mater. Res. Soc. Bull.*, vol. 29, no. 4, pp. 272-275, Apr. 2004.
- [73] F. Kreupl, A. P. Graham, M. Liebau, G. S. Duesberg, R. Seidel, and E. Unger, "Carbon nanotubes for interconnect applications," in *Proc. IEEE Int. Electron Devices Meeting*, 2004, pp. 683-686.
- [74] A. Nieuwoudt, Y. Massoud, "Understanding the Impact of Inductance in Carbon Nanotube Bundles for VLSI Interconnect Using Scalable Modeling Techniques," *IEEE Transactions on Nanotechnology*, vol. 5, no. 6, pp. 758-765, Nov. 2006.

-
- [75] A. Nieuwoudt, Y. Massoud, "Predicting the performance of low-loss on-chip inductors realized using carbon nanotube bundles," *IEEE Transactions on Electron Devices*, vol. 55, pp. 298-312, 2008.
- [76] S. S. Mohan, M. del Mar Hershenson, S. P. Boyd, T. H. Lee, "Simple accurate expressions for planar spiral inductors," *IEEE J. Solid-State Circuits*, vol. 34, pp. 1419-1424, Oct. 1999.
- [77] C. Stampfer, A. Jungen, R. Linderman, D. Obergfell, S. Roth, and C. Hierold, "Nanoelectromechanical displacement sensing based on single-walled carbon nanotubes," *Nano Letters*, vol. 6, no. 7, pp. 1449-53, 2006.
- [78] J. Agbinya and M. Masihpour, "Power equations and capacity performance of magnetic induction body area network nodes," in *Proc. 2010 IEEE Broadband and Biomedical Communications*, pp. 1-6.
- [79] J. Agbinya, and M. Masihpour, "Power equations and capacity performance of magnetic induction communication systems," *Wireless Personal Communications*, vol. 64, pp. 831-845, 2012.
- [80] J. B. Johnson, "Thermal Agitation of Electricity in Conductors," *Phys. Rev.*, vol. 32, pp. 97-109, 1928.
- [81] P. L. McEuen and J. Y. Park, "Electron transport in single-walled carbon nanotubes," *Mater. Res. Soc. Bull.*, vol. 29, no. 4, pp. 272-275, Apr. 2004.
- [82] E. Warburg, "Magnetische untersuchungen," *Ann. Phys. (Leipzig)*, vol. 13, pp. 141-164, 1881.
- [83] D. J. Bell, L. X. Dong, Y. Sun, L. Zhang, B. J. Nelson, D. Grutzmacher, "Manipulation of nanocoils for nanoelectromagnets," in *Proc. of the 5th IEEE Conf. on Nanotechnology*, Nagoya, 2005, pp.303-306.

- [84] H. Tohmyoh, H. Takeda, and M. Saka, "Fabrication of a Free-Standing Pt Micro-Ring on an Electrode Chip as a Small Magnetic Source," *J. Micromech. Microeng.*, vol. 19, pp. 085013 (5 pages), 2009.
- [85] X. Q. Chen, S. L. Zhang, D. A. Dikin, W. Q. Ding, R. S. Ruoff, L. J. Pan, and Y. Nakayama, "Mechanics of a Carbon Nanocoil," *Nano Lett.*, vol. 3, pp. 1299-1304, 2003.
- [86] A. Nieuwoudt, Y. Massoud, "Understanding the impact of inductance in carbon nanotube bundles for VLSI interconnect using scalable modeling techniques," *IEEE Trans. Nanotechnol.*, vol. 5, no. 6, pp. 758-765, 2006.
- [87] H. Li and K. Banerjee, "High-frequency analysis of carbon nanotube interconnects and implications for on-chip inductor design," *IEEE Trans. Electron Devices*, vol. 56, no. 10, pp. 2202-2214, Oct. 2009.
- [88] P. L. McEuen and J. Y. Park, "Electron transport in single-walled carbon nanotubes," *Mater. Res. Soc. Bull.*, vol. 29, no. 4, pp. 272-275, Apr. 2004.
- [89] F. Kreupl, A. P. Graham, M. Liebau, G. S. Duesberg, R. Seidel, and E. Unger, "Carbon nanotubes for interconnect applications," in *Proc. IEEE Int. Electron Devices Meeting*, 2004, pp. 683-686.
- [90] V. K. Pecharsky and Jr. K. A. Gschneidner, Giant magnetocaloric effect in $\text{Gd}_5(\text{Si}_2\text{Ge}_2)$, *Phys. Rev. Lett.*, vol. 78, pp. 4494-4497, June 1997.
- [91] R. Hergt, R. Hiergeist, I. Hilger, W. A. Kaiser, Y. Lapatnikov, S. Margel, and U. Richter, "Maghemite nanoparticles with very AC-losses for application in RF-magnetic hyperthermia," *J. Magn. Magn. Mater.*, vol. 270, pp. 345-357, 2004.
- [92] Z. L. Wang, "Towards self-powered nanosystems: From nanogenerators to nanopiezotronics," *Advanced Functional Materials*, vol. 18, no. 22, pp. 3553-3567, 2008.

- [93] S. Xu, B. J. Hansen, and Z. L. Wang, "Piezoelectric-nanowire-enabled power source for driving wireless microelectronics," *Nature Communications*, vol. 1, no. 7, pp. 1-5, Oct 2010.
- [94] P. Debye, "Einige Bemerkungen zur Magnetisierung bei tiefer temperatur," *Ann. Phys.* vol. 81, pp. 1154-60, 1926.
- [95] W. F. Giauque, "A thermodynamic treatment of certain magnetic effects. A proposed method of producing temperatures considerably below 1° absolute," *J. Am. Chem. Soc.*, vol. 49, pp. 1864-70, 1927.
- [96] W. F. Giauque and D. P. MacDougall, "Attainment of temperature below 1° absolute by demagnetization of $\text{Gd}_2(\text{SO}_4)_3 \cdot 8\text{H}_2\text{O}$," *Phys. Rev.*, vol. 43, pp. 768, 1933.
- [97] G. V. Brown, "Magnetic heat pumping near room temperature," *J. Appl. Phys.*, vol. 47, pp. 3673-80, 1976.
- [98] V. K. Pecharsky and Jr. K. A Gschneider, "Magnetocaloric effect and magnetic refrigeration," *J. Magn. Magn. Mater.*, vol. 200, pp. 44-56, 1999.
- [99] A. H. Morrish. *The Physical Principles of Magnetism*, New York: Wiley, 1965.
- [100] T. Heimburg. *Thermal Biophysics of Membranes*. Wiley-VCH, 2007.
- [101] C. K. Alexander and M. N. O. Sadiku, *Fundamentals of Electric Circuits*, 4th ed. New York: McGraw-Hill, 2008.
- [102] L. E. Reichl. *A modern course in statistical physics*, Wiley, 1980.
- [103] L. D. Landau and E. M. Lifshitz. *Statistical Physics (Course of Theoretical Physics Vol. 5)*, Pergamon Press, 1980.

-
- [104] L.W. Couch. *Digital and Analog Communication Systems*, New Jersey: Prentice Hall, 2002.
- [105] A. K. Gupta and M. Gupta, "Synthesis and surface engineering of iron oxide nanoparticles for biomedical applications," *Biomaterials*, vol. 26, pp. 3995-4021, 2005.
- [106] J. Blumm and A. Lindemann, "Characterization of the thermophysical properties of molten polymers and liquids using the ash technique," *High Temperatures - High Pressures*, vol. 35/36, pp. 627-632, 2003.

CURRICULUM VITAE

DENİZ KILINÇ was born in Malatya on December 11, 1988. He graduated from Ankara Science High School (AFL) in 2006. He received his B.S. degree in Electrical and Electronics Engineering from Middle East Technical University (METU), Ankara, Turkey, in 2011. He received his M.S. degree under the supervision of Prof. Ozgur B. Akan in Electrical and Electronics Engineering from Koc University, Istanbul, Turkey in 2013. At the same time, he was a research assistant in the Next-generation and Wireless Communications Laboratory (NWCL), Koc University. His current research interests include nanoscale communication, intra-body communication, and detection & estimation theory.